UNIVERSITÄT OSNABRÜCK

Department of Physics

From initial growth of ultrathin Fe_3O_4 films up to $NiFe_2O_4$ formation through interdiffusion of Fe_3O_4/NiO bilayers on Nb:$SrTiO_3$(001)

Olga Kuschel, M.Sc.

Dissertation (kumulativ)

zur Erlangung des Doktorgrades (Dr. rer. nat.)

des Fachbereichs Physik der Universität Osnabrück

Osnabrück, February 2020

Examiners:

Prof. Dr. Joachim Wollschläger

Prof. Dr. Jan Ingo Flege

Contents

It is the investment in basic science that we are making today that will fuel the technological innovations of tomorrow. [1]

1 Introduction

Nowadays, the permanently growing generation and amount of information force a continuous development of more and more efficient storage and memory technologies. This trend becomes particularly clear by comparing the price of about 200,000 $ per gigabyte of hard drive storage in 1982 and 0.06 $ in 2012 [2]. Considering this rapid progress, the question arises how the efficiency of electronic devices can be continuously increased, in line with price and size reduction overcoming physical limits of the nanostructures needed. Here, the expanding area of spintronics constituted substantial advances in data storage technologies in the last decades [3]. In contrast to conventional electronics, where only the charge of the electrons is defining, spintronics also involves the spin as an additional degree of freedom to perform logic operations or store information.

One of the most famous phenomenon and possibly the initial breakthrough of this research field is the discovery of the giant magnetoresistance effect (GMR) by P. Grünberg and A. Fert in 1988 [4, 5]. The GMR is based on spin-dependent transport leading to a highly sensitive dependence of the electrical resistivity on the relative angle between the magnetizations of two ferromagnetic films, which are separated by a non-magnetic conductive layer. Already in 1997, sensing elements based on the GMR effect were introduced as readback heads in commercial computer hard-disk drives allowing a reduction in size and a significant enhancement of the storage capacity.

Another spintronic effect is the so-called tunneling magnetoresistance (TMR), which was discovered by M. Julliére in 1975 in Fe/GeO/Co trilayers at 4.2 K [6]. However, only the observation of the TMR effect at room temperature by Miyazaki *et al.* [7] and Moodera *et al.* [8] in 1995 has entailed a great number of theoretical and experimental studies pioneering the development of non-volatile magnetoresistive random-access memory (MRAM) devices [9, 10]. TMR devices exhibit basically a similar structure as GMR devices, namely, two ferromagnetic conductive layers (electrodes) separated by a non-magnetic film (tunneling barrier) which, however, in this case consists of an insulating material.

In this context, the scientific understanding of fundamental phenomena in the rising field of spintronics has been the key to develop new functional materials. Here, magnetic oxides move into the focus of current investigations due to a broad variety of magnetic and electronic properties. Since the performance of spintronic devices based on TMR or GMR strongly depends on the effective generation of highly spin-polarized electron currents, materials exhibiting a finite density of states at the Fermi level for one spin direction and a gap for the other spin direction - so-called half metals - are eminently suitable.

One of the most promising candidates for the usage as electrode material is the transition metal oxide Fe_3O_4 due to its half-metallic character and a predicted 100% spin polarization at the Fermi level [11]. Another approach is to use magnetic insulators as the tunnel barrier due to the exchange splitting of the conduction band leading to an effective spin polarization of the tunneling probability and making this material class highly suited for the application as spin filter or spin valve. Here, the (inverse) spinel type oxide $NiFe_2O_4$ is a representative material

providing both ferrimagnetic and insulating properties (band gap ∼1.5 eV) combined with a large exchange splitting of the conduction band (∼0.7 eV) [12, 13].

Also, the combination of Fe_3O_4 as an electrode material and $NiFe_2O_4$ as a tunnel barrier (spin-valve) is due to similar structural properties a promising strategy to achieve a fully epitaxial oxide spin-filter magnetic tunnel junction with high TMR ratios. However, the complex crystalline structure of (inverse) spinel type materials is highly sensitive to structural and chemical disorder and defects, which can strongly affect the properties of the material. Further, the growth process of iron oxides as well as ferrites is susceptible to deposition conditions which have to be optimized for every growth method individually. Thus, an accurate control of the structural, electronic and magnetic properties depending on the growth conditions and post-deposition treatments is indispensable.

Most of the previous studies have focused on the preparation of thin magnetite or other ferrite films on MgO(001) substrates due to the small lattice mismatch. However, epitaxial film growth on MgO substrates is limited by Mg^{2+} diffusion into the ferrite film for substrate temperatures above 250°C [14]. Due to intermixing, the interface roughness and the density of antiphase boundaries are significantly increased leading to a reduced performance in spintronic devices [15, 16]. One way to minimize or prevent Mg interdiffusion between substrate and film is the insertion of an additional buffer layer, e.g., metallic iron or NiO [17, 18]. Here, the usage of NiO is of particular interest in order to control the relative magnetization alignment between the two electrodes in magnetic tunnel junctions, since exchange bias is induced by an additional antiferromagnetic layer [19, 20]. Moreover, it has recently been shown that NiO can act as a spin-current amplifier in spin Seebeck experiments, and can additionally be a spin-current generator when a thermal gradient is applied [21–24], making NiO a key material for thermoelectric and spin caloritronic devices. Another approach is to use a more stable substrate, such as $SrTiO_3$(001) that does not show any interdiffusion into thin ferrite films even for higher annealing temperatures [25].

Within this cumulative thesis, a comprehensive study of the initial growth process of pure Fe_3O_4 films and Fe_3O_4/NiO bilayers on Nb:$SrTiO_3$(001) substrates including the thermal interdiffusion behavior of these bilayers is presented. The sensitive interplay between magnetic, electronic and structural properties of these materials has been investigated in detail.

First of all, the initial growth behavior of high-quality ultrathin magnetite films on $SrTiO_3$(001) deposited by reactive molecular beam epitaxy depending on the deposition temperature has been studied. For this purpose, the growth process has been monitored *in situ* and *during* the deposition by grazing incidence x-ray diffraction (GIXRD) technique. The results are published in *Applied Physics Letters* **111**, 041902 (2017) [26] and can be found in the reprinted version in Chap. 5. As a second step, a comparative study of Fe_3O_4/NiO bilayers grown on both MgO(001) and Nb:$SrTiO_3$(001) substrates exploring morphological, structural and magnetic properties is presented. These structures have been investigated by means of x-ray photoelectron spectroscopy (XPS), low-energy electron diffraction (LEED), x-ray reflectivity (XRR) and diffraction (XRD), as well as vibrating sample magnetometry (VSM). The corresponding results are published in *Materials* **11**, 1122 (2018) [27] and are reprinted in Chap. 6. Subsequently, thermal stability of these bilayers and the thermally induced interdiffusion process have been studied successively accompanied by a comprehensive characterization of the fundamental electronic, structural and magnetic properties using similar techniques as before. Finally, an alternative pathway for the preparation of ultrathin nickel ferrite films is provided. These results are published in *Physical Review B* **94**, 094423 (2016) [25] and reprinted in Chap. 7.

2 Theoretical background

2.1 Periodic structures - single crystals and thin films

An ideal crystal is defined as an infinite periodical repetition of identical structural elements in all spatial directions. Particularly, it is composed of a three dimensional lattice and a reiterated unit, also known as atomic basis, repeated at each lattice point (see Fig. 2.1). The (smallest) periodically repeated spatial configuration which completely defines the symmetry of the crystal lattice is called (primitive) unit cell. Note, there are several possibilities to choose the size and shape of the unit cell since only the translation symmetry has to be considered. The atomic basis ranges from simple assemblies of one or two atoms, such as for an Ag single crystal or for a NaCl structure, respectively, up to complicated arrangements of several atoms in Fe_3O_4 or some 10,000 atoms in protein crystals.

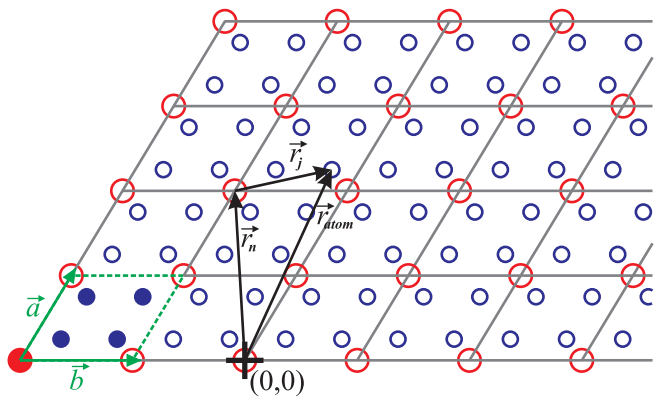

Fig. 2.1: Example of a two dimensional crystal with the unit cell (green) spanned by the vectors $\boldsymbol{a}$ and $\boldsymbol{b}$ as well as an atomic basis consisting of five atoms (filled red and blue circles). The red circles denote the origin of the unit cell and define the periodicity of the crystal lattice. The position $\boldsymbol{r_{atom}}$ of each atom within the crystal is given by the vectorial superposition of the lattice point position $\boldsymbol{r_n}$ and the atom position within the unit cell $\boldsymbol{r_j}$. Adapted from Ref. [28].

The whole crystal structure can be assembled by the repetitive translation of the unit cell along its principal axes. All possible lattice points of a three dimensional crystal are given by the lattice vector

$$\boldsymbol{r_p} = m\,\boldsymbol{a} + n\,\boldsymbol{b} + o\,\boldsymbol{c} \quad \text{with} \quad m, n, o \in \mathbb{Z} \quad , \tag{2.1}$$

where $\boldsymbol{a}$, $\boldsymbol{b}$ and $\boldsymbol{c}$ are the linear independent basis vectors. These vectors span the unit cell and reflect the shape of the crystal lattice. Alternatively, the lattice unit cell can be described by the absolute values of the lattice vectors, called lattice constants, and the angles α, β, γ between them. However, for a complete description not only the lattice but also the positions of atoms inside the unit cell (atomic basis) have to be considered. This can be done by an additional set of vectors

$$\boldsymbol{r_j} = u_j\,\boldsymbol{a} + v_j\,\boldsymbol{b} + w_j\,\boldsymbol{c} \quad \text{with} \quad 0 \leq u_j, v_j, w_j \leq 1 \quad , \tag{2.2}$$

which are pointing from the origin of the unit cell to the position of atom j. Thus, the position $\boldsymbol{r_{atom}}$ of each atom in a crystal is obtained by

$$\boldsymbol{r_{atom}} = \boldsymbol{r_j} + \boldsymbol{r_p} \quad . \tag{2.3}$$

This relation is schematically shown in Fig. 2.1 for a two dimensional crystal.

Classification of crystal lattices

In order to classify different crystal structures, a distinction is made based on the symmetry properties of the lattices. Possible symmetry operations are translation, rotation, reflection and inversion. Considering solely the symmetry of the point group (symmetries that keep at least one point fixed) a categorization in seven different crystal systems can be made (see Fig. 2.2). Namely, these are cubic, tetragonal, orthorhombic, hexagonal, trigonal, monoclinic and triclinic.

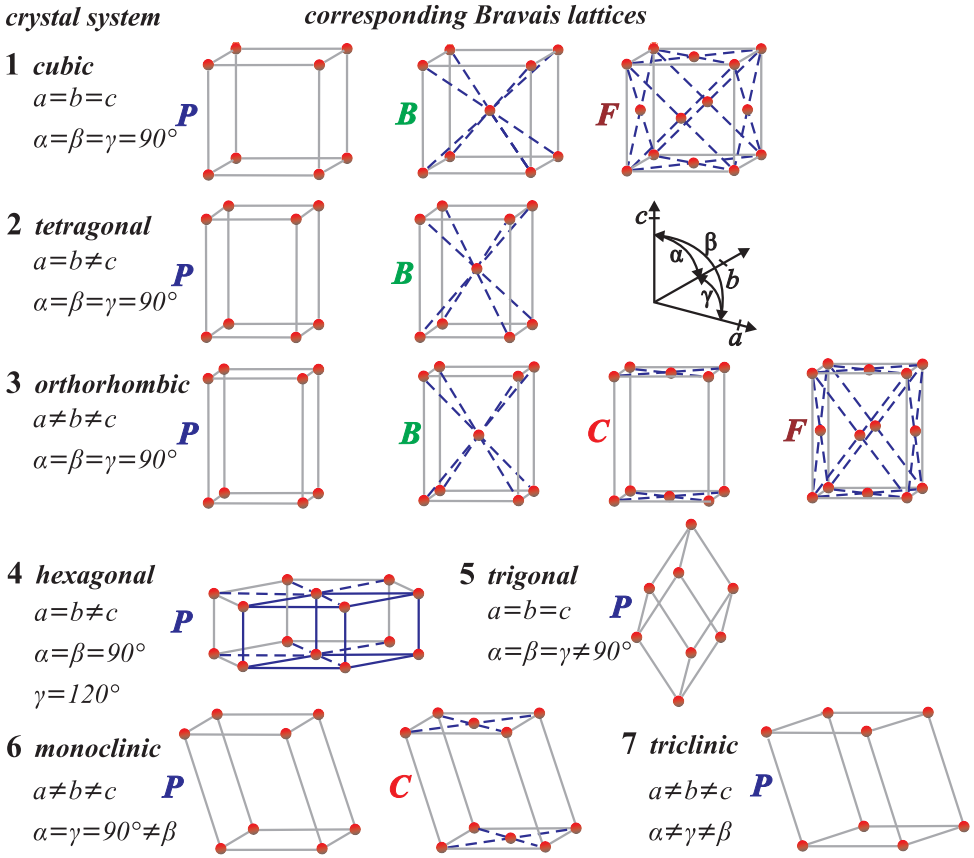

Fig. 2.2: The 14 three-dimensional Bravais lattices, which can be categorized in seven crystal systems. The letter P, B, F and C denotes primitive, body-centered, face-centered, base-centered unit cells, respectively. The unit cell of the hexagonal lattice is primitive and comprises only the blue framed regular prism. The corresponding Bravais lattice included in the trigonal crystal system is named rhombohedral. Adapted from Ref. [29].

Taking into account additional translational operations (e.g., screw rotation or glide reflection), 14 space groups can be defined, the so-called Bravais lattices (see Fig. 2.2). In addition to the seven primitive unit cells also seven centered unit cells are included. All crystalline materials (except quasicrystals) must, by definition, correspond to one of the Bravais lattices.

Considering a basis of any possible symmetry, the 14 Bravais lattices can be subdivided into 230 possible space groups and the seven crystal systems can be classified into 32 crystal classes. Note, in all cases the crystal translational periodicity should be valid, in addition. Therefore, e.g., five-fold symmetric lattices are not possible in regular crystals but can occur locally in so-called quasicrystals [29].

Crystalographic planes and directions - Miller notation

In order to describe different planes within a crystal, the so-called Miller indices are used. A certain crystallographic plane is determined by three integers h, k and l. These indices define a plane that intercepts the crystallographic axes at the points $\boldsymbol{a}/h$, $\boldsymbol{b}/k$ and $\boldsymbol{c}/l$. In case one of the indices is not an integer value, a triplet (hkl) with the smallest common multiple but the same ratios as the reciprocal intersection values is chosen. Negative values are written with an upper bar (e.g. $\overline{2}$ for -2) and if the plane does not intercept with a crystal axis the corresponding index is zero. Further, the triplet (hkl) indicates not solely one certain plane but a whole set of all parallel planes.

Directions within a crystal are denoted with square instead of round brackets $[hkl]$. For a cubic lattice, the crystallographic direction $[hkl]$ represents a vector which is normal to the (hkl) plane with the same indices. Note, this relation is not in general valid for other crystal types. In Fig. 2.3, some common crystallographic planes and corresponding directions are shown for a cubic lattice.

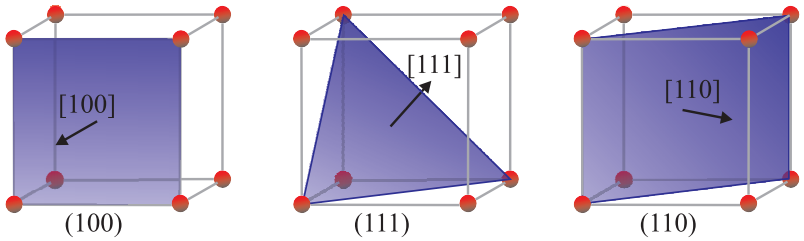

Fig. 2.3: Examples of the Miller notation for planes and directions in a simple cubic system. Crystallographic planes are denoted with round brackets and directions with square brackets. Here, directions normal to the depicted planes are shown.

2.1.1 Epitaxial growth and structural disorder

The growth of a thin film on top of a single crystalline substrate is called epitaxial if the film has a well-defined orientation with respect to the substrate crystal structure [30]. Both, thermodynamic as well as kinetic processes influence and control the film growth. Generally, three different growth modes are defined (see Fig. 2.4):

Layer-by-layer growth - Frank-van-der-Merve growth

The atoms are more strongly bound to the substrate surface then to each other. Consequently, a complete layer is formed prior to the growth of a subsequent layer on top.

Island growth - Volmer-Weber growth

Adatom-adatom interactions are stronger than interactions of the adatom with the surface leading to the formation of three dimensional islands directly on the surface.

Layer-plus-island growth - Stranski-Krastanov growth

Initially an atomically flat film is formed on the substrate surface following the layer-by-layer mode. After a critical layer thickness is reached, the nucleation and coalescence of islands takes place.

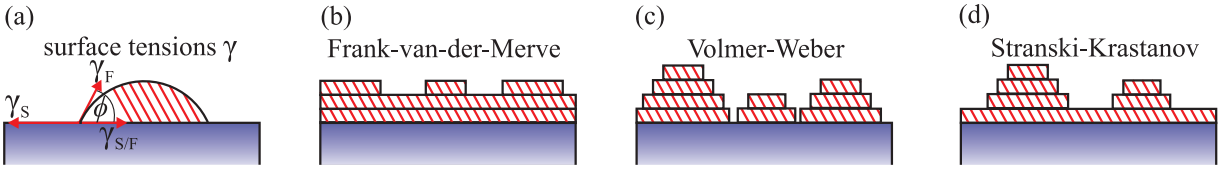

Fig. 2.4: (a) Illustration of the island wetting angle ϕ and the surface tensions γ. Three different growth modes are defined: (b) layer-by-layer or Frank-van-der-Merve growth, (c) 3D-island or Volmer-Weber growth and (d) layer-plus-island or Stranski-Krastanov growth.

Within the thermodynamic approach, the growth basically depends on the interplay between the surface and interface energies. These energies themselves are conditioned by the crystal structures, chemical potentials and lattice misfit between the film and substrate. In Fig. 2.4(a) the surface tensions of the substrate (γ_S), the film (γ_F) and substrate/film interface ($\gamma_{S/F}$) are illustrated. The force equilibrium can be written as

$$\gamma_S = \gamma_{S/F} + \gamma_F \cos\phi \tag{2.4}$$

where ϕ is the island wetting angle (contact angle). In case of a closed layer, the wetting angle ϕ equals zero leading to the condition $\gamma_S \geq \gamma_{S/F} + \gamma_F$ for the layer-by-layer growth mode. Further, the island growth can be described by the condition $\gamma_S < \gamma_{S/F} + \gamma_F$. If the surface tension of the film is increasing during growth of the first layers, the initial layer-by-layer growth converts into subsequent island growth.

In practice, the deposition conditions are often far away from thermodynamic equilibrium. In this case, kinetic controlled processes such as particle flux or diffusion at the surface, at step edges or within the film crucially influence the growth mode. Especially, strong variations of the growth modes can be observed depending on the deposition temperature.

2.1.2 Lattice mismatch and crystallographic defects

Generally, epitaxial growth can be divided in homoepitaxy and heteroepitaxy. In the former case, the deposited single-crystal material is the same as the substrate material. In the latter case, the deposited material and the substrate material are dissimilar, but still have a well-defined crystallographic orientation with respect to each other. Usually, heteroepitaxy is accompanied by a lattice mismatch between film and substrate and, thus, resulting strain effects and structural defects. Here, the magnitude of the lattice mismatch strongly affects the growth, but also a wide range of physical properties including defect states, band structure, magnetic anisotropy etc. The lattice mismatch is defined as

$$f = \frac{a_f - a_s}{a_s} \quad , \tag{2.5}$$

where a_f and a_s are the relaxed lateral lattice constants of the epitaxial layer and substrate, respectively.

Two basic mechanisms for compensation of the lattice mismatch are pseudomorphic growth and

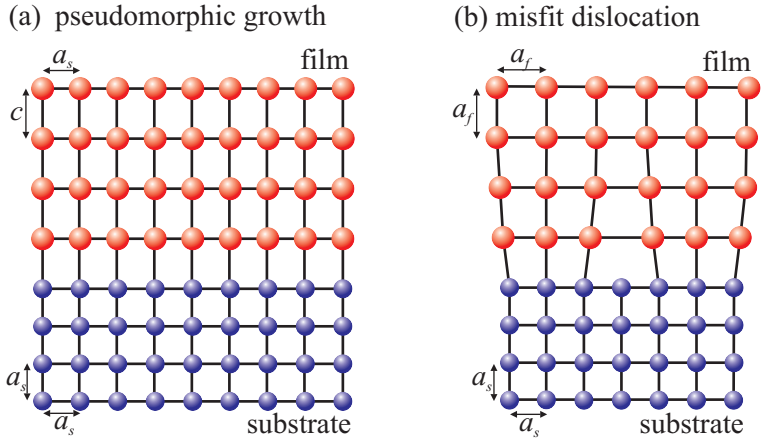

Fig. 2.5: Schematic drawings of the different relaxation mechanisms (a) pseudomorphic growth and (b) misfit dislocation. Here, a_s and a_f are the relaxed lattice parameters of the substrate and film, respectively. The pseudomorphic layer adopts the in-plane lattice constant of the substrate, which leads to a vertical distortion and a modified out-of-plane lattice constant c.

formation of misfit dislocations (see Fig. 2.5). During the pseudomorphic growth the epitaxial layer adopts the lateral lattice constants of the substrate. Consequently, the deposited film exhibits an in-plane strain equal to the lattice mismatch. In order to minimize the energy, the out-of-plane lattice parameter is compressively or tensilely distorted in relation to the mismatch of the system. Based on elastic theory for continuum, the vertical lattice constant c for homogeneous tetragonally distorted films is related to the lateral lattice constant a via [23]

$$\frac{\Delta c}{c} = \frac{2\nu}{\nu - 1}\frac{\Delta a}{a} \quad . \tag{2.6}$$

Here, ν is the Poisson ratio and Δa, Δc are the differences between the fully relaxed and strained lattice constants of the layer material.

With increasing film thickness, the strain energy stored in the pseudomorphic layer also increases. Hence, at a certain layer thickness it is energetically favorable to reduce the mismatch strain by formation of misfit dislocations [see Fig. 2.5(b)]. Following the model of Matthews and Blakeslee [31], the critical thickness d_c, at which the generation of dislocations will begin, is given by the formula

$$\frac{d_c}{b} = \frac{\left(1 - \nu\,\cos^2\alpha\right)\,\left(\ln\left(\frac{d_c}{b}\right) + 1\right)}{2\,\pi\,f\,(1+\nu)\,\cos(\lambda)} \quad . \tag{2.7}$$

Here, b is the magnitude of the Burgers vector, f is the lattice mismatch, ν is the Poisson ratio, α is the angle between the Burgers vector and the dislocation line ($\alpha = 90°$ for edge dislocations), and λ is the angle between the slip direction and that direction in the film plane which is perpendicular to the line of intersection of the slip plane and the interface ($\lambda = 45°$ for a rock salt structure).

Generally, the residual strain is a function of the initial mismatch and the layer thickness, which can be calculated based on the thermodynamic model assuming thermal equilibrium during growth. However, in some cases, kinetic barriers can prevent the lattice to relax completely. These are associated with the generation and movement of dislocations and depend strongly on the growth conditions and thermal post-deposition treatment. Note, even if the grown layer is

nearly fully relaxed at elevated deposition temperature, a lattice strain may still be induced by different thermal expansion coefficients of layer and substrate, when cooling down to room temperature.

Crystallographic defects

Apart from strain relaxation, several additional crystallographic defects can occur during growth of thin films or bulk crystals. Regarding the dimensionality of structural defects, a coarse distinction can be made in point defects, line defects, planar defects and bulk defects.

Point defects are located only at or around a single lattice point, namely vacancy, substitutional, interstitial or antisite defects. In case of line defects, entire rows of atoms in a crystal are dislocated along a line. Typical examples are step or screw dislocations, however, mixed types of dislocation are also common. Planar defects can be described as the interface between homogeneous crystalline regions including grain boundaries, antiphase boundaries or stacking faults. Grain boundaries occur at the interface of single-crystalline regions with different crystallographic orientations. In contrast, antiphase domains exhibit the same orientation but are shifted by a fraction of a lattice translation against each other (cf. Sec. 3.6 for antiphase boundaries in magnetite). Changing the stacking order of a base-centered cubic structure from ABCABC... to ACABCA... will lead to a hexagonal closed-packed structure in the ACA region. Such two-dimensional structural defects characterized by disordering of crystallographic planes are named stacking faults.

Other types of structural defects are the so-called bulk defects and chemical disorder. Exemplarily, these include pores, cracks, inclusions and clusters of impurities. Furthermore, regions or interfaces with deviations from the ideal stoichiometry or intermixed areas at the substrate-film interface can occur.

The density of structural and chemical defects is strongly influenced by the growth conditions, e.g., substrate temperature, deposition rate and method, subsequent annealing processes, as well as the cool-down rate, to name but a few.

2.2 Magnetic properties and magnetic anisotropies of thin films

The dependence of magnetic properties on the spatial direction is called magnetic anisotropy. There are several types of magnetic anisotropies, which affect the magnetization behavior and, thus, the shape of the magnetization curves of magnetic materials. The contributions can be intrinsic arising from crystal symmetry via the spin-orbit interaction or due to the shape of the sample via the dipole-dipole interaction or induced, e.g., by preparation conditions. The impact of the combined magnetic anisotropy contributions on the orientation of the magnetization can be described by the Stoner-Wohlfarth model [32]. This model is based on the assumption of a coherent magnetization rotation towards the direction of an external magnetic field requiring a monodomain state and constant magnitude of the magnetization vector. Thus, according to the Stoner-Wohlfarth model, the magnetization $\boldsymbol{M}$ is aligned in the direction of a local minimum of the energy density E, which is defined as

$$E = -\boldsymbol{H} \cdot \boldsymbol{M} + \sum_i E_i \quad . \tag{2.8}$$

Here, $-\boldsymbol{H} \cdot \boldsymbol{M}$ is the Zeeman energy and E_i are the individual anisotropy contributions.

Consequently, for isotropic media the energy density is determined solely by the Zeeman term. In this case, the minimum of E and, thus, the magnetization $\boldsymbol{M}$ is always aligned along the external

magnetic field $\boldsymbol{H}$. However, various anisotropy contributions can influence the energy landscape leading to a direction of $\boldsymbol{M}$ different from $\boldsymbol{H}$. In this context, an energy landscape may be formed with energetically favored directions (magnetic easy directions) and energetically disadvantageous directions (magnetic hard directions). In Fig. 2.6, typical magnetization curves are presented with external magnetic field aligned along a magnetic easy and magnetic hard axis. A clear hysteretic behavior of the magnetization reversal process is visible showing different magnetic behavior for increasing and decreasing external magnetic field. Significant parameters such as the saturation magnetization M_S, the magnetic remanence M_R and the coercive field H_C are marked in the exemplary magnetization curves for magnetic easy and hard directions. The magnetic easy axis

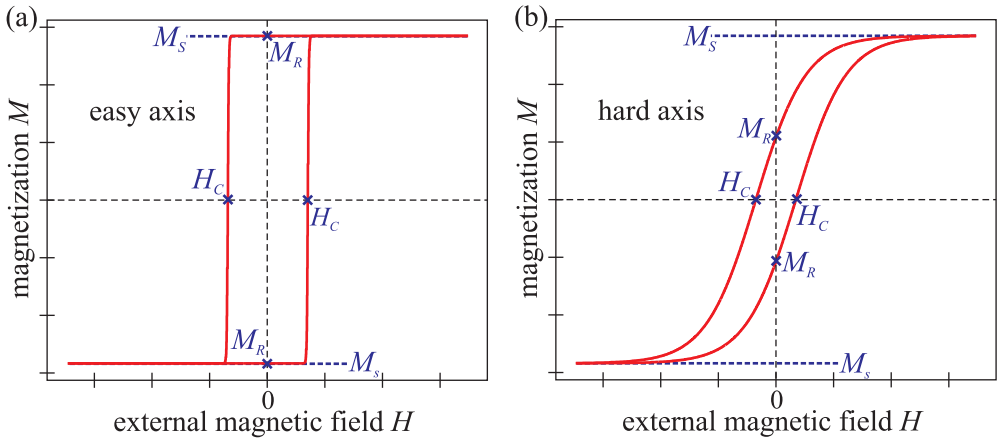

Fig. 2.6: Typical magnetization curve for (a) magnetic easy and (b) magnetic hard axis. Both curves show hysteretic behavior. The significant parameters, i.e, saturation magnetization M_S, magnetic remanence M_R and coercive field H_C are marked.

[Fig. 2.6(a)] is characterized by a large coercive field and large magnetic remanence leading to a square-like magnetization curve. Here, $M_R \approx M_S$. For a magnetic hard axis [Fig. 2.6(b)], the coercive field and the magnetic remanence are smaller than for the magnetic easy axis resulting in a rounded shape of the magnetization curve. Note, the magnetic remanence differs significantly from the saturation magnetization. The latter is commonly equal for all directions.

2.2.1 Shape anisotropy

Commonly, it is easier to magnetize a nonspherical specimen along its spatially more extended direction than along its spatially shorter direction. For example, an iron bar will favor a magnetization along its largest expansion and thin films will exhibit a preferred in-plane magnetization. This phenomenon is known as shape anisotropy and can be explained by the concept of the demagnetization field $\boldsymbol{H_N}$.

In a magnetized body the magnetic poles create a magnetic field $\boldsymbol{H_N}$ inside the body, which acts in the opposite direction with respect to the magnetization $\boldsymbol{M}$ and, therefore, partially demagnetize the sample. Outside the magnetized body this magnetic field is called stray field $\boldsymbol{H_S}$ and is antiparallel to $\boldsymbol{H_N}$. The magnitude of $\boldsymbol{H_N}$ depends on the shape of the magnetized body and on the alignment of the magnetization (see Fig. 2.7).

Further, the demagnetizing field is directly proportional to the magnetization and can be written as

$$\boldsymbol{H_N} = -\hat{N}\,\boldsymbol{M} \quad , \tag{2.9}$$

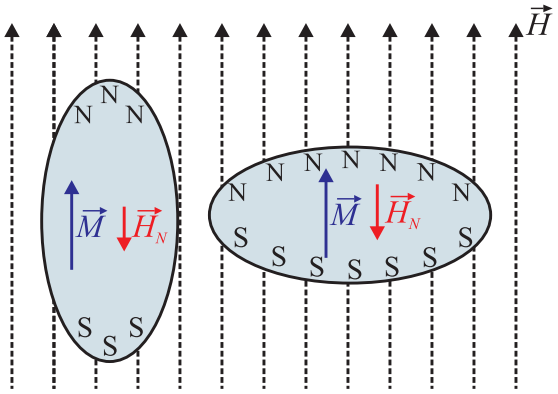

Fig. 2.7: Two identical bodies are magnetized along different spatial directions in an external magnetic field $\boldsymbol{H}$. Magnetic dipoles with poles N and S at the surface are induced leading to a magnetic field $\boldsymbol{H_N}$ inside the body, which is oriented antiparallel to the magnetization $\boldsymbol{M}$. The so-called demagnetization field $\boldsymbol{H_N}$ always occurs if the magnetization has a component normal to the surface. Thus, $\boldsymbol{H_N}$ has its minimum value if the largest expansion of the magnetized body is parallel to $\boldsymbol{H}$.

with $\hat{N}$ as the demagnetization tensor, which is defined by the shape of the sample. Then the contribution to the energy density E [Eq. (2.8)] is

$$E_N = -\frac{1}{2}\mu_0 \int_V \boldsymbol{H_N} \cdot \boldsymbol{M} dV = \frac{1}{2}\mu_0 \int_V (\hat{N} \cdot \boldsymbol{M}) \cdot \boldsymbol{M} dV \quad . \tag{2.10}$$

The contribution E_N is called magnetostatic self-energy or shape anisotropy energy. This is the energy one has to overcome to rotate the magnetization from a preferred to a disadvantageous direction.

For a spherical body the isotropic demagnetization factor $N = 1/3$ leads to $E_N = 0$ due to a completely uniform magnetization behavior (for details, see Ref. [33]). In the case of a thin film, $N \backsimeq 1$ for the magnetization aligned normal to the surface and $N \backsimeq 0$ for the magnetization parallel to the film surface. Therefore, the shape anisotropy for a thin film can be expressed using the saturation magnetization M_S and the angle $\theta_\perp$ between $\boldsymbol{M}$ and the normal of the film surface by

$$E_N^{film} \backsimeq \frac{1}{2}\mu_0 M_S^2 \cos^2 \theta_\perp \quad . \tag{2.11}$$

Thus, the shape anisotropy energy E_N^{film} is minimized for $\theta_\perp = 90°$ leading to preferred in-plane alignment of the magnetization in thin films. Consequently, if the magnetization is completely directed in-plane during the reversal process there will be no contribution of the shape anisotropy to the energy density E [Eq. (2.8)].

Note, these considerations are only valid for monodomain samples. In case of a multidomain state, each domain generates its own demagnetizing field and is affected by the stray fields of neighboring domains.

2.2.2 Magnetocrystalline anisotropy

The magnetocrystalline anisotropy originates mainly from the spin-orbit interaction influenced by the coupling between the crystal lattice and the orbital alignment. When the direction of the electron spin is reoriented by an applied magnetic field, the orbital momentum also tends to be reoriented due to the spin-orbit coupling. However, the orientations of the orbitals are strongly fixed to the crystal lattice. Thus, the energy required to rotate a spin system off the magnetic easy direction is mainly the energy, which is needed to overcome the spin-orbit coupling. Consequently, the magnetocrystalline anisotropy has the same symmetry as the crystal structure.

The anisotropy energy can be expressed as a series expansion of the direction cosines α_1, α_2, α_3 of the saturation magnetization relative to the crystal axes [34]. Considering the symmetry properties of the crystal lattice, the energy E_{cub} for a cubic structure, such as Fe_3O_4, can be written as

$$E_{cub} = K_1 \left(\alpha_1^2\alpha_2^2 + \alpha_2^2\alpha_3^2 + \alpha_1^2\alpha_3^2\right) + K_2 \left(\alpha_1^2\alpha_2^2\alpha_3^2\right) + \ldots \quad . \tag{2.12}$$

Here, K_1 and K_2 are the anisotropy constants, which in general are material- and temperature-dependent.

Usually, contributions containing higher powers are not needed for description of the cubic magnetocrystalline anisotropy. Moreover, in some cases the anisotropy constant K_2 is so small, that the second term in Eq. (2.12) can be neglected. Then the directions of the magnetic easy or hard axes depend only on the sign of K_1. For the case $K_1 > 0$, the magnetic easy axes are aligned along the x-, y- and z-direction ($\langle 100 \rangle$-directions) and the magnetic hard axes are directed along the space diagonals ($\langle 111 \rangle$-directions). For $K_1 < 0$ it is exactly the contrary.

2.2.3 Interface anisotropy

The interface anisotropy is caused by the changed spin-orbit interaction at the interface due to the symmetry break. For ultrathin films, the interface anisotropy can be stronger than the shape anisotropy leading to a preferred out-of-plane alignment of the magnetization. However, for all films in this thesis, the shape anisotropy is the dominating contribution leading to a favored in-plane alignment of the magnetization.

The combination of interface anisotropy K^{int} and volume contribution K^{vol} can be phenomenologically described as an effective magnetic anisotropy K^{eff} which is given by [35]

$$K^{eff} = K^{vol} + \frac{2}{D} K^{int} \quad , \tag{2.13}$$

with D as the film thickness. The factor 2 arises form the two interfaces of a thin layer. The volume anisotropy K^{vol} can consist of contributions from shape anisotropy, magnetocrystalline anisotropy and magnetoelastic energy etc. Note, this description is based on the simplifying assumption that K^{vol} and K^{int} are thickness independent.

2.2.4 Induced magnetic anisotropy contributions

There are several ways to induce a (uniaxial) magnetic anisotropy, e.g., by adjusting the growth parameters or by a subsequent treatment of the film etc. A commonly used procedure is to apply an external magnetic field either during growth or during subsequent annealing and cool-down of the sample [36, 37]. The latter is usually known as magnetic annealing. In metal alloys, for example, this creates a magnetic easy axis parallel to the applied magnetic field. Another way to induce uniaxial magnetic anisotropy in ferromagnetic materials is to apply uniaxial stress. In thin films, this can be done by choosing a substrate material with corresponding structural parameters or by applying tensile, compressive or bending strain. Additionally, the use of vicinal surfaces or oblique deposition techniques can lead to a growth-induced magnetic anisotropy [38, 39].

One further contribution to the magnetic anisotropy of a ferromagnetic material is the so-called exchange bias or exchange anisotropy. While all induced magnetic anisotropies mentioned so far are uniaxial, the exchange bias results in a unidirectional magnetic anisotropy. Its origin is

related to the magnetic coupling across the interface between a ferromagnetic and an antiferromagnetic layer, due to the exchange interaction. The uncompensated interfacial moments in the antiferromagnet tend to pin the adjacent moments in the ferromagnet. This leads to a shift of the hysteresis loop towards negative or positive magnetic field values.

2.2.5 Magnetic domains and domain walls

In order to minimize the free energy E [Eq. (2.8)], ferro(i)magnets tend to form domains separated by domain walls. This is not considered within the Stoner-Wohlfarth model which is usually restricted to describe monodomain states. However, the concepts of domain-wall pinning and nucleation of reverse domains are crucial for the correct explanation of magnetic coercivity in real materials.

Figure 2.8 illustrates the reduction of the spatial extent of the stray field $\boldsymbol{H_S}$ by domain formation with antiparallel magnetization. In this way, the magnetostatic self-energy given in Eq. (2.10) can be minimized. At the same time, the division into smaller and smaller domains increases the exchange energy due to antiparallel alignment of spins adjacent to the domain wall. Here, the exchange energy can be decreased if the rotation of the spins takes place gradually over several atoms forming domain walls. The energy required for the formation of a domain wall is called domain wall energy and is proportional to the area of the wall. Further, the spins within the domain wall or the magnetization of the individual domains could point off the magnetic easy direction leading to an increase of the energy that is given by the anisotropy contributions. Thus, the competition between different energy contributions determines the size of the domains, which are split by domain walls with nonzero width and a definite structure. Domain walls with out-of-plane rotation of the magnetization are called Bloch walls, while walls with in-plane rotation of the magnetization are the so-called Néel walls. A typical expansion of magnetic domains is about 10^{-8} m to 10^{-6} m and a domain wall thickness amounts to 10^{-9} m [40].

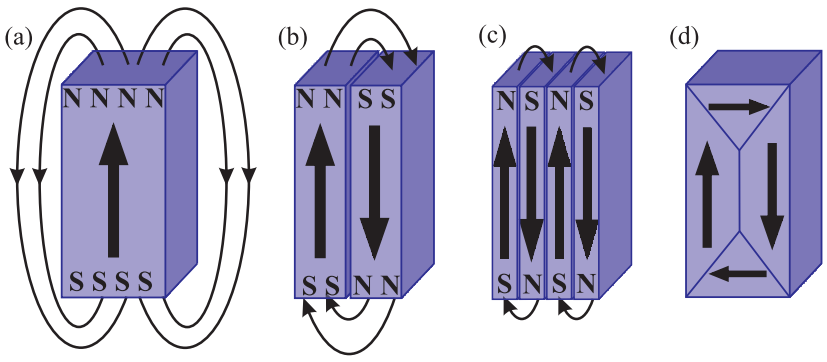

Fig. 2.8: Domain formation in a ferromagnetic material and the respective magnetic stray field $\boldsymbol{H_S}$. From (a) to (d): the magnetostatic energy decreases, while the energy of the domain wall and anisotropy energy increases. Adapted from Ref. [29].

Applying an external magnetic field results in a motion of domain walls and, thus, in a modification of the domain structure. By variation of the external magnetic field the domains can change their size, disappear or be generated. Consequently, the magnetization process of a ferro(i)magnet is mostly related to the change in the domain structure. This becomes visible in the hysteretic behavior of the ferromagnetic magnetization curve presented in Fig. 2.9. Especially, the initial magnetization process of a ferromagnet is mainly dominated by the motion of domain walls and is partially irreversible (blue curve in Fig. 2.9).

Ideally, all magnetic moments are aligned parallel to the direction of a certain magnetic field ending in a monodomain state and, thus, rotating coherently towards the applied magnetic field

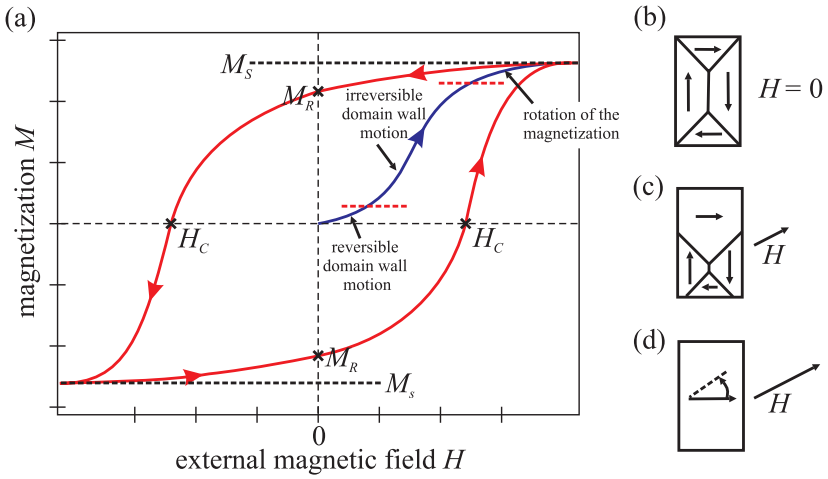

Fig. 2.9: (a) Magnetization curve of a ferromagnet. The initial magnetization curve is plotted in blue and the subsequent magnetization curve in red. (b)-(d) Schematical depiction of the changes in the domain structure depending on the external magnetic field $\boldsymbol{H}$. Adapted from Ref. [29].

direction. However, this is only valid for an ideal material. In real material, the magnetization process is strongly influenced by inhomogeneities such as structural defects, impurities or vacancies, and surface asperities. These defects can act as pinning centers for domain walls or nucleation centers for reverse domains. In the magnetization reversal process, the motion of domain walls takes only little energy, while the most critical step is the creation of a reverse domain. In this context, surface asperities or sharp corners are often the source of nucleation centers due to strong local demagnetizing fields occurring in vicinity of this defects. Once nucleated, the reverse domain tends to expand under the action of a reversed magnetic field. The propagation of domain walls itself can get pinned at defects, which act as a barrier or a trap. Strong pinning arises when these defects exhibit a spatial dimension comparable to the domain wall width. Here, the most effective pinning centers are planar defects, because they give rise to an energy change of the whole wall at the same time. R. W. DeBlois and C. P. Bean can demonstrate that small domains of reversed magnetization may always be present near imperfections, even if the material is nominally saturated [41]. Consequently, the magnetic properties including the magnetization reversal process are strongly influenced by inhomogeneities within the investigated material.

2.3 Vibrating sample magnetometry

Vibrating sample magnetometry (VSM) is an inductive measurement technique, which allows to determine the magnetic behavior of magnetic materials in an external magnetic field with high precision. The basic working principle rests upon Faraday's law, according to which an electromagnetic force is generated in a conductor by a time-varying magnetic flux. The induced voltage $U_{ind}(t)$ depends on the change in magnetic flux $\delta\Phi$ and is given by

$$U_{ind}(t) = -\frac{\delta\Phi}{\delta t} \quad . \tag{2.14}$$

In the measurement, a sample is magnetized by a uniform external magnetic field, which has no effect on the induced voltage. Additionally, the sample is vibrated vertically at a fixed frequency and amplitude in proximity to stationary detection coils (called pick-up coils). The induced voltage is proportional to the change in magnetic flux and can be calculated via

$$U_{ind}(t) \backsimeq -\sum_{n_w} \int_A \frac{\partial \boldsymbol{B}(\boldsymbol{t})}{\partial t} d\boldsymbol{A} \quad , \tag{2.15}$$

where n_w is the number of windings and $d\boldsymbol{A}$ is an area vector of the area enclosed by a single turn of a coil.

The change in magnetic flux depends on several factors including the amplitude $\hat{z}$ and frequency ω of the harmonic movement, the magnetic moment m of the sample and the position and orientation of the pick-up coils with respect to the measured sample. Thus, the resulting voltage induced in the VSM pick-up coils is proportional to

$$U_{ind}(t) \propto m\,\hat{z}\,\omega\,S\,\cos(\omega t) \quad . \tag{2.16}$$

Here, the parameter S contains the geometric information of the pick-up coils concerning position, orientation, number of windings and design of the coils.

A typical measurement setup of a VSM is shown in Fig. 2.10. A variable uniform magnetic field

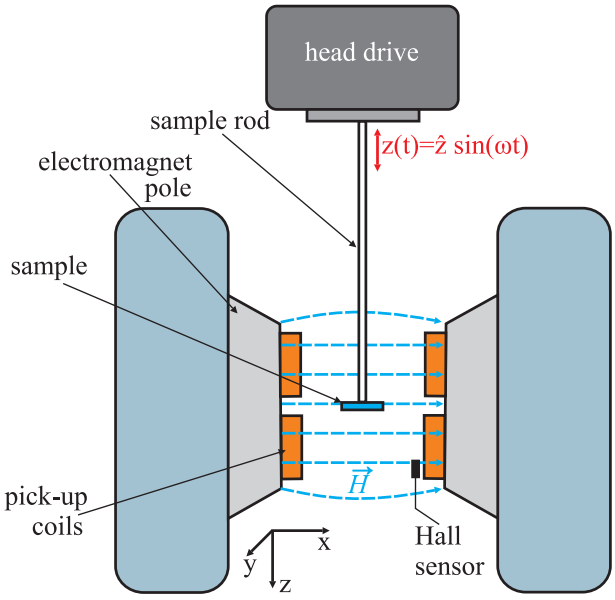

Fig. 2.10: Schematic representation of a VSM setup. The sample is placed on the sample rod, which is connected to the head drive containing the rotation and vibration unit. A variable magnetic field is produced by an electromagnet. The induced voltage is measured by the pick-up coils mounted on the poles of the electromagnet. The applied magnetic field is monitored by a Hall sensor adjacent to one of the poles.

is produced by an electromagnet. Depending on the electromagnet, magnetic fields in the range of a few Tesla are possible. The pick-up coils used for detection are mounted on the poles of the electromagnet. The magnetic field strength is monitored by a Hall probe positioned between the poles. The sample is fixed on a sample rod, which is mounted to the VSM head drive, and placed in between the poles of the electromagnet. A sinusoidal signal is transmitted by the VSM head drive into a vertical vibration around the symmetry center of the pick-up coils. Typically, the vibration frequency is in the range of $10 - 100\,\mathrm{Hz}$ and the amplitude amounts to a few tenths of a millimeter. To get a large signal-to-noise ratio, the measured voltage is passing a preamplifier and is ending in a lock-in-amplifier, which is tuned to the vibration frequency of the sample.

On the one hand, magnetic hysteresis curves can be recorded by measuring the magnetic moment of a material as a function of the applied magnetic field. On the other hand, the head drive allows to vary the sample orientation relative to the direction of the applied magnetic field (rotation around z-axis) and, thus, to measure the magnetic anisotropy. Further, temperature dependent measurements can be performed using a low temperature cryostat or a high temperature oven.

2.4 X-ray diffraction

The phenomenon of scattering can be interpreted as the redirection of light, which takes place when an electromagnetic wave encounters an obstacle or an inhomogeneity. Due to the interaction with the electromagnetic wave, the electrons of these scattering centers are periodically deflected. Consequently, the oscillating electron cloud acts as a Hertzian dipole and is the source of stray radiation. In the most cases, the scattering is elastic, which means that the emitted light exhibits the same frequency as the incident wave. The elastic scattering of electromagnetic waves at long range ordered periodic structures, e.g., crystals, is called diffraction. Here, interference of the scattered waves occurs, causing intense peaks at certain scattering angles, which are known as Bragg reflections. Bragg described the appearance of the interference pattern as a superimposition of waves reflected at different parallel lattice planes as illustrated in Fig. 2.11. If the phase

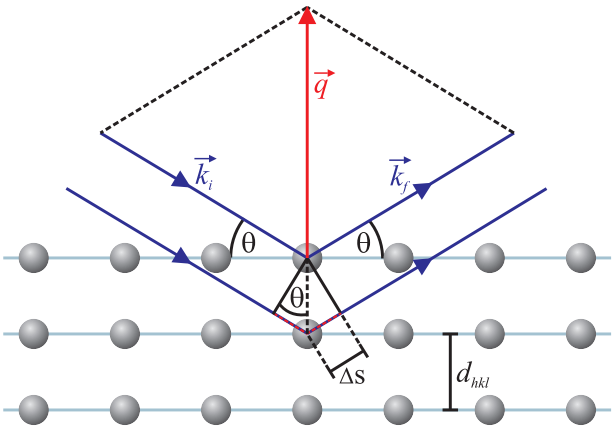

Fig. 2.11: Sketch of Bragg's law, which illustrates the condition for constructive interference depending on the scattering angle θ. An incoming wave $\boldsymbol{k_i}$ is diffracted at different lattice planes with the layer distance d_{hkl}. The outgoing waves $\boldsymbol{k_f}$ originating from these planes exhibit a path difference Δs. Constructive interference occurs, if the condition $2\Delta s = n\lambda$ is fulfilled. The scattering vector $\boldsymbol{q}$ is given by $\boldsymbol{k_f} - \boldsymbol{k_i}$ and oriented perpendicular to the lattice planes.

difference between the reflected waves is a multiple of their wavelength, constructive interference occurs. This condition can be described by Bragg's law [42]

$$2d_{hkl} \sin\theta = n\,\lambda \quad , \tag{2.17}$$

with d_{hkl} as the distance between the hkl-lattice planes, θ as the angle of incidence and reflection, and λ as the wavelength of the incident beam. The parameter n is a positive integer and indicates the order of the Bragg reflection.

Following Bragg's law, the general condition for diffraction is that the spacing between the scattering centers is of the order of the wavelength of the scattered wave. Since atomic distances in crystalline systems are of the order of a few Ångströms, x-rays in the energy range of $5 - 100\,\mathrm{keV}$ are needed to get information on the crystallographic and atomic structure of solids.

Laue equation and reciprocal lattice

An alternative description of the diffraction condition is given by the Laue equations [43]

$$\boldsymbol{q}\cdot\boldsymbol{a} = 2\pi\,h \quad , \quad \boldsymbol{q}\cdot\boldsymbol{b} = 2\pi\,k \quad , \quad \boldsymbol{q}\cdot\boldsymbol{c} = 2\pi\,l \quad , \tag{2.18}$$

with $\boldsymbol{q} = \boldsymbol{k_f} - \boldsymbol{k_i}$ as the scattering vector, which is given by the difference between the wave vectors of the incident and reflected wave $\boldsymbol{k_i}$ and $\boldsymbol{k_f}$, respectively. The basis vectors $\boldsymbol{a}$, $\boldsymbol{b}$ and $\boldsymbol{c}$ are defined in Sec. 2.1. Bragg peaks are observed if the scattering vector $\boldsymbol{q}$ fulfills all three Eqs. (2.18) for integer values of h, k and l at the same time. The integers h, k and l correspond to the Miller indices which are used to index lattice planes (see Sec. 2.1).

While in case of orthogonal crystal axes there is a simple solution of the Laue equations, the determination of $\boldsymbol{q}$ for all other cases is more complex. At this point, it is useful to introduce the reciprocal lattice, which is an universal and important concept for discussion and interpretation of diffraction phenomena at periodic structures. In analogy to the crystal lattice, which describes the position of atoms in a crystal, a reciprocal lattice gives the positions of Bragg points in the reciprocal space. The primitive translation vectors of the reciprocal lattice are given by

$$\boldsymbol{a}^* = 2\pi \frac{\boldsymbol{b} \times \boldsymbol{c}}{\boldsymbol{a} \cdot (\boldsymbol{b} \times \boldsymbol{c})} \quad , \quad \boldsymbol{b}^* = 2\pi \frac{\boldsymbol{c} \times \boldsymbol{a}}{\boldsymbol{a} \cdot (\boldsymbol{b} \times \boldsymbol{c})} \quad , \quad \boldsymbol{c}^* = 2\pi \frac{\boldsymbol{a} \times \boldsymbol{b}}{\boldsymbol{a} \cdot (\boldsymbol{b} \times \boldsymbol{c})} \quad . \tag{2.19}$$

Here, $\boldsymbol{a} \cdot (\boldsymbol{b} \times \boldsymbol{c})$ is the volume of the unit cell. In case of an orthogonal crystal system, the reciprocal lattice vectors point in the same directions as the lattice vectors in real space and their length is given by

$$a^* = \frac{2\pi}{a} \quad , \quad b^* = \frac{2\pi}{b} \quad , \quad c^* = \frac{2\pi}{c} \quad . \tag{2.20}$$

Thus, the reciprocal lattice is completely given by the set of points represented by all possible reciprocal lattice vectors

$$\boldsymbol{G} = h\boldsymbol{a^*} + k\boldsymbol{b^*} + l\boldsymbol{c^*} \quad \text{with} \quad h, k, l \in \mathbb{Z} \quad . \tag{2.21}$$

Using the definition of the reciprocal lattice, the Laue equation can be rearranged to

$$\boldsymbol{q} = \boldsymbol{k_f} - \boldsymbol{k_i} = \boldsymbol{G} \quad . \tag{2.22}$$

Therefore, constructive interference is observed if the scattering vector $\boldsymbol{q}$ equals a reciprocal lattice vector $\boldsymbol{G}$.

Bragg's law as well as the Laue conditions solely describe the occurrence of constructive interference but provide no quantitative information of the diffracted intensity. While the periodicity of the crystal lattice defines the positions of the Bragg peaks, the inner structure of the unit cell strongly influences the diffracted intensity. Consequently, the analysis of the intensity and shape of a Bragg peak provides information about atomic structure of the unit cell or the morphology of the surface. The amplitude of the diffracted wave can be written as

$$A(\boldsymbol{q}) = F(\boldsymbol{q})\, G(\boldsymbol{q}) \quad , \tag{2.23}$$

with $G(\boldsymbol{q})$ as the lattice factor and $F(\boldsymbol{q})$ as the structure factor containing information on the lattice symmetry and on the structure of the unit cell, respectively. One theoretical concept to describe diffraction phenomena in crystals including quantitative information is the so-called classic kinematic diffraction theory. Here, based on the weak interaction of x-rays with matter, some simplifications of the diffraction process can be made. In fact, multiple scattering effects and refraction as well as absorption processes of the incidence beam are not considered.

Further, for x-rays the cross section with the atomic nucleus is by orders of magnitude smaller than with electrons, thus scattered intensity from the nuclei is usually neglected. Therefore, the scattering of x-rays at a real crystal is given by the sum of the scattering processes at all contributing electrons. Taking into account these restrictions, a quantitative description of the diffracted intensity from a single crystalline film grown on a single crystalline substrate will be derivated in the following. This description is mainly based on theoretical works of Feidenhans'l, Robinson and Tweed [44, 45].

2.4.1 Scattering at a single electron

The amplitude $A(\boldsymbol{q})$ of an electromagnetic wave scattered at a single electron located at $\boldsymbol{r_e}$ can be described by the Thomson equation

$$A\,(\boldsymbol{q}) = A_0\,C\;e^{\,i\boldsymbol{q}\,\cdot\,\boldsymbol{r_e}} \quad \text{with} \quad C = \frac{e^2}{m_e\;c^2\;R_0} \quad . \tag{2.24}$$

Here, A_0 is the amplitude of the incident wave, R_0 the distance between the electron and the detector, c the speed of light and m_e and e are the mass and the charge of the electron, respectively. The resulting amplitude is given as a function of the scattering vector $\boldsymbol{q}$.

The influence of the polarization of the incident wave on the scattered intensity has not been considered here due to the strong dependence on the scattering geometry. It will be introduced in Sec. 4.2.4 as a correction factor.

2.4.2 Scattering at a single atom

The scattering at an atom is described as a sum over the scattering amplitudes for the individual electrons of the atom, using the Thomson equation [cf. Eq. (2.24)] and considering the phase difference between the waves scattered at different electrons. Note, the involved electrons are not localized at distinct positions but arranged around the center of the atom $\boldsymbol{r_a}$ according to the electron distribution function $\rho(\boldsymbol{r})$. One more point to consider is that the value R_0, included in the constant C, is assumed to be the same for all electrons, due to the much smaller spatial expansion of an atom. Hence, the amplitude $A(\boldsymbol{q})$ of the scattered wave is given by

$$A(\boldsymbol{q}) \;=\; A_0\,C \int d^3r\,\rho(\boldsymbol{r})\;e^{\,i\,\boldsymbol{q}\,\cdot\,(\boldsymbol{r_a}\,+\,\boldsymbol{r})} \tag{2.25}$$

$$\;=\; A_0\,C\,f(\boldsymbol{q})\;e^{\,i\,\boldsymbol{q}\,\cdot\,\boldsymbol{r_a}} \quad . \tag{2.26}$$

Here, the atom-dependent part of the amplitude is described as the atomic form factor

$$f(\boldsymbol{q}) = \int d^3r\,\rho(\boldsymbol{r})\;e^{\,i\,\boldsymbol{q}\,\cdot\,\boldsymbol{r}} \quad , \tag{2.27}$$

which is equivalent to the Fourier transform of the electron density of the atom. The form factors for different atoms can be determined by means of quantum mechanic calculations, e.g., Hartree-Fock or density functional theory. Assuming a spherical electron distribution, the form factor can be approximated by four Gaussian functions

$$f(q) = \sum_{i=1}^{4} a_i\;e^{\,-b_i\left(\frac{q}{4\pi}\right)^2} + c \quad . \tag{2.28}$$

In this case, the form factor $f(q)$ solely depends on the absolute value of the scattering vector $\boldsymbol{q}$. Tabulated values for the constants a_i, b_i and c for different atoms and ions can be found in literature [46].

2.4.3 Scattering at a single unit cell

The scattering process at a unit cell can be described as a sum over the scattering amplitudes resulting from scattering at the atoms inside the unit cell. Consequently, the scattering amplitude is given by

$$A(\boldsymbol{q}) = A_0\, C \sum_j f_j(q)\, e^{i\boldsymbol{q}\cdot\,(\boldsymbol{r_n}+\boldsymbol{r_j})} \tag{2.29}$$

$$= A_0\, C\, F(\boldsymbol{q})\; e^{i\boldsymbol{q}\cdot\boldsymbol{r_n}} \quad , \tag{2.30}$$

where $\boldsymbol{r_n}$ is the position of the unit cell and $\boldsymbol{r_j}$ the position of the j-th atom of the unit cell. Analogously, the sum of the atomic form factors $f_j(q)$ is defined as the structure factor of the unit cell

$$F(\boldsymbol{q}) = \sum_j f_j(q)\, e^{i\boldsymbol{q}\cdot\boldsymbol{r_j}} \quad . \tag{2.31}$$

Thus, the structure factor $F(\boldsymbol{q})$ is the Fourier transform of the electron distribution within the unit cell. In contrast to the atomic form factor, the structure factor $F(\boldsymbol{q})$ depends on the direction of the scattering vector $\boldsymbol{q}$ and not only on its absolute value. Here, the atomic distribution of the unit cell is not assumed to be spherically symmetric as it is the case for the electron distribution.

2.4.4 Thermal vibrations - Debye-Waller factor

In the previous sections, for the derivation of the atomic form factor and the structure factor, it was assumed that the atoms are located at definite positions. However, the atoms in a real crystal fluctuate around a mean value due to thermal effects. In addition to vibrations caused by thermal excitations, impurities, dislocations as well as defects in the crystal structure may affect the ideal positions of the involved atoms. Typical vibration frequencies for crystals are in the rage of $10^{12} - 10^{14}$ Hz. These vibrations affect the electron density function of the atoms and, thus, their scattering ability resulting in a change of the scattered intensity. This effect can be considered by a modified atomic form factor and, thus, the structure factor of the unit cell can be written as

$$\overline{F(\boldsymbol{q})} = \sum_j f_j(q)\, e^{i\boldsymbol{q}\cdot\boldsymbol{r_j}}\; e^{-\frac{1}{2}U_j(T)\,|\boldsymbol{q}|^2} \quad . \tag{2.32}$$

Here, a Gaussian distribution of the atoms around their ideal position is assumed. The factor $U_j(T)$ depends on the temperature T and is the so-called Debye-Waller factor of the j-th atom. The scattered intensity is decreasing with increasing scattering vector due to the damping of the structure factor.

In general, the vibration of an atom around the ideal position is an anisotropic function depending on the direction. Then, U_j is a second-order tensor representing the so-called vibrational ellipsoid. This may result in different thermal dependences for different hkl-directions. A more detailed description can be found in the literature [47, 48].

2.4.5 Diffraction at a single crystalline structure

A single crystal can be described as a periodical repetition of unit cells in all three spatial directions. Thus, the amplitude of a wave diffracted at a single crystal is given as the sum over the scattering amplitudes of the individual unit cells

$$A(\boldsymbol{q}) = A_0\, C \sum_n F_n(\boldsymbol{q})\; e^{i\boldsymbol{q}\cdot\boldsymbol{r_n}} \quad . \tag{2.33}$$

Assuming a crystal consisting of a finite number of equal unit cells and, thus, identical F_n for each unit cell, the diffracted amplitude can be rewritten as

$$A(\boldsymbol{q}) = A_0\, C\, F(\boldsymbol{q}) \sum_{n_a=0}^{N_a-1} \sum_{n_b=0}^{N_b-1} \sum_{n_c=0}^{N_c-1} e^{i\boldsymbol{q}\cdot\,(n_a\boldsymbol{a}+n_b\boldsymbol{b}+n_c\boldsymbol{c})} \tag{2.34}$$

$$= A_0\, C\, F(\boldsymbol{q}) \sum_{n_a=0}^{N_a-1} e^{in_a\,\boldsymbol{q}\cdot\boldsymbol{a}} \sum_{n_b=0}^{N_b-1} e^{in_b\,\boldsymbol{q}\cdot\boldsymbol{b}} \sum_{n_c=0}^{N_c-1} e^{in_c\,\boldsymbol{q}\cdot\boldsymbol{c}} \quad . \tag{2.35}$$

Here, the translation vector of each unit cell is replaced by $\boldsymbol{r_n} = n_a\boldsymbol{a} + n_b\boldsymbol{b} + n_c\boldsymbol{c}$, with $\boldsymbol{a}$, $\boldsymbol{b}$, $\boldsymbol{c}$ as the lattice vectors of the crystal. Further, N_a, N_b and N_c are the numbers of unit cells in the respective spatial direction.

Each of the sums can be identified as a geometric series, which can be rewritten for one particular direction as

$$S_{N_c}(\boldsymbol{q}) = \sum_{n_c=0}^{N_c-1} e^{in_c\,\boldsymbol{q}\cdot\boldsymbol{c}} = \frac{1-e^{iN_c\,\boldsymbol{q}\cdot\boldsymbol{c}}}{1-e^{i\,\boldsymbol{q}\cdot\boldsymbol{c}}} \quad . \tag{2.36}$$

By replacing $x = \boldsymbol{q}\cdot\boldsymbol{c}$ the diffracted intensity of a one dimensional crystal consisting of N_c

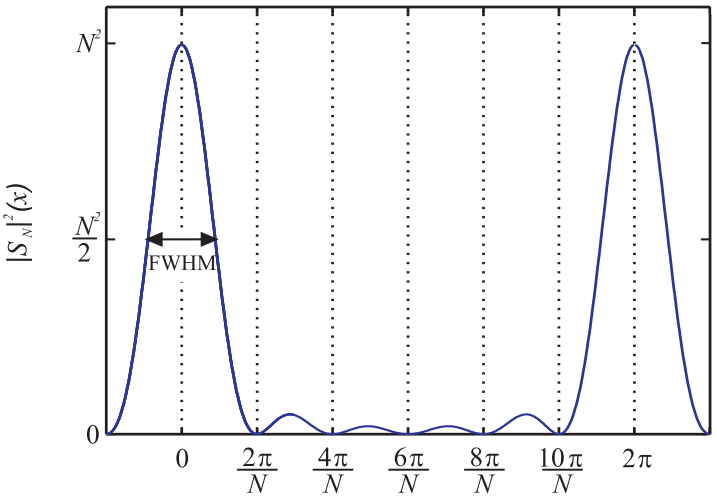

Fig. 2.12: N-slit function for $N = 6$ showing main maxima at multiples of 2π. $N-2$ fringes occur between two main maxima. The spacing between the fringes equals $2\pi/N$. The FWHM of the main maxima is given by $K_S(2\pi/N)$ with $K_S = 0.89$ [49].

scattering centers is given by the square of Eq. (2.36)

$$|S_{N_c}|^2(x) = \frac{\sin^2(N_c\, x/2)}{\sin^2(x/2)} \quad . \tag{2.37}$$

This expression is known as N-slit function and is depicted for $N = 6$ in Fig. 2.12. The function exhibits main maxima separated by a multiple of 2π and $N - 2$ smaller maxima or fringes in between of them. An increasing number of unit cells N in the particular crystallographic direction results in a decrease of the FWHM (full width at half maximum) of all maxima and an increase of the number of observed fringes within the interval of 2π.

Assuming an infinite number of unit cells $N_{a,b,c}$ in all three dimensions, like it is the case in an ideal single crystal, the N-slit function can be written as a series of δ-functions. The resulting diffraction amplitude is then given by

$$A(\boldsymbol{q}) \propto A_0\, C\, F(\boldsymbol{q}) \sum_h \sum_k \sum_l \delta(\boldsymbol{q}\cdot\boldsymbol{a} - 2\pi\, h)\, \delta(\boldsymbol{q}\cdot\boldsymbol{b} - 2\pi\, k)\, \delta(\boldsymbol{q}\cdot\boldsymbol{c} - 2\pi\, l) \quad . \tag{2.38}$$

This expression corresponds to the introduced Laue equations described by Eq. (2.18) and results in high intensity peaks at discrete points known as Bragg peaks [see Fig. 2.13(a)].

2.4.6 Diffraction at semi-infinite crystals and crystalline thin films

For real crystals, the concept of an infinite crystal is not sufficient to model the diffracted intensity. Thus, real crystals are theoretically described as semi-infinite with a limited number of unit cells in one direction. Moreover, real crystals exhibit a surface with a finite roughness, which the x-ray beam has to pass. Further, in contrast to the classic kinematic diffraction theory, absorption effects, leading to a weaker contribution from atoms in deeper layers, should be considered for the correct description of the diffracted intensity. All these effects result in a significant change of the intensity distribution in the diffraction pattern. More precisely, for a semi-infinite crystal the

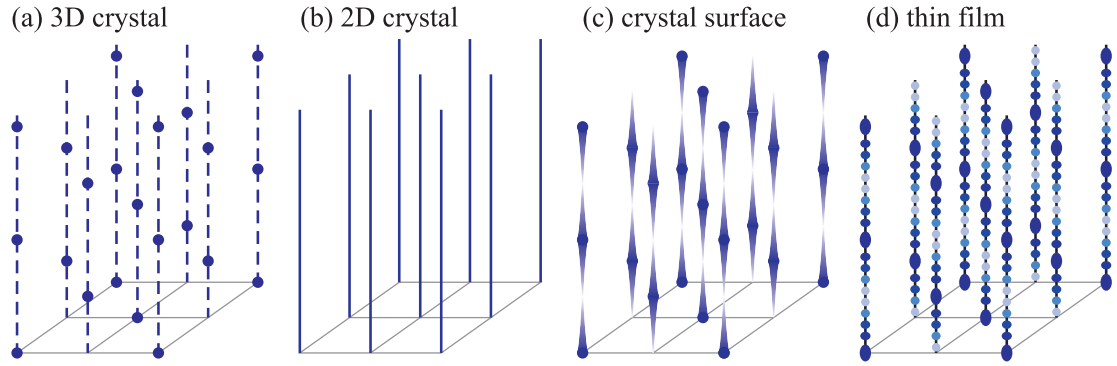

Fig. 2.13: Sketch of the distribution of the diffracted intensity in reciprocal space. (a) Infinite bulk crystals produce sharp Bragg peaks at single points. Here, the dashed lines are drawn to guide the eye. (b) Two dimensional layers produce diffraction rods due to reduced translational symmetry along the vertical direction. (c) Semi-infinite crystals with a surface produce diffraction peaks with smeared out intensity in the direction normal to the surface forming the so-called crystal truncation rods. (d) Crystalline thin films produce diffraction peaks and additional oscillations (fringes) in the direction normal to the surface. Taken from Ref. [28].

intensity of the diffraction spots is blurred in the direction normal to the surface forming crystal truncation rods (CTRs) [44, 45], as shown in Fig. 2.13.

Considering absorption effects, the diffraction amplitude of a semi-infinite crystal, which is limited in vertical direction, is given by

$$A_{substrate}\,(\boldsymbol{q}) = A_0\,C\,F\,(\boldsymbol{q}) \sum_{n_a=0}^{N_a-1} e^{\,i n_a\,\boldsymbol{q}\cdot\boldsymbol{a}} \sum_{n_b=0}^{N_b-1} e^{\,i n_b\,\boldsymbol{q}\cdot\boldsymbol{b}} \sum_{n_c=-\infty}^{N_c(n_a,n_b)} e^{\,i\,n_c\,\boldsymbol{q}\cdot\boldsymbol{c}}\; e^{\,n_c\epsilon} \quad . \tag{2.39}$$

Here, the factor $e^{\,n_c\epsilon}$ describes the attenuation due to the absorption within deeper layers and $N_c(n_a, n_b)$ gives the height variation in lateral direction considering the surface roughness (see Fig. 2.14).

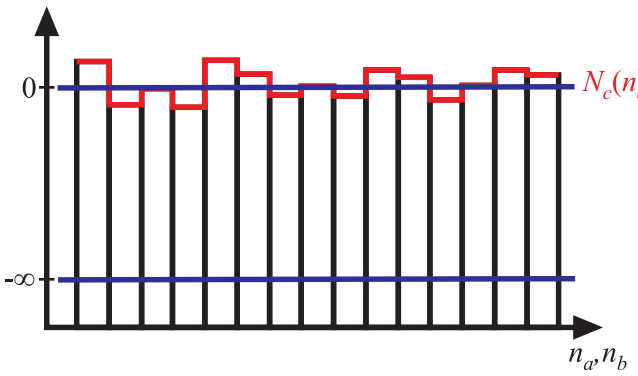

Fig. 2.14: Height distribution of a semi-infinite crystal surface. The profile is given by $N_c(n_a, n_b)$ with average height at zero level. Taken from Ref. [28].

Because the crystal is assumed to be infinite parallel to the surface, the diffracted intensity is located exclusively at the CTRs. Consequently, the Laue conditions are regarded as fulfilled in lateral direction leading to a simplification of Eq. (2.39). Thus, the diffraction amplitude along a CTR can be written as

$$A_{substrate}\,(\boldsymbol{q}) = A_0\,C\,F\,(\boldsymbol{q}) \sum_{n_a=0}^{N_a-1} 1 \sum_{n_b=0}^{N_b-1} 1 \sum_{n_c=-\infty}^{N_c(n_a,n_b)} e^{\,i\,n_c\,\boldsymbol{q}\cdot\boldsymbol{c}\,+\,n_c\epsilon} \tag{2.40}$$

$$= A_0\,C\,F\,(\boldsymbol{q}) \sum_{n_a=0}^{N_a-1} \sum_{n_b=0}^{N_b-1} \frac{e^{\,(i\,\boldsymbol{q}\cdot\boldsymbol{c}\,+\,\epsilon)\,N_c(n_a,n_b)}}{1-\,e^{\,-(i\,\boldsymbol{q}\cdot\boldsymbol{c}\,+\,\epsilon)}} \quad , \tag{2.41}$$

with the sums over n_a and n_b describing the average over the height profile $N_c(n_a, n_b)$. The diffracted amplitude along a CTR of a wave diffracted at a semi-infinite substrate is then given by

$$A_{substrate}\,(\boldsymbol{q}) = A_0\,C\,F\,(\boldsymbol{q})\,N_aN_b\,\frac{\left\langle e^{\,(i\,\boldsymbol{q}\cdot\boldsymbol{c}\,+\,\epsilon)\,N_c(n_a,n_b)}\right\rangle}{1-\,e^{\,-(i\,\boldsymbol{q}\cdot\boldsymbol{c}\,+\,\epsilon)}} \quad . \tag{2.42}$$

Assuming the height distribution $N_c(n_a, n_b)$ to be Gaussian shaped and setting the average height to zero level, the amplitude can be written as

$$A_{substrate}\,(\boldsymbol{q}) = A_0\,C\,F\,(\boldsymbol{q})\,N_aN_b\,\frac{e^{\,-\sigma^2\,(1\,-\,\cos\boldsymbol{q}\cdot\boldsymbol{c})}}{1-\,e^{\,-(i\,\boldsymbol{q}\cdot\boldsymbol{c}\,+\,\epsilon)}} \quad . \tag{2.43}$$

Here, σ is the standard deviation, which corresponds to the RMS (root mean square) roughness of the surface (cf. Sec. 2.5).

The diffraction at a thin film consisting of only a few layers can be described nearly in a similar way. However, the absorption can be neglected and the x-ray beam has to penetrate two surfaces at the top and at the bottom of the thin film. Here, two height functions $N_c^+(n_a, n, b)$ for the top and $N_c^-(n_a, n, b)$ for the bottom have to be considered (see Fig. 2.15). The average of the height distribution at the bottom is assumed to be at zero level and is at the top given by $\overline{N_c}$, which is the intermediate number of unit cells (film thickness).

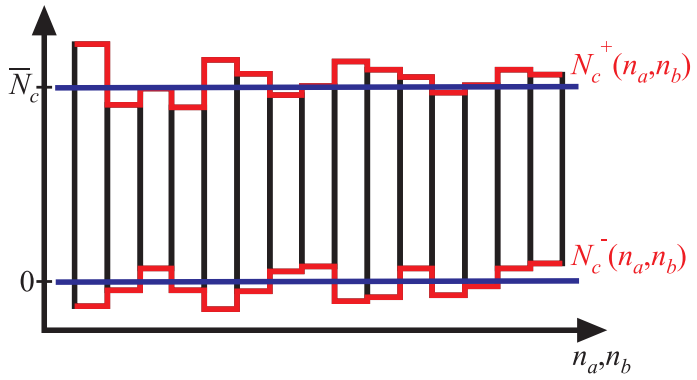

Fig. 2.15: Height distribution of the thin-film interfaces. The film exhibits an average thickness of $\overline{N}_c$. The roughness profile at the top and the bottom interface is given by the height profiles $N_c^+(n_a, n_b)$ and $N_c^-(n_a, n_b)$, respectively. Taken from Ref. [28].

Hence, the amplitude of a wave scattered at a thin film can be written as

$$A_{film}(\boldsymbol{q}) = A_0\, C\, F(\boldsymbol{q}) \sum_{n_a=0}^{N_a-1} 1 \sum_{n_b=0}^{N_b-1} 1 \sum_{n_c=N_c^-(n_a,n_b)}^{N_c^+(n_a,n_b)} e^{i\, n_c\, \boldsymbol{q}\cdot\boldsymbol{c}} \tag{2.44}$$

$$= A_0\, C\, F(\boldsymbol{q}) \sum_{n_a=0}^{N_a-1} \sum_{n_b=0}^{N_b-1} \frac{e^{i\,\boldsymbol{q}\cdot\boldsymbol{c}\,N_c^-(n_a,n_b)} - e^{i\,\boldsymbol{q}\cdot\boldsymbol{c}\,N_c^+(n_a,n_b)+1}}{1-e^{i\,\boldsymbol{q}\cdot\boldsymbol{c}}} \quad . \tag{2.45}$$

Analogous to Eq. (2.42), the sums can be simplified by averaging to

$$A_{film}(\boldsymbol{q}) = A_0\, C\, F(\boldsymbol{q})\, N_a N_b \frac{\left\langle e^{i\,\boldsymbol{q}\cdot\boldsymbol{c}\,u_c^-}\right\rangle - e^{i\,\boldsymbol{q}\cdot\boldsymbol{c}\,\overline{N_c}}\left\langle e^{i\,\boldsymbol{q}\cdot\boldsymbol{c}\,u_c^+}\right\rangle}{1-e^{i\,\boldsymbol{q}\cdot\boldsymbol{c}}} \quad , \tag{2.46}$$

with u_c^+ and u_c^- as the deviations from $\overline{N_c}$ at the top and the bottom of the film, respectively. Assuming the height distributions u_c^+ and u_c^- to be Gaussian shaped, the amplitude is given by

$$A_{film}(\boldsymbol{q}) = A_0\, C\, F(\boldsymbol{q})\, N_a N_b \frac{e^{-\sigma_-^2(1-\cos\boldsymbol{q}\cdot\boldsymbol{c})} - e^{i\,\boldsymbol{q}\cdot\boldsymbol{c}\,\overline{N_c}}\, e^{-\sigma_+^2(1-\cos\boldsymbol{q}\cdot\boldsymbol{c})}}{1-e^{i\,\boldsymbol{q}\cdot\boldsymbol{c}}} \tag{2.47}$$

Here, σ_+ and σ_- are the RMS roughnesses of the top and the bottom interface of the thin film.

For zero roughness the upper expression reduces to the form of the N-slit function [Eq. (2.36)] revealing an intensity profile shown in Fig. 2.12.

2.4.7 Diffraction at thin film layer systems

Typically, a thin film system consists of a crystalline substrate with one or more crystalline thin films on top. Assuming pseudomorphic growth the lateral positions of the CTRs of the film and the substrate coincide. Therefore, the diffracted amplitude can be expressed as a summation of all contributions considering the phase difference. The diffracted amplitude along a CTR for a system consisting of substrate and several thin films is given by

$$A_{system}\left(\boldsymbol{q}\right) = A_{substrate}\left(\boldsymbol{q}\right) + \sum_{i} \Theta_i \, e^{\,i\,\boldsymbol{q}\,\cdot\,\boldsymbol{p_i}} \, A_{film,i}\left(\boldsymbol{q}\right) \quad . \tag{2.48}$$

Here, Θ_i is the occupation factor of each individual film i, which takes into account impurities, dislocations or cavities inside the film. Further, the phase difference between the substrate and the layers is given by $\boldsymbol{q}\cdot\boldsymbol{p_i}$. The vector $\boldsymbol{p_i}$ is defined as

$$\boldsymbol{p_i} = \sum_{j=0}^{i-1} \boldsymbol{g_j} + \overline{N_{cj}}\boldsymbol{c_j} \quad . \tag{2.49}$$

The interface vector $\boldsymbol{g_j}$ defines the distance and lateral shift between layer j and $j+1$. Further, the phase shift due to the film thickness of layer j is given by $\overline{N_{cj}}\boldsymbol{c_j}$.

2.4.8 Study of the long-range order by x-ray diffraction

The following description considers exemplarily a binary compound consisting of A- and B-type atoms distributed on two different lattice sites namely α and β. In a stoichiometric composition and perfect order the α-sites are occupied solely by A-atoms and β-sites by B-atoms. Consequently, the structure factor $F(\boldsymbol{q})$ given in Eq. (2.31) can be divided into a sum over the α-sites and a sum over the β-sites

$$F\left(\boldsymbol{q}\right) = \sum_{\alpha}\Big(z_\alpha\, f_A(q) + w_\alpha\, f_B(q)\Big)\; e^{\,i\,\boldsymbol{q}\,\cdot\,\boldsymbol{r_\alpha}} + \sum_{\beta}\Big(z_\beta\, f_B(q) + w_\beta\, f_A(q)\Big)\; e^{\,i\,\boldsymbol{q}\,\cdot\,\boldsymbol{r_\beta}} \quad . \tag{2.50}$$

Here, for each kind of lattice sites an average form factor is used. The parameters z_α and z_β are fractions of the α- and β-site occupied by the correct atom A or B, respectively. In contrast, w_α and w_β are fractions of the α- and β-site occupied by the wrong atom B or A, respectively, with the relations $z_\alpha + w_\alpha = 1$ and $z_\beta + w_\beta = 1$. Note, vacant lattice sites are not considered within this model.

To quantify the long-range order, the parameter

$$S = z_\alpha + z_\beta - 1 = z_\alpha - w_\beta = z_\beta - w_\alpha \tag{2.51}$$

is usually introduced, also known as the Bragg-Williams parameter. In case of a stoichiometric and ordered composition, S equals 1 and $S = 0$ for a completely random arrangement of the A and B atoms within the crystal structure. Note, the parameter S is defined in a way that it is also convenient for a non-stoichiometric compositions. In this case, even the optimum distribution of the available atoms results in $S < 1$. In conclusion, Bragg reflections which are independent of the degree of order are called fundamental reflections, while reflections which depend on the ordering are called superstructure reflections. By measuring the intensity of the superstructure reflections the long-range order parameter S can be determined. A detailed description of order-disorder study by x-ray diffraction can be found in literature [47].

Reordering between tetrahedral and octahedral lattice sites in a spinel structure

The model above can be transferred to the (inverse) spinel structure to describe the reordering between tetrahedral and octahedral lattice sites in magnetite films. The total structure factor for the (inverse) spinel structure considering the contributions from different lattice sites can be written as

$$F_{tot}(\boldsymbol{q}) = F_{tetrahedral}(\boldsymbol{q}) + F_{octahedral}(\boldsymbol{q}) + F_{oxygen}(\boldsymbol{q}) \quad . \tag{2.52}$$

Figure 2.16 shows the calculated structure factor and the respective site contributions in $(22L)$ direction for a magnetite film. Here, it is clearly visible, that the superstructure (224) Bragg reflection originates exclusively from the Fe cations on tetrahedral lattice sites, while only Fe cations on octahedral lattice sites and O anions contribute to the fundamental (222) and (226) reflections. Therefore, it is possible to get information on the occupancy of the respective lattice sites and, thus, the ordering of the spinel lattice by comparing the intensities of these Bragg peaks [26, 28, 50].

Bertram *et al.* showed that the occupation of the tetrahedral lattice sites in thin magnetite films strongly depends on the deposition conditions, even if the stoichiometry of the magnetite is not affected [50]. In this case, the Fe^{3+} cations, which should occupy the tetrahedral lattice sites, are partly distributed to the octahedral vacancies of the spinel lattice. Transferring Eq. (2.50) to this situation, one obtains

$$F(\boldsymbol{q}) = \sum_{tet} z_{tet}\, f_A(q)\; e^{\,i\,\boldsymbol{q}\cdot\boldsymbol{r_{tet}}} + \sum_{oct}\Big(f_B(q) + w_{oct}\, f_A(q)\Big)\; e^{\,i\,\boldsymbol{q}\cdot\boldsymbol{r_{oct}}} + \sum_{oxy} f_O(q)\; e^{\,i\,\boldsymbol{q}\cdot\boldsymbol{r_{oxy}}} \tag{2.53}$$

Here, $f_A(q)$ is the form factor of the Fe^{3+} cations, $f_B(q)$ the average over the form factors for the Fe^{2+} and Fe^{3+} cations and $f_O(q)$ the form factor of the oxygen anions. z_{tet} is the fraction of the correctly occupied tetrahedral lattice sites and w_{oct} is the fraction of the octahedral lattice sites occupied by the wrong Fe^{3+} cation. Since there are no wrong cations on tetrahedral lattice sites, $w_{tet} = 0$, and since the 'right' Fe^{2+}/Fe^{3+} cations are not relocated, $z_{oct} = 1$. Further, the relation $z_{tet} + w_{oct} = 1$ becomes immediately obvious. Hence, this case is a modification of the model introduced above. Further, the occupation of the oxygen lattice sites remains unaffected. Extending and rewriting Eq. (2.53), the structure factor can be expressed as

$$F(\boldsymbol{q}) = (1 - w_{oct})\, F_{Fe_3O_4}(\boldsymbol{q}) + w_{oct}\, F_{Fe_{0.75}O}(\boldsymbol{q}) \quad , \tag{2.54}$$

with $F_{Fe_3O_4}$ as the structure factor of an ideal magnetite structure and $F_{Fe_{0.75}O}$ as the structure factor of an defective rock salt like structure with the same stoichiometry as magnetite but without tetrahedrally coordinated iron ions. Here, w_{oct} directly represents the parameter of disorder.

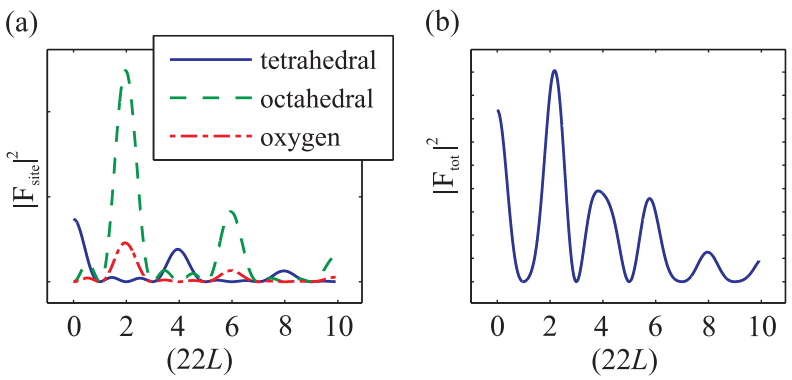

Fig. 2.16: (a) Contributions of the different magnetite lattice sites to the structure factor. (b) The total structure factor of magnetite. The calculations are done along the $(22L)$-CTR of the spinel lattice. Taken from Ref. [28].

2.5 X-ray reflectivity

X-ray reflectivity (XRR) is a surface and interface sensitive technique based on the interference of electromagnetic waves reflected at different interfaces. During the experiment, the sample is irradiated with x-rays at a small incidence angle α_i, which is typically below 5° for x-rays in the wavelength region of $\sim 1.0 - 1.5\,\text{Å}$. The reflected intensity at the angle of reflection $\alpha_f = \alpha_i$ is recorded as a function of the incidence angle α_i (cf. Fig. 2.17). The resulting intensity distribution of the reflected beam contains information on the structural properties like the stacking order of multilayers, the refractive index (dispersion and absorption) of each layer, the layer thicknesses, surface and interface roughnesses. In Fig. 2.17, a sketch of a reflectivity experiment is presented.

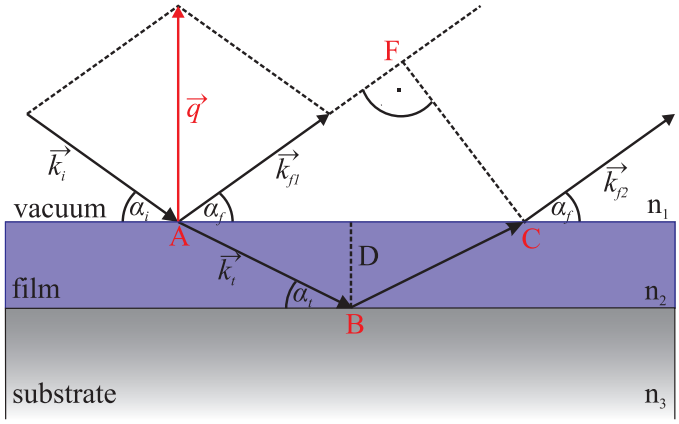

Fig. 2.17: Incoming wave with wave vector $\boldsymbol{k_i}$ hits the surface at the angle α_i and is partly reflected ($\boldsymbol{k_f}$) and partly transmitted ($\boldsymbol{k_t}$) at each interface between two optically different media with the refractive indices n_x ($x = 1, 2, 3$). The reflected intensity is recorded at the angle of reflection $\alpha_f = \alpha_i$ as a function of the scattering vector $\boldsymbol{q} = \boldsymbol{k_f} - \boldsymbol{k_i}$, which is varied during the measurement by changing the incidence angle α_i.

Due to energy conservation, the wavenumber in vacuum is denoted $|\boldsymbol{k_i}| = |\boldsymbol{k_f}| = k$ and in the material it is $nk = |\boldsymbol{k_t}|$. Further, each incidence angle refers to a scattering vector $\boldsymbol{q} = \boldsymbol{k_f} - \boldsymbol{k_i}$, which has only a component normal to the surface. Thus, its magnitude is given by

$$q = 2k \sin \alpha_i = \frac{4\pi}{\lambda} \sin \alpha_i \tag{2.55}$$

and is varied during the measurement by changing the incidence angle α_i and keeping $\alpha_f = \alpha_i$.

The reflectivity and transmissivity of a material depend on the complex index of refraction n. In the case of a homogeneous medium and x-ray energies far from absorption edges, the refractive index n can be approximated by

$$n = 1 - \delta + i\beta \quad \text{with dispersion} \quad \delta = \frac{\lambda^2}{2\pi} r_e \rho \quad \text{and absorption} \quad \beta = \frac{\lambda}{4\pi}\mu \ . \tag{2.56}$$

Here, λ is the x-ray wavelength, r_e the classical electron radius, ρ the electron density and μ the absorption coefficient. For vacuum, δ equals 0 and for x-rays in solid materials δ is typically in the range of $10^{-4} - 10^{-6}$ leading to a real part of the refractive index being slightly smaller than one. Consequently, it is always possible to observe total external reflection at the interface between air/vacuum ($n = 1$) and solid state media using x-ray energies and small incidence angles. The critical angle for total reflection can be calculated using Snell's law and is approximately

$$\alpha_c \approx \sqrt{2\delta} \ . \tag{2.57}$$

Above the critical angle, parts of the x-rays penetrate into the material resulting in a decrease of the reflected intensity (cf. Fig. 2.18).

The reflectivity of a material is defined as the intensity ratio of the reflected and incident wave $R = I^r/I^i$ and is connected to the complex reflection coefficient $r_{s/p}$ by the relation $R = \left|r_{s/p}\right|^2$. Here, the indices s and p denote s- and p- polarized light, respectively. The transmissivity $T = I^t/I^i = \left|t_{s/p}\right|^2$ can be described analogously. Due to $n \approx 1$ for x-rays the optical coefficients for s- and p-polarized light can be expressed in the same way by the Fresnel formulas

$$r_{s,p} = \frac{k_{i,z} - k_{t,z}}{k_{i,z} + k_{t,z}} \quad \text{and} \quad t_{s,p} = \frac{2k_{t,z}}{k_{i,z} + k_{t,z}} \quad . \tag{2.58}$$

Here, $k_{i,z} = k \sin\alpha_i$ and $k_{t,z} = nk \sin\alpha_t = k\sqrt{n^2 - \cos^2\alpha_i}$ describe the vertical components of the wave vectors $\boldsymbol{k_i}$ and $\boldsymbol{k_t}$, respectively.

In Fig. 2.18, a theoretically calculated reflectivity curve is depicted as a function of scattering vector q at a pure substrate assuming a infinite thickness. For small incidence angles, the sample surface is irradiated only by a part of the x-ray beam leading to a linear increase of the reflected intensity until the angle α_{fp} is reached. This effect is called footprint and is due to the finite size of the sample and the spatial extension of the beam. For a sample with length l in beam direction and a rectangular beam profile with a height b_i, the angle α_{fp} is given by $\alpha_{fp} = \arcsin(b_i/l)$. At this angle, the sample is illuminated by the entire beam.

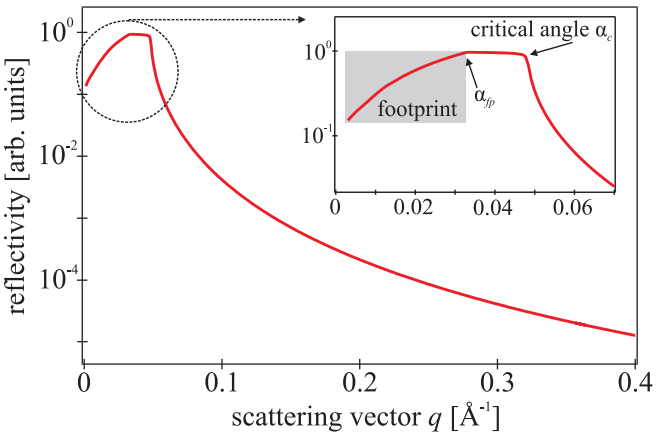

Fig. 2.18: Calculated reflectivity curve for the reflection at a single surface. Note the logarithmic scaling of the y-axis. The inset shows the reflectivity at small scattering angles. Due to a finite size of the sample and the extension of the beam, the intensity increases until the footprint angle α_{fp} is reached. The reflectivity of 1 describes the total reflection of the incident wave. At the critical angle α_c parts of the x-rays are transmitted into the material resulting in a decrease of the reflected intensity.

2.5.1 Reflection at multiple interfaces

For a multilayer system, a part of the transmitted beam can be reflected at the next interface and again transmitted at the first interface, contributing to the total measured intensity. Consequently, also the reflection and transmission at each additional interface have to be considered for correct description of the reflected intensity. The total reflectivity of a multilayer system can be calculated using a recursive approach established by Parratt [51]. This so-called Parratt algorithm for N layers is a recursive expression of the reflected amplitude $R_{j-1,j}$ at the interface between the j-th and the $(j-1)$-th layer and is given by

$$R_{j-1,j} = \frac{r_{j-1,j} + R_{j,j+1} \exp\left(iD_j q_j\right)}{1 + r_{j-1,j}\, R_{j,j+1} \exp\left(iD_j q_j\right)} \quad \text{for } j \in \{1, ..., N\} \quad . \tag{2.59}$$

Here, $r_{j-1,j}$ is the Fresnel coefficient at the interface between layer j and layer $j-1$, which can be calculated by

$$r_{j-1,j} = \frac{q_{j-1} - q_j}{q_{j-1} + q_j} \quad . \tag{2.60}$$

Further, D_j is the layer thickness and $q_j = n_j 2k \sin\alpha_t = 2k\sqrt{n_j^2 - n_{j-1}^2 cos^2\alpha_i}$ is the scattering vector in layer j. Here, solely the vertical component $q_j = q_{z,j} = 2k_{z,j}$ is essential, since the scattering components parallel to the surface are zero. The substrate is denoted as 'layer $N+1$' and the vacuum/air as 'layer 0'. Since an infinite thickness of the substrate is assumed, there is no reflection at the bottom of the substrate and the starting point of the recursive calculation is $R_{N,N+1} = r_{N,N+1}$. By successive insertion of $R_{j,j+1}$ in Eq. (2.59), the total specularly reflected intensity is obtained after N iterations as $R = I^r/I^i = |R_{0,1}|$.

Figure 2.19 shows the calculated intensity of a 10 nm thick layer on a infinite thick substrate. The intensity oscillations are due to alternately appearing constructive and destructive interference of the beams reflected at the air/film interface and the film/substrate interface. Analogously to the Bragg condition (cf. Sec. 2.4), the thickness D of the film can be approximated by determination of the distance Δq between two oscillations: $D \approx 2\pi \,/\, \Delta q$. In

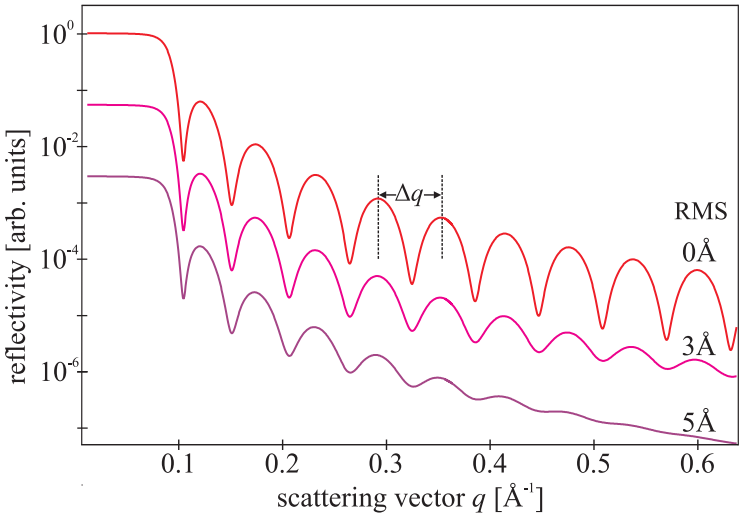

Fig. 2.19: Calculated reflectivity curves for a 10 nm thick film on a substrate with different RMS roughnesses of the interface between film and substrate. The thickness $D \approx 2\pi \,/\, \Delta q$ of the film can be estimated from the distance Δq between two oscillations. The footprint is not considered here.

case of a multilayer system, the determination of the respective thicknesses is more complicated due to multiple interference conditions. Therefore in this work, an in-house developed fitting tool was applied for the analysis of the reflectivity curves [52]. The fitting of the modeled reflectivity to the experimental data allows to determine thickness, dispersion, absorption of each layer but also the stacking order of multilayer systems. Additionally, the interface roughness is an important fitting parameter, which strongly affects the shape of the reflectivity curve. Its influence will be discussed in the following.

2.5.2 Influence of interface roughness

So far, for the description of reflectivity, only perfectly sharp interfaces are considered. This has been taken into account by a constant index of refraction n_j which abruptly jumps to the value n_{j+1} at the boundary. However, this is not true for real materials exhibiting a distinct interface roughness. For this purpose, the refractive index has to be described as a continuous variation $n_j(x,y,z)$ in all three spacial directions. Since for reflectivity only the specular component is

crucial, the refractive index can be expressed as one-dimensional depth profile

$$n_j(z) = \int\int n_j(x,y,z)\,dx\,dy = \langle n_j(x,y,z)\rangle_{x,y} \tag{2.61}$$

laterally averaged over (x, y). Further, a rough interface is described by an ensemble of smooth interfaces with coordinates $z_j + z$ weighted by a probability density $P_j(z)$ [cf. Fig. 2.20(a)].

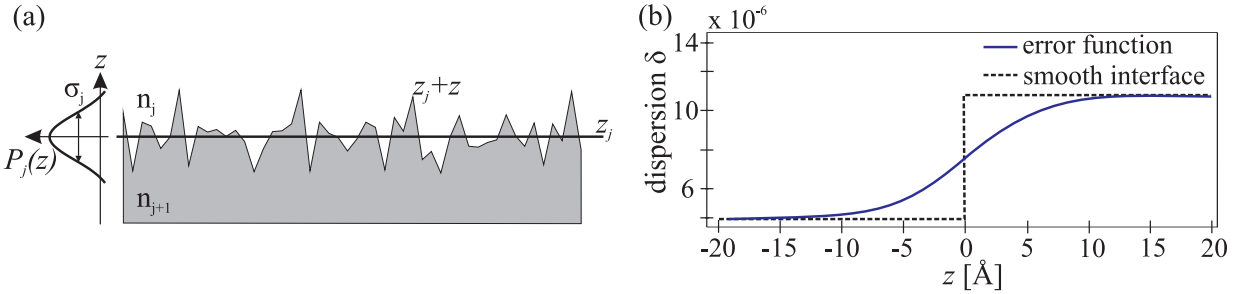

Fig. 2.20: (a) Rough interface with mean z-coordinate z_j and fluctuations z around this value. This surface is described as an ensemble of smooth surfaces at coordinates $z_j + z$ with probability density $P_j(z)$ and standard deviation σ_j. (b) Density profile of an error function for a transition from $\delta = 4.4{\times}10^{-6}$ to $\delta = 5.9{\times}10^{-6}$ and a RMS roughness of 5 Å. Adapted from Refs. [52, 53].

Thus, a continuous refractive-index profile is assumed between the layers j and $j+1$, which can be written as

$$n_j(z) = \frac{n_j + n_{j+1}}{2} - \frac{n_j - n_{j+1}}{2}\,\mathrm{erf}\left(\frac{z - z_j}{\sqrt{2}\,\sigma_j}\right) \tag{2.62}$$

with the error function

$$\mathrm{erf}(z) = \frac{2}{\sqrt{\pi}}\int_0^z \exp(-t^2)\,dt \quad . \tag{2.63}$$

In this case, a Gaussian probability density of the interface heights

$$P_j(z) = \frac{1}{\sqrt{2\,\pi}\,\sigma_j}\,\exp\left(-\frac{z^2}{2\,\sigma_j^2}\right) \tag{2.64}$$

results. Here, $\sigma_j^2 = \langle z^2\rangle - \langle z\rangle^2$ is the variance of the height distribution with the standard deviation σ_j. The value σ_j is also known as the RMS (root mean square) roughness of a layer and is an important fitting parameter, which strongly influences the shape of the reflectivity curve (cf. Fig. 2.19). In Fig. 2.20(b), a profile of an error function is presented for a RMS value of 5 Å. Finally, these considerations lead to a modified Fresnel coefficient for reflection

$$\tilde{r}_{j-1,j} = r_{j-1,j}\,\exp\left(-2\,k_{z,j-1}\,k_{z,j}\,\sigma_j^2\right) \quad , \tag{2.65}$$

which has to be replaced in the recursive formula of Eq. (2.59). The exponential factor is called the Nevot-Croce factor [54]. If $\sigma_j \to 0$ the expression for the sharp interface case is regained.

The introduced roughness model is only valid if the roughness is much smaller than the thickness of the respective layer. For other roughness types, models such as layer segmentation etc. can be used.

2.6 Low-energy electron diffraction

Low-energy electron diffraction (LEED) is based on the elastic backscattering of low-energy electrons ($10 - 500\,\mathrm{eV}$) incident normally to the sample surface containing information on the structure and morphology of the investigated surface. Thereby, the De Broglie wavelength of such an electron beam is in the magnitude of the atomic distances in crystal lattices making it suitable for diffraction. Further, the minimum of the universal pathlength curve is located in this energy region leading to high surface sensitivity (typically ≈ 3 atomic layers) of this method. For electron diffraction the same Bragg formula Eq. (2.17) as for x-rays is applicable. Due to

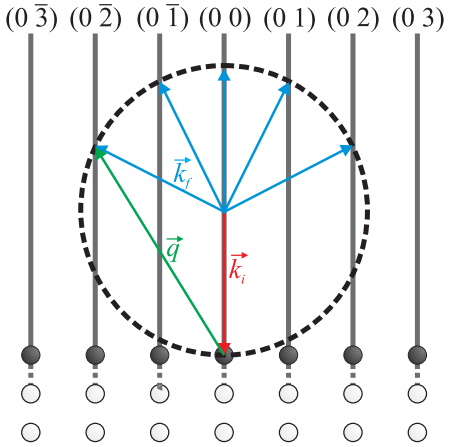

Fig. 2.21: Ewald sphere construction for an electron beam with the wave vector $\boldsymbol{k}_i$ incident normal to the surface. The Ewald sphere (dashed line) is defined by the set of all possible exiting wave vectors $\boldsymbol{k}_f$. Diffraction spots will appear whenever the Ewald sphere is intercepting a Bragg rod (solid lines). Here, only diffracted beams within the plane with Miller indices $h = 0$ are shown.

the two-dimensional character of the measured area, the periodically repeated distance normal to the surface becomes infinite forming reciprocal lattice rods instead of Bragg peaks. Figure 2.21 presents the Ewald construction for an electron beam incident normal (along (0 0) direction) to the sample surface. Here, only the plane with the Miller index $h = 0$ is shown. The Ewald sphere is defined by the set of all possible exiting wave vectors $\boldsymbol{k}_f$. The radius is given by the magnitude of the wave vector $|\boldsymbol{k}_f| = |\boldsymbol{k}_i|$ due to elastic scattering. The resulting pattern represents the intersection of the Ewald sphere with the reciprocal lattice rods. As a consequence, diffraction may occur at all energies of the incident beam. Due to a fixed incidence angle of the electron beam in LEED experiments, the scattering condition can only be changed by changing the energy of the beam. This leads to a variation of the Ewald sphere radius and, thus, to a modified number and positions of the intercepts of the sphere with the Bragg rods.

The observed LEED pattern reflects directly the symmetry and the unit cell size of the reciprocal lattice in lateral direction. However, any periodical modification of the surface, such as reconstruction, overlayer adsorption or terraces (steps) may cause additional diffraction spots. In general, the observed diffraction pattern contains statistic information on large parts of the radiated surface. Therefore, local point defects, which are not periodically ordered, result only in an increased diffuse background and have no impact on the diffracted intensity. In contrast, periodically distributed defects like atomic steps, dislocation networks, domain boundaries or mosaics lead to a modified intensity distribution [55]. Therefore, analysis of spot intensities and widths reveals not only qualitative but also quantitative information on the density of line defects. Further, small bulk contributions can be seen as an intensity modulation along the rod.

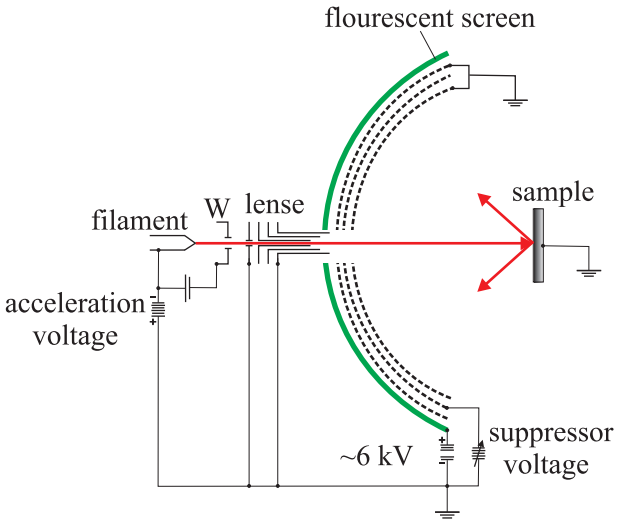

Fig. 2.22: Schematic diagram of conventional three-grid LEED optics consisting of a filament, a Wehnelt cylinder (W), an electrostatic lens system and a fluorescent screen. The three-grid system is used for electron acceleration and suppression of inelastically scattered electrons.

A typical experimental arrangement of a LEED experiment is shown in Fig. 2.22. An electron beam of variable energy is produced by an electron gun and is incident normal to the sample surface. The electron gun consists of a cathode, the Wehnelt cylinder (W) and an electrostatic lens system allowing to collimate, focus and accelerate the electron beam. Typically, in a LEED experiment the electron beam is focused on the detector to achieve narrow diffraction peaks. However, if it is necessary to study only small sample areas, focusing the beam on the surface is also possible, which will lead to a broadening of the diffraction peaks. The backscattered electrons are accelerated onto a grid system and detected by a spherical fluorescent screen. For this purpose, the screen is set at a high positive potential (of about 6 keV) to provide the electrons with enough energy for the excitation of fluorescence. Further, the middle grid is kept on an adjustable negative potential to suppress the inelastically scattered electrons and, thus, minimize the diffuse background. The observed LEED pattern is recorded by a camera placed on the rear side of the screen system.

2.7 X-ray photoemission spectroscopy

X-ray photoemission spectroscopy (XPS) provides information on the electronic structure and chemical composition of the investigated material and can be exploited with either soft (SXPS) or hard x-rays (HAXPES) to vary the surface/bulk sensitivity. This technique is based on the photoelectric effect, which describes the excitation of an electron onto the high-energy continuum state by a photon. This emitted electron can be detected as a photoelectron. The spectroscopic process is shown schematically in Fig. 2.23. The kinetic energy E_{kin} of the emitted photoelectron can be written as

$$E_{kin} = h\nu - E_b - \phi \tag{2.66}$$

considering the energy conservation law. Here, $h\nu$ is the energy of the incident photons, E_b is the binding energy of a photoelectron and ϕ is the work function, which is the energy an electron has to overcome to leave the solid. In case of conductive samples, the sample and spectrometer are connected at a common electrical potential leading to equal Fermi levels. Thus, the work function in Eq. (2.66) is given by the work function of the spectrometer. Consequently, the value of E_b can be estimated from the XPS spectrum by measuring the kinetic energy of the emitted electrons if ϕ is known. Usually, the spectrometer is calibrated using a well known reference level

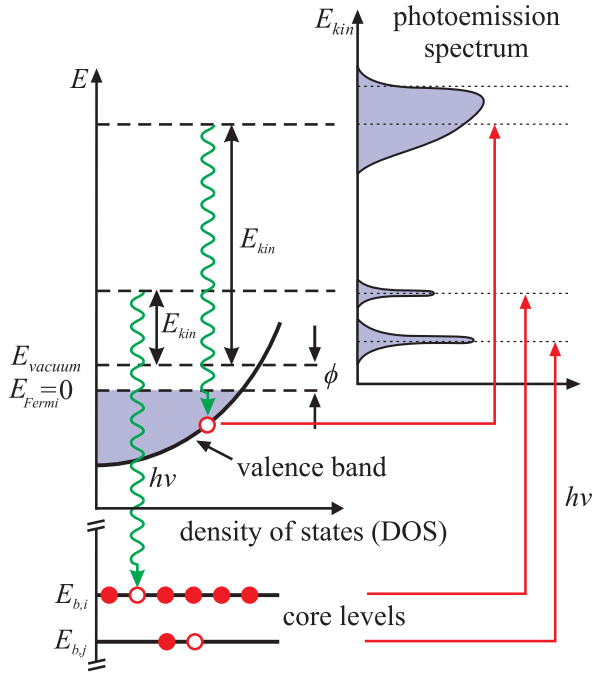

Fig. 2.23: Schematic drawing of the photoemission process including an energy level diagram. Electrons are excited from occupied states into the quasi-continuum by absorbing a photon of the energy $h\nu$. After excitation, the photoelectrons are detected with the kinetic energy $E_{kin} = h\nu - E_b - \phi$. The work funktion is given by $\phi = E_{vacuum} - E_{Fermi}$. Adapted from Ref. [28].

like the Au $4f$ line. In addition, for solid samples, the energies are calibrated in such a way that the Fermi level corresponds to $E_b = 0\,\text{eV}$.

The information depth of an XPS experiment is limited by the inelastic mean free path (IMFP) of the emitted electrons. It depends on the investigated material but also on the kinetic energy of the emitted electrons. For soft x-rays of 1000 eV, the IMFP is approximately in the range of a few nanometers, making SXPS a surface sensitive method. A higher bulk sensitivity can be achieved by increasing the energy of the incident x-rays creating higher energy electrons that have larger escape depths, like it is the case for HAXPES. Further, due the extremely small IMFP of the emitted photoelectrons under ambient conditions, XPS experiments are typically performed in ultra-high vacuum (UHV).

In the experiment, only electrons without energy loss contain direct information on the electronic structure of the investigated material. Their positions in the spectrum directly correspond to the element specific binding energies of the atomic core levels providing information on the elements present in the sample. The electrons, which suffer energy loss through inelastic scattering but still have sufficient energy to leave the solid, will contribute to a background signal. In addition, a number of different effects can influence the shape and positions of the photoemission peaks during the experiment. The most important effects will be briefly introduced in the following sections. A more detailed description of the photoemission process and spectral characteristics can be found elsewhere [56–58].

The basic experimental setup used in a laboratory is schematically pictured in Fig. 2.24 and consists of an x-ray source, electron optics, an energy discriminative electron analyzer and an electron detector. Typically, the x-ray tube is equipped with two anodes providing photons of the energy Al K$\alpha_{1/2}$ = 1486.6 eV and Mg K$\alpha_{1/2}$ = 1253.6 eV. Within the experiment, a sample is excited with x-rays of a certain energy causing photoelectrons, which are emitted with a range of energies and directions. A part of the photoelectrons, which are ejected under the angle θ, is collected and focused onto the analyzer entrance using a set of electrostatic and magnetic lens units and slits. Electric fields within the hemispherical analyzer are applied and force the electrons on a predefined trajectory. Thus, only photoelectrons of a given energy can pass the analyzer and reach the detector. The detector itself consists of a microchannel plate (MCP) or

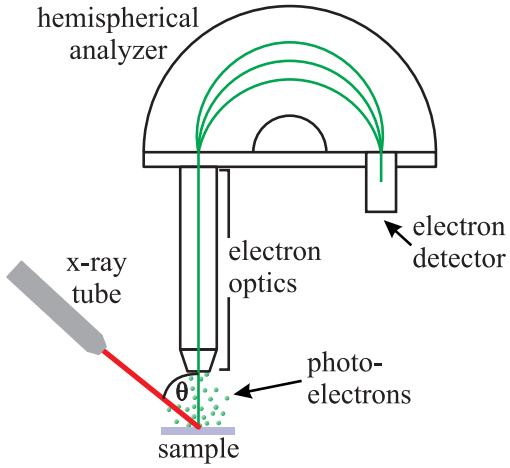

Fig. 2.24: Basic components of an XPS setup including an x-ray tube, a hemispherical electron analyzer, electron optics and an electron detector. A sample is irradiated with x-rays leading to an emission of photoelectrons. Electrons ejected under the angle θ are collected and focused using the electron optics, which involves electrostatic and/or magnetic lenses and apertures. By applying electrostatic fields within the hemispherical analyzer, only electrons of a given energy can pass the analyzer and reach the detector. Adapted from Ref. [28].

of several channel electron multipliers (CEM's) arranged as a single block.

The analyzer and the lens system can be utilized in two operation modes. Typically, the so-called fixed analyzer transmission mode (FAT) is used. In this mode, the kinetic energy of the electrons is reduced by the lens system to a certain pass energy E_p before they enter the analyzer. However, the pass energy of the analyzer itself is held on a constant value, thus a constant energy resolution for the whole spectrum can be achieved. The use of a lower pass energy increases the absolute energy resolution of the recorded spectra but reduces the overall intensity of the XPS signal. An alternative mode is the so-called fixed retarding ratio (FRR), which is usually used to record Auger spectra. Here, the retarding factor of the lens system is kept constant while the pass energy of the analyzer is varied allowing electrons with different kinetic energies reach the detector. Consequently, the resolution scales with the electron energy. This mode allows to resolve broad peaks of small intensity at low kinetic energies.

2.7.1 Binding energy and chemical shift

The binding energy of a photoelectron can be written as the energy difference

$$E_b = E_f(n-1) - E_i(n) \tag{2.67}$$

between the atomic final state E_f with $(n-1)$-electrons and the atomic initial state E_i with n-electrons. According to Koopmans' theorem, the core level energy E_b measured after an ionization event is nearly equal to the negative ε_{HF} orbital energy of a neutral ground state, calculated using the Hartree-Fock method. However, the assumption that other electrons remain 'frozen' during photoemission is not valid due to relaxation of the surrounding electrons. Here, contributions to the relaxation energy depend on both the potentials created by valence electrons of the atom containing the core hole (atomic relaxation) and the potentials created by its surrounding atoms (extra-atomic relaxation). Further, electron correlation and relativistic effects are not considered in the Koopmans/Hartree-Fook model. However, the correlation and relativistic energies are rather small and can usually be neglected. The deviation of the measured binding energy from the free atom value, which is denoted as the chemical shift, provides information on the chemical bonding of the detected electrons.

One basic approach to describe the chemical shift is the charge potential model [59, 60]. Within this model, the shift in the binding energy is correlated with the charge on the atom, and not

with its formal oxidation state. The effective binding energy $E_{b,eff}$ is given by

$$E_{b,eff} = E_b^\circ + kq_i + \sum_{j \neq i}(q_j/r_{ij}) \quad , \tag{2.68}$$

where E_b° is the reference energy (usually equal to E_b of a neutral atom), q_i the charge of the atom i, k an empirical parameter, and q_j the charge of the surrounding atoms j at distances r_{ij}. Consequently, the chemical shift can be written as

$$\Delta E_b = k\Delta q_i + \Delta V_i \quad . \tag{2.69}$$

The term $k\Delta q_i$ represents the potential change in the atom containing the core hole and ΔV_i denotes the potential change in the surrounding atoms.

An example for a chemical shift of a Fe $2p$ signal is given in Fig. 2.25. Here, the binding energy of the Fe $2p$ electron in FeO is higher than in the Fe metal. Thus, a Fe $2p$ electron in Fe has a weaker Coulomb interaction with the nucleus than a Fe $2p$ electron in FeO.

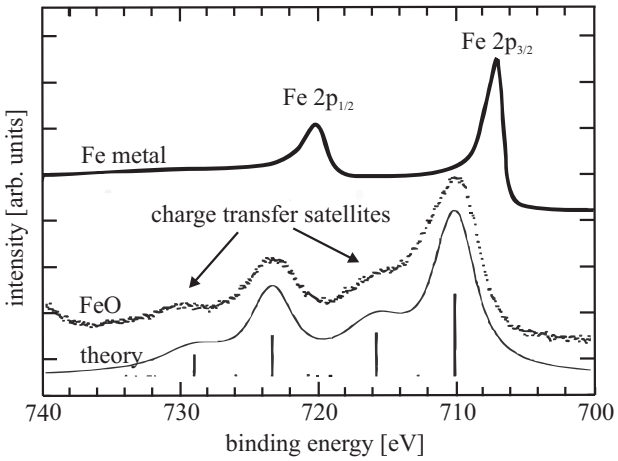

Fig. 2.25: Fe $2p$ core level lines of Fe metal and FeO. For iron oxide a clear chemical shift to higher binding energies of the Fe $2p$ peaks is visible, if comparing to the signal of pure iron metal. In addition, FeO shows characteristic charge-transfer satellites. FeO spectra and theoretical calculation are adapted from Ref. [61].

2.7.2 Spectral features

Besides the main lines, there is a variety of effects leading to additional intensity in the XPS spectra. Some of them give rise to distinct lines, while others result in broad features or contribute to the inelastic background.

Spin-orbit coupling

For electrons with an angular momentum $l > 0$ the photoemission lines split into two peaks with discrete energies due to magnetic interaction between the spin s of the electron in the final state and the orbital angular momentum l (cf. Fig. 2.25). The intensities of the lines are defined by the ratio of the respective degeneracies $2j + 1$ (quantum number $j = |l \pm s|$).

Satellites

Additional spectral features in XPS spectra are the so-called satellite lines typically located on the high energy side of the main peaks. Satellites which are due to intraatomic excitations are called intrinsic satellites. Here, photoelectrons suffer energy loss through excitation of a second

electron during the photoemission process. If this additional electron is excited to an unoccupied higher energy level, this peak is called 'shake-up' satellite. Shake-up peaks have discrete energies because the energy loss belongs to a specific quantitized energy transition. Photoemission loss peaks arising from excitations into the continuum, are called 'shake-off' satellites. These peaks have a wide range of possible energies and occur as a broad feature typically hidden within the background signal.

Extrinsic satellites originate from intraatomic relaxations. One possibility is the so-called charge-transfer process often apparent for transition metal oxides. In the case of FeO, an electron from the oxygen $2p$ orbital is transferred to the metal $3d$ orbital of the iron (see Fig. 2.25). The energy Δ required for this extrinsic charge transfer process is given by

$$\Delta = E(3d^{n+1}L^{-1}) - E(3d^nL) \tag{2.70}$$

and is taken from the primary photoelectron leading to satellite lines located at higher binding energies in the spectra of many transition metal oxides such as FeO, NiO etc. Here, n denotes the number of electrons in the respective orbital, L the oxygen ligand from which the electron is transfered to the $3d^n$ orbital and L^{-1} the corresponding ligand hole. Note, charge transfer effects can not only occur in atomic final states but already in atomic ground states.

Further satellites in conductive materials can occur as a result of a plasmon excitation during the photoemission process. Plasmon vibrations lead to characteristic, periodic energy losses in the XPS spectra due to the excitation of several plasmons at the same time.

Multiplet splitting

Multiplet splitting originates from interactions between spins of the remaining unpaired electrons (after photoemission) in the ionized core states with unpaired electrons in the valence band. Due to variety of different coupling processes, this may result in a lot of possible final state configurations with as many different energies after the photoemission. Since various final state effects, e.g., spin-orbit splitting or charge-transfer satellites, have to be considered, this can lead to complex multiplet structures containing a huge quantity of photoemission lines.

2.7.3 Quantitative analysis and depth profiling

By analyzing XPS spectra, it is possible to get quantitative information about the chemical composition of a surface or a thin film. For this purpose, the areas enclosed by the emission peaks have to be determined, corrected by several factors, such as instrumental effects, and weighted by the photoionization cross section for the specific element and atomic subshell. It has to be noted that a background has to be subtracted from the data prior to the determination of the areas under the peaks. In this work, the well known Shirley background has been subtracted [62]. Resulting areas under the photoemission peaks are directly related to the relative amount of each element (except for H and He) present in the sample.

The integrated intensity of an inner shell orbital j from element i of a film with thickness t_f can be calculated as [57, 58]

$$I_{ij} = S_i^j \int_0^{t_f} e^{-z/\lambda_i^*} dz = S_i^j \lambda_i^* \left(1 - e^{-t_f/\lambda_i^*}\right) \quad . \tag{2.71}$$

Here, z is the depth of the emitted photoelectron measured from the sample surface and $\lambda_i^* = \lambda_i \cos\varphi$ the effective IMFP at angle φ between detector and surface normal, where λ_i de-

scribes the IMFP for electrons of the element i at a given kinetic energy. The constant S_i^j for an orbital j of the element i is determined by

$$S_i^j = \Phi(h\nu) \times \sigma_i^j(h\nu) \times D(\mathrm{KE}) \times N_i \times A \quad , \tag{2.72}$$

with x-ray flux Φ at an energy $h\nu$, the photoionization cross section σ_i^j, the spectrometer efficiency $D(\mathrm{KE})$, the number of atoms per unit volume N_i and the analysis area A. The parameter $D(\mathrm{KE})$ includes the efficiency of the collection lenses, energy analyzer, and detector for a given kinetic energy KE of the photoelectrons.

Typically, content ratios of the elements are calculated. Hence, it is not necessary to determine the absolute values in Eq. (2.71). Thus, some quantities included in S_i^j like the x-ray flux Φ and analysis area A (in most cases) will cancel out. Further, most instruments are operating in the so-called FAT mode which means that all electrons are retarded by the collection lens to a constant pass energy E_p (see Sec. 2.7). Thus, only the efficiency of the collection lenses, which can be determined experimentally, has to be considered within the parameter $D(\mathrm{KE})$. Usually, information about the transmission functions of the spectrometer is provided by the manufacturers. The IMFP λ_i of photoelectrons as a function of their KE can be estimated using the TPP-2M formula [63]. Further, the angular distribution of the photoelectrons is generally not isotropic and has to be considered in terms of a differential photoionization cross section. In most cases, the electric dipole approximation provides a sufficient description of the photoionization cross section for circularly polarized and unpolarized photons, which results in [64]

$$\frac{d\sigma_i^j}{d\Omega} = \frac{\sigma_i^j}{4\pi}\left[1 - \frac{\beta_i^j}{2} P_2(\cos\vartheta)\right] \quad . \tag{2.73}$$

Here, β_i^j is the angular asymmetry parameter which depends on the energy, the element i and the j-th atomic subshell. The term $P_2(\cos\vartheta)$ is the second order Legendre polynomial and ϑ is the angle between the propagation direction of the photons and the photoelectrons. However, in most lab systems the x-ray source is mounted in the so-called 'magic angle' configuration, that is, 54.7° with respect to the analyzer. In this case, the second-order Legendre polynomial becomes zero. The element and orbital specific photoionization cross sections $\sigma_i^j(h\nu)$ for Al Kα and Mg Kα are then available in tabulated works, e.g., sensitivity factors calculated by Scofield [65].

A more precise description of the angular distribution of the photoelectrons including dipole and quadrupole terms for circular polarized and unpolarized as well as for linearly polarized photons is given in Ref. [64]. Tabulated values of σ_i^j, β_i^j and of the nondipolar parameters for nearly all subshells of atoms (up to $Z = 54$) for various photon energies can be found in the comprehensive work of Trzhaskovskaya *et al.* [66, 67].

To calculate the XPS intensity in a multilayer system the attenuation from each overlying layer has to be considered. According to Lambert-Beer's law, the intensity I_b^m for a bulk material covered by n homogeneous layers can be written as

$$I_b^m = S_b^j \lambda_b^* \prod_{i=1}^{n} e^{-t_i/\lambda_i^*} \quad , \tag{2.74}$$

with the term $S_b^j \lambda_b^*$ as the intensity for a pure bulk material obtained by the limit $t_f \to \infty$ from Eq. (2.71). Consequently, the intensity I_f^m of layer f in a multilayer system of n layers which is

attenuated by $(n - f)$ layers is given by

$$I_f^m = S_f^j \lambda_f^* \left(1 - e^{-t_f/\lambda_f^*}\right) \prod_{i=f+1}^{n} e^{-t_i/\lambda_i^*} \quad . \tag{2.75}$$

Depth-profile measurements of the chemical composition can be realized by varying the emission angle at which the electrons are collected. Consequently, electrons from different depths are detected due to the angle dependence of λ_i^*, and σ_i^j. Here, the angle φ between detector and surface normal is relevant to determine the escape depth of the photoelectrons and, thus, the information depth of the measurement. A variation of the emission angle can be achieved either by tilting the sample with respect to the analyzer or by using a wide area detector allowing parallel data acquisition over a wide angular range. The analysis of the intensities measured by angle resolved XPS can provide information about the composition as a function of depth and, also, about the thicknesses of the different layers in a multilayer system. Another possibility to perform depth profiling is to use x-rays of different energies. According to Eq. (2.66), higher energy x-rays will release photoelectrons with higher kinetic energies, greater IMFP and, consequently, an increased sampling depth.

3 Investigated materials

Within the present thesis, ultrathin magnetite films as well as Fe_3O_4/NiO bilayers were deposited on single crystalline $SrTiO_3$(001) and MgO(001) substrates. Further, $NiFe_2O_4$ was synthesized by thermally induced interdiffusion starting with a distinct Fe_3O_4/NiO bilayer. In the following, the properties of the grown materials as well as the used substrates are briefly introduced.

3.1 Strontium titanate - substrate material

At room temperature, $SrTiO_3$ crystallizes in a cubic perovskite structure (cf. Fig. 3.1) with a lattice constant of $a_{SrTiO_3} = 3.905$ Å [68]. The lattice consists of Ti^{4+} ions sixfold coordinated by O^{2-} and of Sr^{2+} ions, which are coordinated by 12 O^{2-} ions. Thus, each Sr^{2+} ion is surrounded by eight TiO_6 octahedra. For any planar direction $[hkl]$ of a perovskite structure, always two distinct types of alternating equally spaced atomic planes (hkl) exist. In this study, $SrTiO_3$ substrates with a (001) surface orientation were used. In this case, the alternating atomic planes are SrO and TiO_2. The surface unit cell with axes pointing in [100] and [010] directions coincides with the cubic volume structure and, thus, exhibits the same lattice constant a_{SrTiO_3}. At lower temperatures (< 110 K) $SrTiO_3$ undergoes several structural phase transitions from cubic to lower symmetries.

Stoichiometric $SrTiO_3$ is an insulator with a band gap of about 3.2 eV and exhibits diamagnetic properties [69]. The magnetic properties and the electronic structure can be modified by the presence of oxygen vacancies or dopants. Especially, the magnitude of the conductivity strongly depends on the relative concentration of defects or dopants [70]. However, the conductivity can be more accurately controlled via doping than via oxygen deficiency. In this study, 0.05wt.% Nb-doped $SrTiO_3$ substrates were used to attain a diamagnetic and conductive support material (n-type conductivity).

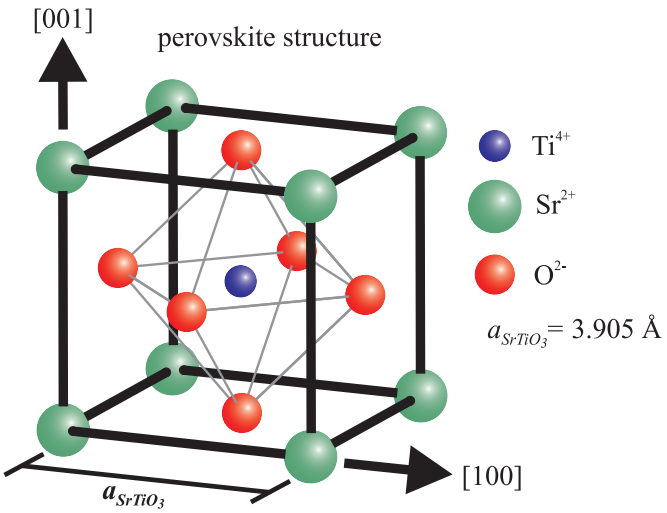

Fig. 3.1: Schematic sketch of a perovskite unit cell of cubic $SrTiO_3$. The bulk lattice constant at room temperature is denoted as a_{SrTiO_3}. The O^{2-} octahedron is marked in gray. The sizes of the spheres representing the atoms are arbitrary.

3.2 Magnesium oxide - substrate material

Magnesium oxide (MgO) crystallizes in a rock salt structure with a bulk lattice constant of $a_{MgO} = 4.2117\,\text{Å}$ at room temperature (see Fig. 3.2) [71]. Each of the ion types (Mg^{2+} and O^{2-}) forms a separate face-centered cubic lattice. These two lattices are shifted by half a unit cell against each other along one lattice vector. Thus, the Mg^{2+} are located at the octahedral sites of the fcc-lattice formed by O^{2-} ions and vise versa. In this study, MgO with a (001) surface orientation is used as substrate material. Here, a primitive surface unit cell can be defined in the (001) plane (cf. Fig. 3.2) with axes pointing in [110] and [$\bar{1}$10] directions forming a quadratic unit cell which is rotated by 45° compared to the bulk unit cell. The lattice constant of the surface unit cell is $a_{s,MgO} = a_{MgO}/\sqrt{2}$. Moreover, MgO is diamagnetic at room temperature and an electrical insulator with a band gap of about 7.8 eV [72].

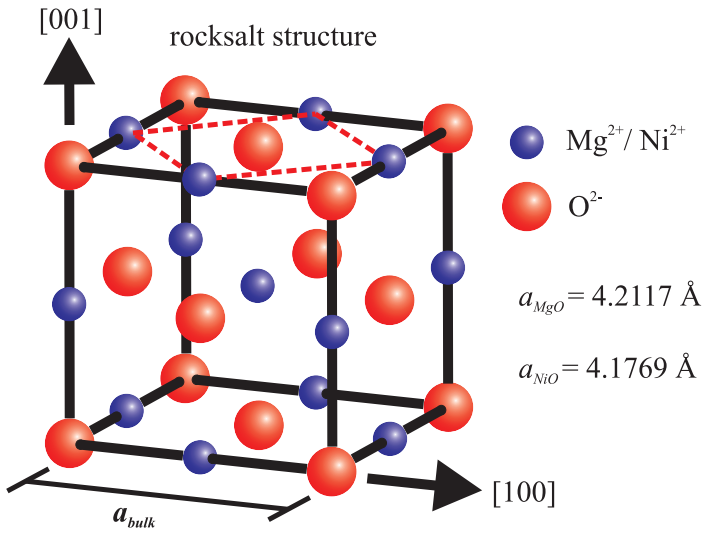

Fig. 3.2: Schematic sketch of a rock salt unit cell typical for MgO and NiO crystals. The red dotted line denotes the primitive surface unit cell in the (001) plane. The given lattice constants a_{MgO} and a_{NiO} are the bulk constants marked by a_{bulk} for MgO and NiO, respectively. The sizes of the spheres representing the atoms are arbitrary.

3.3 Nickel(II) oxide - NiO

Nickel(II) oxide (NiO) crystallizes in a rock salt structure with a lattice constant of $a_{NiO} = 4.1769\,\text{Å}$
for bulk material at room temperature (see Fig. 3.2) [73]. Analogously to MgO, the Ni^{2+} ions are located at the octahedral sites of the O^{2-} fcc-lattice. In the (001) plane, a primitive surface unit cell can be defined (cf. Fig. 3.2) with axes pointing in [110] and [$\bar{1}$10] directions. This surface unit cell exhibits a lattice constant of $a_{s,NiO} = a_{NiO}/\sqrt{2}$ and is rotated by 45° compared to the bulk unit cell. Further, NiO is electrically insulating with a band gap of about 4 eV [74] and antiferromagnetic with a Néel temperature of 525 K [75].

3.4 Magnetite - Fe_3O_4

Magnetite is an iron oxide with a chemical formula of Fe_3O_4 and contains divalent as well as trivalent iron cations. It crystallizes in the inverse spinel structure with a lattice constant of $a_{Fe_3O_4} = 8.3963\,\text{Å}$ for bulk material at room temperature [76]. The bulk unit cell consists of 56 atoms and is shown in Fig. 3.3. Here, 32 O^{2-} anions are arranged in a fcc-sublattice, whose tetrahedral and octahedral sites are filled to one eighth and one half by the Fe cations,

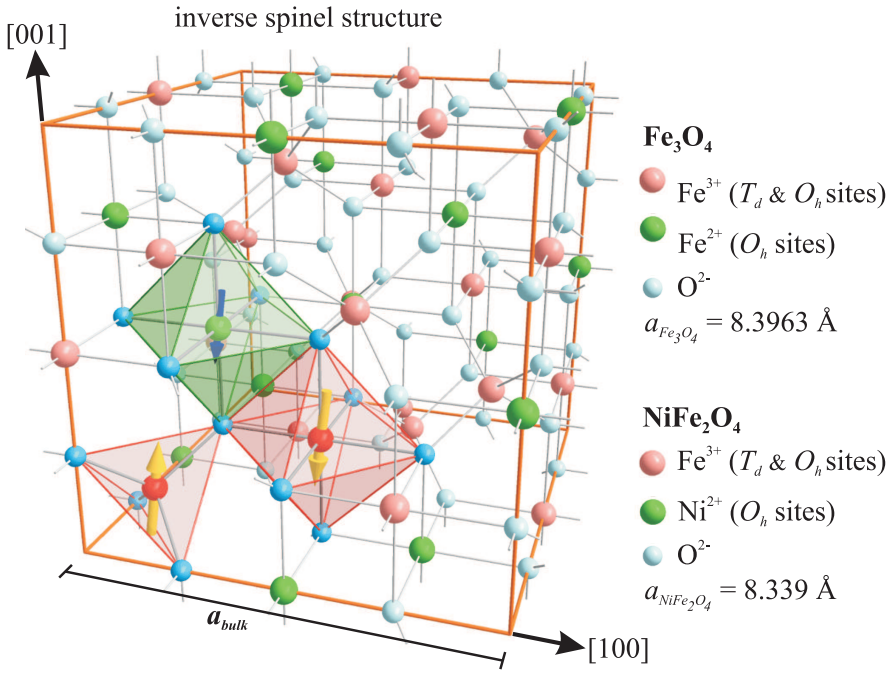

Fig. 3.3: Schematic sketch of the inverse spinel structure as it can be found for Fe_3O_4 and $NiFe_2O_4$. In magnetite, the Fe^{3+} cations are distributed equally across tetrahedral (T_d) and octahedral sites (O_h), while Fe^{2+} cations occupy only O_h sites. For nickel ferrite the Fe^{2+} cations are replaced by Ni^{2+}. As a result of the antiferromagnetic coupling between the magnetic moments of the Fe^{3+} cations located on T_d and O_h sites, only the magnetic moments of the Ni^{2+} in $NiFe_2O_4$ or Fe^{2+} in Fe_3O_4 account for the net macroscopic magnetization. The resulting magnetic moment per formula unit equals $2\mu_B$ and $4\mu_B$ for nickel ferrite and magnetite, respectively. The lattice constants $a_{Fe_3O_4}$ and $a_{NiFe_2O_4}$ are the bulk constants of the respective material marked by a_{bulk}. The sizes of the spheres representing the atoms are arbitrary. Adapted from Ref. [78].

respectively. Particularly, eight tetrahedral (T_d) sites are exclusively occupied by Fe^{3+} while 16 octahedral (O_h) sites are equally shared by randomly distributed Fe^{3+} and Fe^{2+} ions. In contrast, in a normal spinel structure all divalent cations occupy exclusively tetrahedral (T_d) sites, while all trivalent cations are located solely at octahedral sites (O_h). In the (001) plane of the Fe_3O_4 bulk unit cell, also, a primitive surface unit cell with a lattice constant of $a_{s,Fe_3O_4} = a_{Fe_3O_4}/\sqrt{2}$ can be defined. The axes of the surface unit cell point in [110] and [$\bar{1}$10] directions leading to a 45° rotation compared to the bulk unit cell of magnetite. Further, the Fe_3O_4(001) surface exhibits a $(\sqrt{2} \times \sqrt{2})$R45° reconstruction with respect to the surface unit cell, which is typical for well-ordered stoichiometric magnetite [77].

Moreover, Fe_3O_4 is a ferrimagnet with a high Curie temperature of $T_C = 858$°C [76]. As in most spinel ferrites, the ferrimagnetic ordering arises from the strong antiferromagnetic coupling between the O_h and T_d sites. Consequently, the magnetic moments of the Fe^{2+} ions on octahedral sites are uncompensated leading to a net magnetic moment of about $4\mu_B$ [79]. Further, magnetite is a half-metal with a predicted total negative spin polarization at the Fermi level [11] and a bad conductor at room temperature. At about 120 K magnetite undergoes a metal to insulator transition (Verwey transition) leading to a two-orders-of-magnitude decrease in conductivity and accompanied by a reduction from cubic to monoclinic crystal symmetry [80, 81]. This transition is highly sensitive to structural parameters such as induced strain, domain size and, thus, film thickness [82, 83].

3.5 Nickel ferrite - $NiFe_2O_4$

$NiFe_2O_4$ crystallizes in the inverse spinel structure with a bulk lattice constant of $a_{NiFe_2O_4} = 8.339\,\text{Å}$ at room temperature [84]. The unit cell of nickel ferrite consists of 56 atoms including 32 O^{2-} anions, 16 Fe^{3+} and eight Ni^{2+} cations. In contrast to magnetite, there is no iron in the divalent oxidation state. Thus, the 16 Fe^3+ cations are equally distributed across the tetrahedral (T_d) and octahedral (O_h) sites, while the Ni^2+ cations are located solely on octahedral (O_h) sites. More detailed description of the (inverse) spinel structure can be found in Sec. 3.4.

Further, bulk $NiFe_2O_4$ is a ferrimagnet with a Curie temperature of $T_C = 865°C$. An antiferromagnetic coupling between the magnetic moments of the Fe^{3+} cations located on T_d and O_h sites leads to a compensation of the magnetic contribution of the iron ions. Thus, only the magnetic moments of the Ni^{2+} cations account for the net macroscopic magnetization of about $2\mu_B$/f.u. Moreover, $NiFe_2O_4$ is an insulator with a band gap of about 1.5 eV [12]. Due to the combination of insulating and ferrimagnetic properties, there is an exchange splitting (spin-split) of the conduction band, which can lead to a spin-selective transport of electrons [13].

3.6 Antiphase boundaries in Fe_3O_4 and $NiFe_2O_4$

Antiphase domains exhibit the same crystallographic orientation and chemical composition but are shifted by a fraction of a lattice translation against each other (cf. Fig. 3.4). If two of these single crystalline regions coalesce, the so-called antiphase boundaries (APBs) are formed at their interface. Antiphase domains and boundaries emerge during the ordering or growth process, which can start at different locations in the disordered lattice or at different nucleation centers on the substrate, respectively, resulting in a smaller distance between two domains than the size of a unit cell. Especially in magnetite or nickel ferrite films, APBs frequently occur due to the doubled size of their lattice constants compared to the used MgO and $SrTiO_3$ substrates [85–89]. In several detailed studies, it was shown that the density of APBs in magnetite depends on the deposition conditions, e.g., temperature and rate, and can significantly affect its magnetic and electrical properties [88]. For example, the magnetization in thin ferro(i)magnetic films can be reduced or extremely high magnetic fields are required to reach saturation magnetization [90,91]. Further, in thin magnetite films the Verwey transition broadens and is eventually completely suppressed with decreasing film thickness [85,88]. The reduction of the density of APBs can be achieved by post-deposition annealing or by using higher deposition rates which lead to higher mobility of the adsorbed ions on the surface.

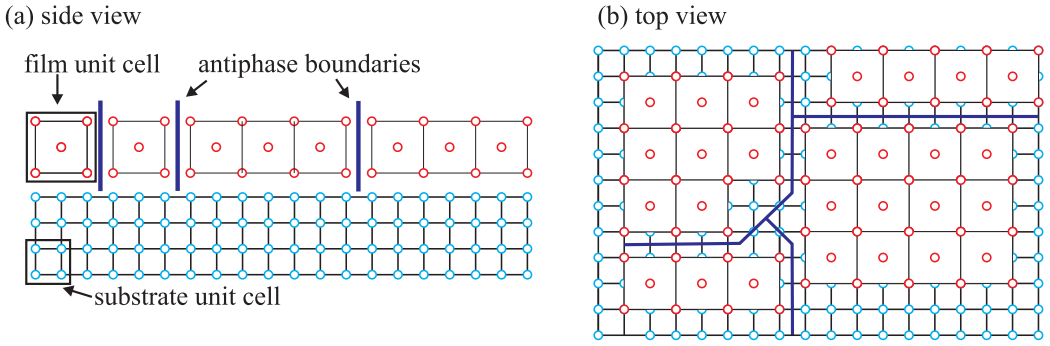

Fig. 3.4: (a) Side view and (b) top view of a thin film grown on a substrate showing antiphase boundaries (APBs). Adapted from Ref. [92].

4 Experimental setup

4.1 UHV system and sample preparation

Most of the samples investigated in this thesis were prepared in an interconnected UHV system at Osnabrück University. It comprises a deposition chamber with a base pressure of 10^{-8} mbar and an analysis chamber with a base pressure of 10^{-10} mbar. Further, the system is equipped with a load-lock chamber and a transfer system, which enables the transfer to the deposition chamber and to the analysis chamber. The deposition chamber is equipped with a rotary manipulator, several thermal evaporation sources, a heating device and an O_2 valve to adjust the oxygen pressure during annealing or evaporation. The sample heating is realized using a filament at the backside of the sample holder. The temperature of the sample is measured by a thermocouple mounted at the manipulator close to the sample position. The analysis chamber comprises a 4-grid LEED optics (ErLEED 150, SPECS, Berlin) and an XPS system with Al Kα and Mg Kα radiation sources and a hemispherical analyzer (Phoibos HSA 150 Specs, Berlin).

Thin films are grown by molecular beam epitaxy (MBE), which is a physical vapor deposition method (PVD). For MBE, a constant flow of atoms or molecules is produced and directed towards the substrate surface. For this purpose, effusion cells are used enabling thermal evaporation from a pure metal rod or from material placed in a crucible. The design of an evaporator is schematically shown in Fig. 4.1. All films prepared within this thesis were deposited directly from pure metal rods without using any crucible. High voltage is applied between the metal rod and the filament in order to accelerate the electrons emitted from the filament towards the metal. Once the sublimation temperature of the material (in our case Fe or Ni) is reached, the evaporation starts. Due to the aperture of the evaporator, a molecular beam is formed pointing towards the substrate. Additionally, the evaporator is equipped with a water cooling system and a shutter, which allows to start or stop the deposition immediately at a certain point in time. The amount of evaporated material is controlled by monitoring the material flow using either a quartz crystal microbalance or a flux monitor. Deposition rates are adjusted by measuring the deposited film thickness via XRR. The used material combination as well as the deposition conditions, e.g., temperature, oxygen pressure, deposition rate etc., have to be precisely defined,

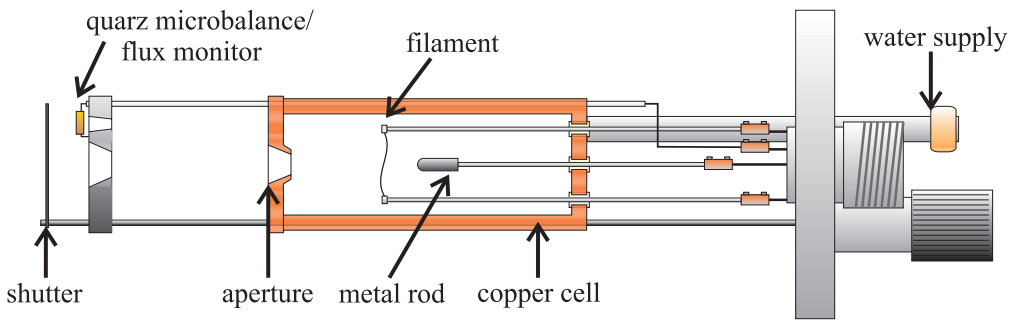

Fig. 4.1: Schematic sketch of an evaporator equipped with a pure metal rod. Adapted from Ref. [93].

in order to obtain homogeneous growth of high quality thin films with correct crystallographic orientation and in the desired phase.

High quality MgO and 0.05% Nb-doped $SrTiO_3$ substrates with a (001)-surface orientation were provided by the CrysTec GmbH. After the transfer to the UHV-chamber the substrates were annealed at 400°C in 1×10^{-4} mbar of O_2 for 1 h in order to remove carbon contaminations and get well-ordered surfaces. Thereafter, the chemical cleanness and the crystal surface quality were controlled *in situ* by XPS and LEED, respectively. Here, the benchmark for a clean surface was the absence of the C 1*s* peak and other impurities in the XPS spectrum and a well-defined diffraction pattern with sharp spots and a low background intensity in the LEED measurement. The thin Fe_3O_4 and NiO films were grown by deposition of metals in 5×10^{-6} mbar and 1×10^{-5} mbar oxygen atmosphere, respectively. The deposition rate and the substrate temperature of 250°C were kept constant during the deposition. After evaporation, XPS and LEED measurements were again performed to control the stoichiometry and the surface structure, respectively.

4.2 Experimental setups at synchrotron radiation facilities

All (GI)XRD (GI: grazing incidence) and HAXPES experiments presented in this work were carried out at different synchrotron radiation facilities, namely, the ESRF in Grenoble (France), Diamond in Didcot (England), PETRA III at DESY in Hamburg (Germany) or MaXLab in Lund (Sweden). Compared to laboratory based x-ray sources, synchrotron light comprises a number of advantages including a higher intensity, tunable energy as well as a smaller divergence and beam size. All these features ensure the performance of high resolution measurements in several geometries and are therefore a powerful tool for the investigation of thin film systems.

4.2.1 Generation of synchrotron radiation

The basic principle behind the generation of synchrotron light is the emission of electromagnetic radiation originating from charged particles (electrons or positrons) during acceleration. In case these particles move at a non-relativistic velocity, a dipole radiation pattern is emitted which has a toroidal shape with its main axis pointing into the direction of the accelerating force [cf. Fig. 4.2(a)]. However, for particles traveling almost at the speed of light relativistic effects and

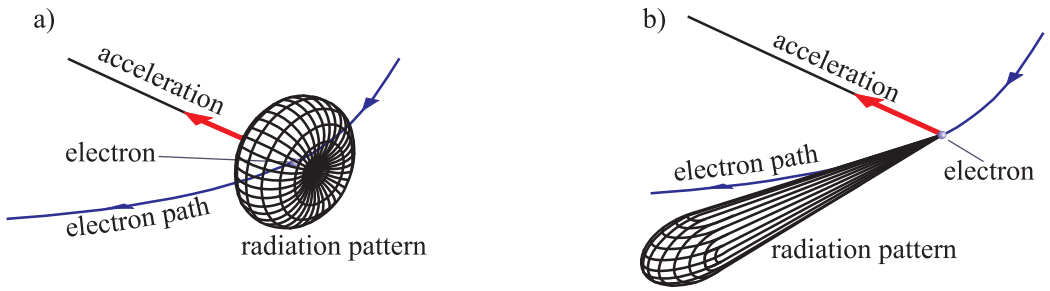

Fig. 4.2: Emission of radiation of an electron, which is accelerated along an orbital path and travels (a) at a non-relativistic velocity and (b) almost at the speed of light. Adapted from Ref. [94].

the Doppler shift have to be considered. In this case, the emitted electromagnetic radiation is concentrated into a cone which center is pointing into the tangential direction of the electrons' trajectory [cf. Fig. 4.2(b)].

Today, the most common radiation sources are the so-called third-generation storage rings. Here, electrons/positrons are traveling at constant velocities close to the speed of light. Typically, these storage rings have a polygon like shape consisting of straight and curved sections in alternating order. In each curved section, two large bending magnets force bunches of electrons/positrons into their orbit. Whenever these bunches are deflected from straight line motion and, thus, transversely accelerated, synchrotron radiation is generated. The synchrotron light from a bending magnet covers a wide and continuous spectrum ranging from microwaves to hard x-rays. The emission spectrum depends on the bending radius and the energy of the particles, and is mainly defined by the geometry of the storage ring.

To increase the intensity or brilliance of the emitted beam, so-called insertion devices are integrated in the straight sections of the storage ring. This periodic arrangement of dipole magnets with alternating polarity forces the charged particles to follow a wavy or undulating trajectory. Depending on the strength of the magnetic field and the displacement of the particles from their straight path, the device is called wiggler or undulator.

In case of a wiggler, the large displacement of the electrons/positrons leads to an incoherent superposition of the radiation cones emitted during each oscillation period. The resulting emission spectrum is continuous and similar to that of a bending magnet but exhibits a higher intensity. An advantage over a bending magnet is that the magnetic arrangement of a wiggler is not affected by the storage ring geometry and can be fitted to the experimental requirements. In contrast, the magnetic structure of an undulator allows only small amplitudes of the oscillations leading to interference of the radiation cones of each consecutive bend. The coherent superposition results in a sharp emission line at a certain energy and its repetition at corresponding higher harmonics. The wavelength of the generated x-rays can be fine-tuned by varying the gap between the rows of magnets and, thus, changing the arrangement of the magnetic field.

After passing the insertion device the beam properties are adjusted using different monochromator crystals, focusing lenses, windows and slits. The actual setups for scattering experiments or photoelectron spectroscopy are located at the beamline endstations.

The measurements presented within this thesis were performed at five different beamlines. The XRD experiments shown in Chap. 5 were carried out at beamline BM25 (ESRF, Grenoble), which is located at a bending-magnet device covering the hard x-ray energy range. The XRD spectra shown in Chap. 6 were recorded at beamline I811 (MaXLab, Lund) which is equipped with a superconducting multipole wiggler. The HAXPES and XRD measurements in Chap. 7 were performed at beamlines I09 (Diamond, Didcot) and P08 (PETRA III, Hamburg), respectively. At both beamlines, an undulator is used as insertion device. Further, x-ray magnetic circular dichroism (XMCD) experiments (Chap. 7) were carried out at beamline 6.3.1 (ALS, Berkley), which is a bending-magnet beamline. Further information on generation and properties of synchrotron radiation and the mentioned devices can be found in Refs. [95, 96].

4.2.2 HAXPES - experimental setup

In addition to XPS, HAXPES provides information on the electronic structure also in deeper layers. The experiments were carried out at beamline I09 (Diamond, Didcot) using a photon energy of $h\nu = 5934\,\mathrm{eV}$. The geometry of the experimental layout is schematically sketched in Fig. 4.3. The incidence angle $\theta = 25°$ of the x-ray beam with respect to the plane surface is kept constant during all measurements. The variation of the probing depth and, thus, the bulk sensitivity, is achieved using a 2D wide-area photoelectron detector. Hence, parallel data acquisition over a angular range of 56° is possible and allows to record photoelectron spectra for different emission angles simultaneously. In our case, the detector is divided in seven sections,

each covering ∼7° of the acceptance angle leaving out the regions near the edges of the detector.

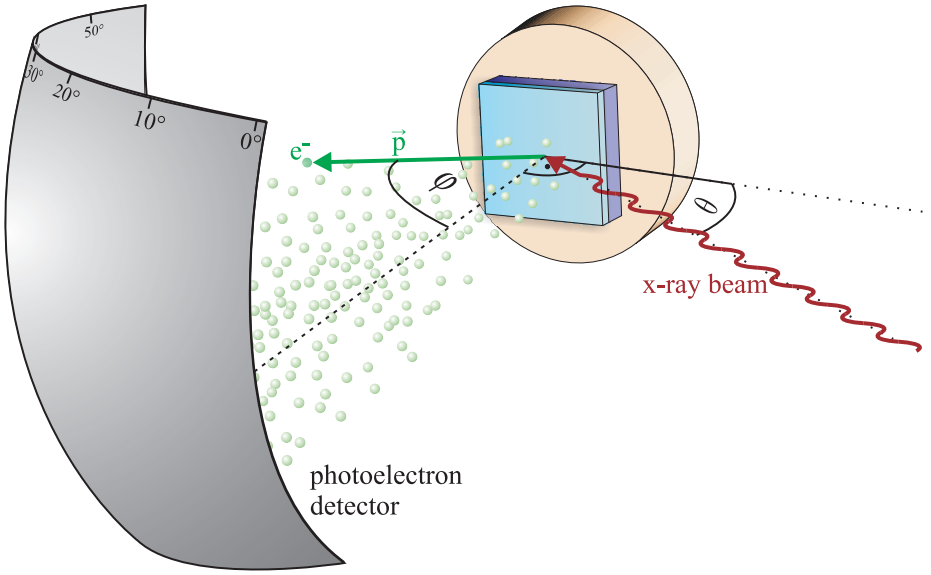

Fig. 4.3: Schematic sketch of the experimental setup at the beamline I09 used for depth dependent HAXPES measurements. The 2D wide-area detector covers an angular range of 56° allowing data collection for different emission angles φ simultaneously. $\vec{p}$ denotes the momentum of the electron leaving the sample surface at a particular angle φ. The incidence angle θ of the x-ray beam is kept constant during all measurements. Taken from [97].

The angular dependence of information depth D_I, from which 95% of the photoelectrons originate, is given by

$$D_I(95) = -\lambda \cos\varphi \ln(1 - 95/100) \quad , \tag{4.1}$$

with the inelastic mean free path λ and the off-normal emission angle φ [98]. The maximum information depth, e.g., for the Fe $2p$ or Ni $2p$ core levels amounts to $\sim 20\,\text{nm}$ at the used energy.

4.2.3 (GI)XRD - experimental setup

The main part of an x-ray scattering experiment is a diffractometer for sample and detector positioning. In Fig. 4.4, a sketch of a 2S+3D diffractometer is shown exemplarily. This type of diffractometer is available at beamlines I811 and BM25, where the measurements shown in Chaps. 5 and 6 were performed. It has two degrees of freedom for sample alignment and three degrees of freedom for detector positioning. Further, it can be used in two different geometries: vertical and horizontal mode. The endstation of the P08 beamline is equipped with a high precision 6-circle diffractometer with an Eulerian cradle (KOHZU NZD-3). The design of the diffractometer was developed according to the requirements of PETRA III. It provides four degrees of freedom for sample alignment and two degrees of freedom for detector positioning, which is denoted as 4S+2D, offering several different scattering geometries. Detailed information can be found in Ref. [100].

For the measurements presented in this thesis, two different scattering geometries were used, one for the specular and one the grazing incidence scattering. For the specular x-ray diffraction and reflectivity, the so-called four-circle mode in the horizontal geometry is utilized (cf. Fig. 4.4). In

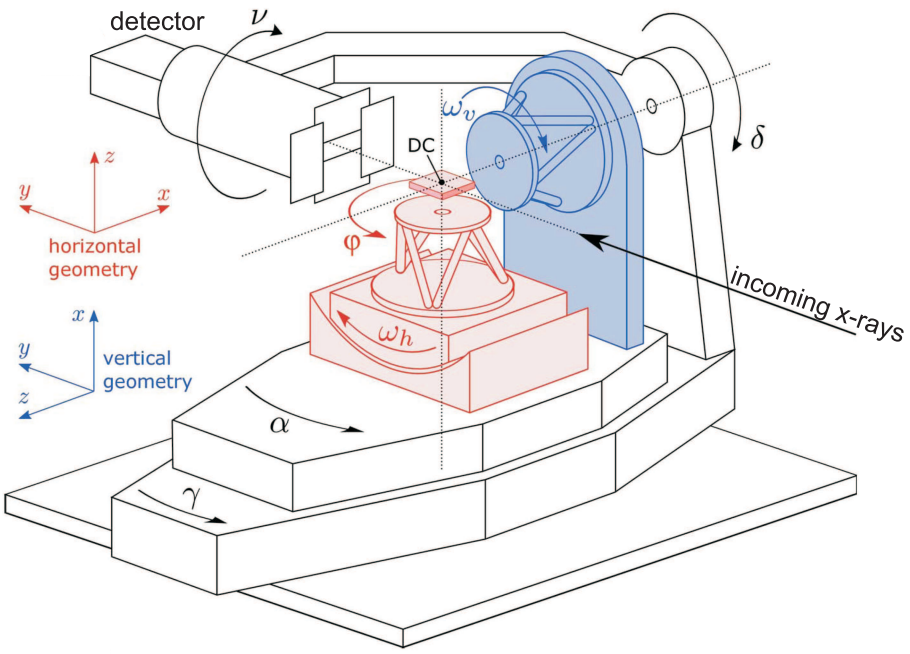

Fig. 4.4: Sketch of the 2S+3D diffractometer used at the beamlines I811 and BM25. The rotation axes as well as the two different geometry modes are denoted. The detector position is defined by the angles δ and γ, while θ provides a rotation of the detector. In the vertical geometry, ω_v and α provide the azimuthal and polar degrees of freedom, respectively. In the horizontal mode, the azimuthal and polar degrees of freedom are given by ω_h and φ. The diffractometer center (DC) is intersected by all rotation axes. Adapted from Ref. [99].

this setup, the lateral components of the scattering vector are zero. Further, the wave vectors from the incident and the exiting beam have to be in the plane which is perpendicular to the sample surface. For this purpose, the angles α and γ are fixed to zero. The incidence angle is defined by ω_h, while the diffraction angle is given by δ. If the sample is tilted by an angle $\omega_h = \theta$, the detector has to be rotated by $\delta = 2\theta$ to fulfill the scattering condition. Therefore, this geometry is known as $\theta - 2\theta$ measurement.

Typically, GIXRD is performed in the vertical geometry (cf. Fig. 4.4). Here, a fixed angle of incidence is necessary, which is now defined as α. For diffraction, this angle should be slightly larger than the critical angle of the investigated material (cf. Sec. 2.5). Typical values for α are $0.3° - 0.5°$ for the materials and energies used within this work. In this geometry, ω_v is used to rotate the sample about its surface normal to access the complete reciprocal space. The detector position is adjusted by the angles δ and γ in order to fulfill the diffraction condition. GIXRD allows to measure intensities near the $L = 0$ plane of the reciprocal space (in-plane Bragg peaks) as well as non-specular CTRs.

4.2.4 Analysis and correction of x-ray diffraction data

Prior to analysis of the CTRs, the measured intensity has to be corrected by several factors. Table 4.1 gives an overview of the corrections used in this thesis for the grazing incidence and specular diffraction geometry with vertical and horizontal alignment of the sample surface, respectively. Here, only non-constant contributions, which show angular dependences during the measurements, are considered. A more detailed description of possible correction factors can be

	Specular diffraction	Grazing incidence diffraction
Polarization factor P	1	$1-(\sin\alpha\cos\delta\cos\gamma+\cos\alpha\sin\gamma)^2$
Lorentz factor L	$1/\sin\omega$	$1/\sin\gamma$
Active area A	$1/\sin\omega$	$1/\sin\delta$

Tab. 4.1: Correction factors for the diffracted intensity measured in specular geometry with horizontal sample surface and in grazing incidence geometry with vertical sample surface.

found in literature [28, 101].

The Lorentz factor L gives the geometrical correction with respect to the integration volume, which has to be considered during the conversion from real to reciprocal space. The active area factor A describes the intersection of the illuminated sample area and the area visible to the detector. This area is usually determined by the alignment of the slits and the detector position. However, in our case only the detector position is relevant, since the slits are fixed during the measurement. Further, the scattered intensity is reduced due to the polarization of the x-ray beam by $\cos^2\alpha_{pol}$. Here, α_{pol} is the angle between the direction of the polarization of the incident beam and the wave vector of the scattered photon. The polarization correction P given in Tab. 4.1 is obtained, taking into account that the x-rays produced by an insertion device are 99% (or better) polarized within the deflection plane (usually horizontal polarization).

Consequently, the total corrected intensity I_{cor} is given by

$$I_{cor} = \frac{I_m}{P\,L\,A} \quad , \tag{4.2}$$

where P, L, A are the factors given in Tab. 4.1 and I_m the measured intensity.

For deeper analysis of the corrected data, the fitting program RodsNPlots has been used. This program allows to calculate the diffracted intensity along CTRs measured in specular diffraction as well as in grazing incidence diffraction geometry with high accuracy. It was developed by A. Greuling [102] and improved by S. Hahne and F. Bertram [103, 104]. The calculation of the diffracted intensity is based on Eq. (2.48) developed in Sec. 2.4.

For the calculation, a user-defined model is necessary, which consists of a variable number of crystalline layers on a substrate. These layers are described by several parameters. For each layer, the number of unit cells and a material parameter are chosen. The latter contains the information on the structure factor and the vertical layer distance. Further fitting parameters are the occupation factor, scaling factors of the vertical lattice vector and the interface vector (solely vertical components), adsorption site, top and bottom RMS roughnesses and the Debye-Waller factor. Different numerical optimization algorithms, which operate in user-specified limits, are implemented with the aim to describe the experimental data by the model in the best possible way. For the analysis of the data shown in this thesis, the differential evolution algorithm has been employed. Additionally, the underlying model can contain several lateral coexisting columns each consisting of multiple layers to describe laterally coexistent structural phases. However, there was no need to use this option during the data analysis within this thesis.

Though RodsNPlots is a powerful tool for the analysis of the diffracted intensity from thin film systems, one has to keep in mind some limitations. First, the used theoretical model does not

consider any lateral misfit. The second limitation is that reasonable results are only available for an integer number of atomic unit cells. Hence, it is not possible to fit this parameter, so it has to be chosen by the user in advance. Third, the structure factor is not considered in the roughness model. This fact leads to unrealistic results for the diffracted intensity in the regions near forbidden Bragg peaks. To avoid this problem, the unit cell used for the calculation of the structure factor has to be chosen as small as possible.

More detailed information concerning RodsNPlots, the used parameters and the different optimization algorithms can be found in literature [28].

Original publication: Applied Physics Letters **111**, 041902 (2017)
available at http://dx.doi.org/10.1063/1.4995408

Real-time monitoring of the structure of ultrathin Fe_3O_4 films during growth on Nb-doped $SrTiO_3(001)$

O. Kuschel, W. Spiess, T. Schemme, J. Rubio-Zuazo, K. Kuepper, and J. Wollschläger

Abstract

In this work, thin magnetite films were deposited on $SrTiO_3$ via reactive molecular beam epitaxy at different substrate temperatures. The growth process was monitored *in situ* during deposition by means of x-ray diffraction. While the magnetite film grown at 400°C shows a fully relaxed vertical lattice constant already in the early growth stages, the film deposited at 270°C exhibits a strong vertical compressive strain and relaxes towards the bulk value with increasing film thickness. Furthermore, a lateral tensile strain was observed under these growth conditions although the inverse behavior is expected due to the lattice mismatch of -7.5%. Additionally, the occupancy of the A and B sublattices of magnetite with tetrahedral and octahedral sites was investigated showing a lower occupancy of the A sites compared to an ideal inverse spinel structure. The occupation of A sites decreases for a higher growth temperature. Thus, we assume a relocation of the iron ions from tetrahedral sites to octahedral vacancies forming a deficient rock salt lattice.

Original publication: Materials **11**, 1122 (2018)
available at http://dx.doi.org/10.3390/ma11071122

Impact of strain and morphology on magnetic properties of Fe_3O_4/NiO bilayers grown on Nb:$SrTiO_3$(001) and MgO(001)

O. Kuschel, N. Pathé, T. Schemme, K. Ruwisch, J. Rodewald, R. Buß, F. Bertram, T. Kuschel, K. Kuepper and J. Wollschläger

Abstract

We present a comparative study of the morphology and structural as well as magnetic properties of crystalline Fe_3O_4/NiO bilayers grown on both MgO(001) and $SrTiO_3$(001) substrates by reactive molecular beam epitaxy. These structures were investigated by means of x-ray photoelectron spectroscopy, low-energy electron diffraction, x-ray reflectivity and diffraction, as well as vibrating sample magnetometry. While the lattice mismatch of NiO grown on MgO(001) was only 0.8%, it was exposed to a lateral lattice mismatch of −6.9% if grown on $SrTiO_3$. In the case of Fe_3O_4, the misfit strain on MgO(001) and $SrTiO_3$(001) amounted to 0.3% and −7.5%, respectively. To clarify the relaxation process of the bilayer system, the film thicknesses of the magnetite and nickel oxide films were varied between 5 and 20 nm. While NiO films were well ordered on both substrates, Fe_3O_4 films grown on NiO/$SrTiO_3$ exhibited a higher surface roughness as well as lower structural ordering compared to films grown on NiO/MgO. Further, NiO films grew pseudomorphic in the investigated thickness range on MgO substrates without any indication of relaxation, whereas on $SrTiO_3$ the NiO films showed strong strain relaxation. Fe_3O_4 films also exhibited strong relaxation, even for films of 5 nm thickness on both NiO/MgO and NiO/$SrTiO_3$. The magnetite layers on both substrates showed a fourfold magnetic in-plane anisotropy with magnetic easy axes pointing in ⟨100⟩ directions. The coercive field was strongly enhanced for magnetite grown on NiO/$SrTiO_3$ due to the higher density of structural defects, compared to magnetite grown on NiO/MgO.

6.1 Introduction

Transition metal oxides are one of the most interesting material classes, providing a huge variety of structural, magnetic, and electronic properties ranging from metallic to insulating, from ferro- to antiferromagnetic, as well as ferroelectric states [127]. Especially, thin magnetite films (Fe_3O_4) have attracted intensive research interest in the last decade in the field of spintronics [105] and spin caloritronics [106, 108]. Due to their anticipated half-metallic behavior with complete spin polarization at the Fermi level [11] and high (bulk) Curie temperature of 858 K [76], thin magnetite films are promising candidates for room temperature spintronic devices such as highly spin-polarized electrodes for magnetic tunneling junctions [109, 110, 128] or spin injectors [111]. Furthermore, multilayers of magnetite and platinum show huge thermoelectric effects [112] based on the recently observed spin Seebeck effect in magnetite [113] pushing the development of more efficient thermoelectric nanodevices [114].

Magnetite crystallizes in the inverse spinel structure with a lattice constant of 8.3963 Å [76] at 300 K. At ∼120 K it undergoes a metal-insulator transition (Verwey transition) [80] accompanied by a change from cubic to monoclinic crystal symmetry [81]. The reduction of the crystal symmetry leads to a spontaneous ferroelectric polarization and, thus, to multiferroicity [115,116].

In order to control the relative magnetization alignment in magnetic tunnel junctions, exchange bias effects induced by additional antiferromagnetic layers are commonly used [19]. In the case of Fe_3O_4 tunnel junctions, the antiferromagnetic NiO is a good candidate due to its small lattice mismatch of only 0.5% and a high Néel temperature of 523 K [75].

Nickel oxide is an insulating material with a high thermal stability. It crystallizes in a rock salt structure with a lattice constant of 4.1769 Å [73] at 300 K. It was recently shown that NiO can act as a spin-current amplifier in spin Seebeck experiments, and can additionally be a spin-current generator when a thermal gradient is applied [21–24], making NiO a key material for thermoelectric devices. Further, the latest studies report on a temperature-dependent sign change in the spin Hall magnetoresistance for nickel oxide on ferromagnetic insulator [129, 130]. Thus, there is a possibility to use it as a spin filter.

Previous works [18,50,121,131–134] have focused on the characterization of magnetite and nickel oxide films grown on MgO substrates because of the small lattice mismatch of 0.3% and 0.8%, respectively. However, it has been demonstrated that the electronic and magnetic properties of magnetite films can be modified using $SrTiO_3$ substrates [83, 135, 136], despite the large lattice mismatch of −7.5%. One advantage of using $SrTiO_3$ substrates is the possibility of doping and, thus, a tunable conductivity providing either an insulating or metallic substrate which can be used as a bottom electrode in capacitor-like structures [116]. Furthermore, Fe_3O_4/NiO bilayers grown on $SrTiO_3$ can be used to synthesize $Ni_xFe_{3-x}O_4$ thin films by thermally induced interdiffusion with tunable magnetic and electric properties [25].

To date, most studies concerning NiO films on $SrTiO_3$ have been limited to a coarse analysis of the growth [137, 138], while a thorough structural characterization is seldom reported [139]. In the case of Fe_3O_4/NiO bilayers on both substrates, there are a number of works on electronic structure, interfacial coupling, and magnetic characterization [140–143], whereas to the best of our knowledge there are no detailed structural studies for these bilayers on $SrTiO_3$. However, the magnetic and transport characteristics of such films are sensitive to structural variations, number of defects, or stoichiometric deviations, and can be affected by the strain between film and substrate [83]. Therefore, in this work, a comprehensive structural characterization of Fe_3O_4/NiO bilayers of different thicknesses grown on Nb-doped $SrTiO_3$(001) and for comparison on MgO(001) is presented. Additionally, these results are correlated with magnetic properties (e.g., magnetocrystalline anisotropy).

Directly after deposition, the stoichiometry in the near-surface region and the surface structure of each layer was determined *in situ* using x-ray photoelectron spectroscopy (XPS) and low-energy electron diffraction (LEED), respectively. The bulk structure was investigated *ex situ* by x-ray reflectivity (XRR) and synchrotron radiation x-ray diffraction (SR-XRD) measurements and analyzed within kinematic diffraction theory. Further, angle-dependent hysteresis loops were measured via vibrating sample magnetometry (VSM).

6.2 Materials and methods

Preparation and *in situ* characterization of the thin oxide films were carried out in an interconnected ultra-high vacuum (UHV) system at a base pressure of 10^{-8} mbar in the deposition chamber and 10^{-10} mbar in the analysis chamber. Epitaxial Fe_3O_4/NiO ultrathin bilayer sys-

tems with thicknesses between 5 nm and 20 nm were grown via reactive molecular beam epitaxy (RMBE) on 0.05% Nb-doped $SrTiO_3(001)$ or on MgO(001) single crystalline substrates. Prior to deposition, the substrates were annealed at 400°C in 1×10^{-4} mbar O_2 atmosphere for 1 h in order to remove carbon contamination and get well-defined surfaces. Subsequently, nickel oxide and magnetite films were deposited by thermal evaporation from pure metal rods in 1×10^{-5} mbar and 5×10^{-6} mbar oxygen atmosphere, respectively. Deposition was performed at 250°C substrate temperature using deposition rates of 0.01 nm/s for nickel oxide films and 0.025 nm/s for magnetite films, as controlled by a quartz microbalance adjacent to the evaporation source. The resulting film thicknesses were determined later on *ex situ* by XRR (Panalytical, Philips X'Pert Pro, Almelo, The Netherlands). Crystal surface quality and near-surface stoichiometry were controlled *in situ* after each preparation step by LEED (ErLEED 150, SPECS, Berlin, Germany) and XPS (SPECS, Berlin, Germany) using an Al Kα ($h\nu$ = 1486.6 eV) radiation source and a Phoibos HSA 150 hemispherical analyzer.

After transport under ambient conditions, XRR and XRD experiments were carried out *ex situ* for structural characterization of the films. XRR measurements were performed in $\theta - 2\theta$ geometry using a lab based diffractometer equipped with a Cu Kα anode. An in-house developed fitting tool based on the Parratt algorithm [51] using Névot-Croce [54] roughness profiles was applied for the analysis of the XRR curves. For XRD synchrotron based radiation sources at the MaXLab beamline I811 (MaXLab, Lund, Sweden) and at the Swiss Light Source beamline X04SA (Paul Scherrer Institute, Villigen, Switzerland) were used. Both beamlines are equipped with (2S+3D) type diffractometers and Pilatus pixel area detectors for data collection. The XRD data were recorded in $\theta-2\theta$ geometry at an energy of 12.4 keV and analyzed within the kinematic diffraction theory [95] that is implemented in our in-house developed fitting tool.

In addition, magnetization curves were measured at room temperature for several in-plane directions of the samples by varying the magnetic field $\mu_0 H$ between −300 mT and +300 mT, using a VSM (Lakeshore, Model 7407, Westerville, OH, USA). The magnetization loops were corrected by subtracting the diamagnetic contribution from the substrates.

6.3 Results

6.3.1 LEED / XPS

Figures 6.1(a),(d) present the LEED patterns of the cleaned MgO(001) and $SrTiO_3(001)$ surfaces, respectively. All as-prepared NiO and Fe_3O_4 films showed similar LEED patterns on the respective substrate for all investigated thicknesses ranging from 5 nm to 20 nm. Thus, only patterns of a ∼20 nm Fe_3O_4 and a ∼10 nm NiO film on MgO and $SrTiO_3$ are shown as examples in Fig. 6.1. The intensity variations in all recorded patterns were due to dynamical scattering for electron diffraction, and will not be considered further. Instead, we focus on the symmetry of the diffracted pattern and the sharpness of the diffraction spots. Clear (1×1) structures corresponding to the square unit cells of MgO(001) and $SrTiO_3(001)$ surfaces could be seen [see Fig. 6.1(a),(d)]. Due to the rock salt structure of MgO, the reciprocal unit vectors of the MgO(001) surface point in [110] and [$\bar{1}$10] directions, forming a quadratic reciprocal unit cell. The reciprocal unit vectors of the (001) surface of the perovskite $SrTiO_3$ point in [100] and [010] directions, also forming a quadratic unit cell. Consequently, the reciprocal surface unit vectors of MgO(001) are $\sim\sqrt{2}$ times larger than those of $SrTiO_3(001)$.

In diffraction patterns, a random arrangement of point defects leads to an increased background, while line defects (e.g., domain boundaries) result in a broadening of the diffraction spots [55]. To obtain not only qualitative but also quantitative information on the defect density, the full

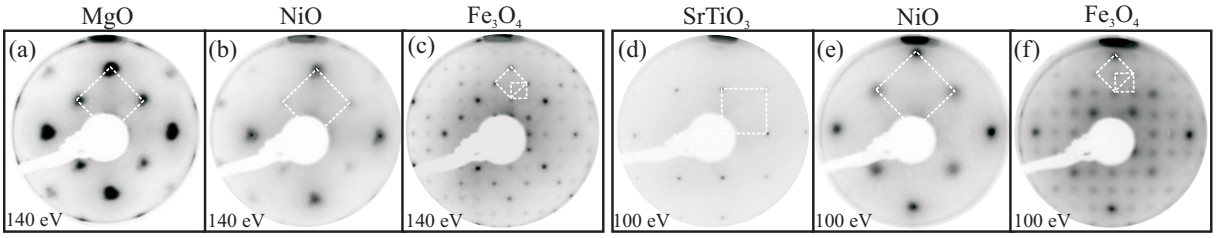

Fig. 6.1: Low-energy electron diffraction (LEED) pattern recorded at 140 eV for (a) pure MgO(001) surface; (b) 11.9 nm NiO film on MgO(001); and (c) 21.5 nm Fe_3O_4 on NiO/MgO(001). The LEED pattern taken at 100 eV of a pure $SrTiO_3$ surface, a 10.4 nm NiO film on $SrTiO_3$(001), and 20.7 nm Fe_3O_4 on NiO/$SrTiO_3$(001) are depicted in (d–f), respectively. The larger white squares indicate the (1×1) structure of the reciprocal unit cell of the respective surfaces, while the smaller white squares in (c) and (f) indicate the $(\sqrt{2} \times \sqrt{2})$R45° superstructure unit cell of magnetite.

width of half maximum (FWHM) of the diffraction spots was determined at 140 eV, taking into account the instrumental broadening of the LEED instrument.

The $SrTiO_3$ pattern exhibited sharp and intense diffraction spots. Analysis of the FWHM of the (11) diffraction peaks yielded a line defect density of $(0.11 \pm 0.02)\,\mathrm{nm}^{-2}$. In contrast, the spots of the MgO substrate were broadened due to charging effects. Thus, it was not possible to determine a value for the defect density of the substrate here. The diffuse background was quite low in both patterns, pointing to clean surfaces and negligible point defects. Additionally, XPS measurements of both substrates showed no carbon contamination, indicating chemically clean surfaces.

After the deposition of NiO, the LEED patterns also exhibited a (1×1) structure related to the square symmetry of the NiO(001) surface for both substrates [see Fig. 6.1(b),(e)]. As mentioned above, due to the rock salt structure, the reciprocal unit vectors of the NiO(001) surface point in [110] and [$\bar{1}$10] directions and are consequently $\sim\sqrt{2}$ times larger than the surface unit cell of $SrTiO_3$ in reciprocal space. Due to the very similar lattice constants of NiO(001) and MgO(001), the diffraction spots were located at almost identical positions. A broadening of the diffraction spots compared to the pattern of the $SrTiO_3$ substrate was clearly visible, indicating an increase of the defect density. Analyzing the FWHM of the (10) surface diffraction spots, we obtained densities of line defects of $(0.8 \pm 0.1)\,\mathrm{nm}^{-2}$ and $(1.1 \pm 0.2)\,\mathrm{nm}^{-2}$ for the NiO/MgO and NiO/$SrTiO_3$, respectively. The slightly larger broadening of the diffraction spots for NiO/$SrTiO_3$ compared to the diffraction spots of the NiO/MgO surface can be related to the formation of more structural defects (e.g., domain boundaries), induced by the higher lattice misfit of NiO(001) on $SrTiO_3$(001). Additionally, both patterns showed a negligible background intensity of the NiO(001) surface, pointing to a small amount of point defects.

The LEED images of Fe_3O_4 obtained after deposition on NiO/MgO(001) and NiO/$SrTiO_3$(001) showed similar diffraction patterns with a square symmetry [see Fig. 6.1(c),(f)]. Clear diffraction spots with half-peak distance compared to the NiO(001) surface indicated an approximately doubled lattice constant in real space due to the almost-doubled cubic lattice constant of Fe_3O_4 compared to the other oxides used here. Furthermore, an additional $(\sqrt{2}\times\sqrt{2})$R45° superstructure appeared, which is characteristic for a well-ordered magnetite surface [77, 124, 125, 144]. This superstructure is not observed for maghemite (Fe_2O_3), which has a very similar surface lattice constant. Therefore, we assume the formation of well-ordered stoichiometric magnetite films. However, the diffraction spots of the magnetite film grown on NiO/MgO were sharper than for the growth on NiO/$SrTiO_3$, indicating a better ordering and less domain boundaries. For the

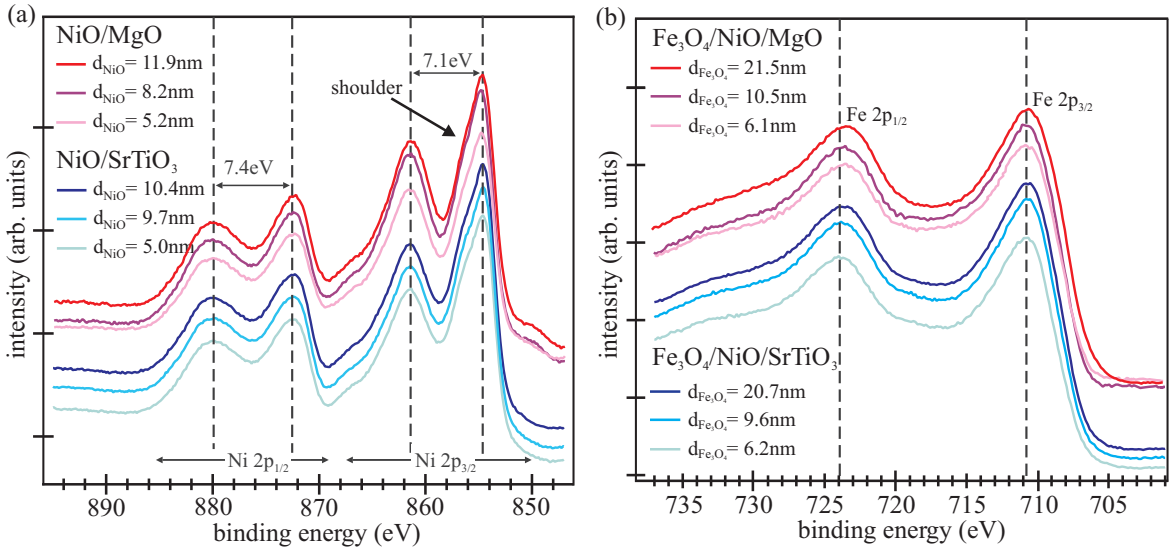

Fig. 6.2: X-ray photoelectron spectra of (a) Ni $2p$ region for the as-prepared NiO films on MgO(001) and $SrTiO_3$; (b) Fe $2p$ region for the as-prepared Fe_3O_4 films on NiO/MgO(001) and NiO/$SrTiO_3$.

density of line defects of the Fe_3O_4 films, values of $(1.3 \pm 0.2)\,\mathrm{nm}^{-2}$ and $(0.14 \pm 0.02)\,\mathrm{nm}^{-2}$ were obtained for the growth on NiO/$SrTiO_3$(001) and NiO/MgO(001), respectively, analyzing the FWHM of the (20) surface diffraction spots.

In summary, the LEED patterns of the Fe_3O_4/NiO bilayer systems confirmed a crystalline cube-on-cube growth of both NiO and Fe_3O_4 films on MgO(001), as well as on $SrTiO_3$(001). The films grown on MgO substrates exhibited a higher crystalline quality and less surface defects compared to the bilayers grown on $SrTiO_3$.

XPS measurements were made directly after deposition of the films to determine the stoichiometry and the valence state of the cation species. Figure 6.2(a) shows the XP spectra of the Ni $2p$ region after the deposition of nickel oxide and before the deposition of iron oxide. All spectra of the Ni $2p$ core level revealed Ni $2p_{3/2}$ and Ni $2p_{1/2}$ peaks at binding energies of 854.6 eV and 872.5 eV, respectively, and two intense satellite structures at about 7 eV higher binding energies. Since these values agree well with the binding energies reported in the literature for a Ni^{2+} valence state in NiO stoichiometry [145, 146], we assume that the oxide films were stoichiometric and had negligible point defects (e.g., oxygen vacancies). Additionally, there was a shoulder ~1.5 eV above the Ni $2p_{3/2}$ peak, which has been reported to be typical for NiO [147, 148]. Thus, the shape of all spectra was comparable to that of NiO bulk crystal [146, 149, 150]. The Fe $2p$ photoelectron spectra of the iron oxide films as prepared on top of the NiO films are presented in Fig. 6.2(b). From the position and shape of the Fe $2p$ peaks, one can obtain information about the iron oxidation state and the stoichiometry. All recorded spectra exhibited the same shape, with main peaks located at binding energies of 710.6 eV and 723.6 eV for Fe $2p_{3/2}$ and Fe $2p_{1/2}$, respectively. These binding energies of the core levels correspond to well-known values of Fe_3O_4 from the literature [122]. Additionally, in contrast to wüstite (FeO) and maghemite (Fe_2O_3), no apparent charge-transfer satellites can be observed between the two main peaks due to their overlap [122, 123]. Consequently, the shape and binding energies of the Fe $2p$ spectra confirmed a mixed Fe^{2+}/Fe^{3+} valence and pointed to a Fe_3O_4 stoichiometry for all prepared iron oxide films. Thus, both XPS and LEED measurements demonstrated that the bilayer structures on both kind of substrates consisted of crystalline stoichiometric NiO and Fe_3O_4 films.

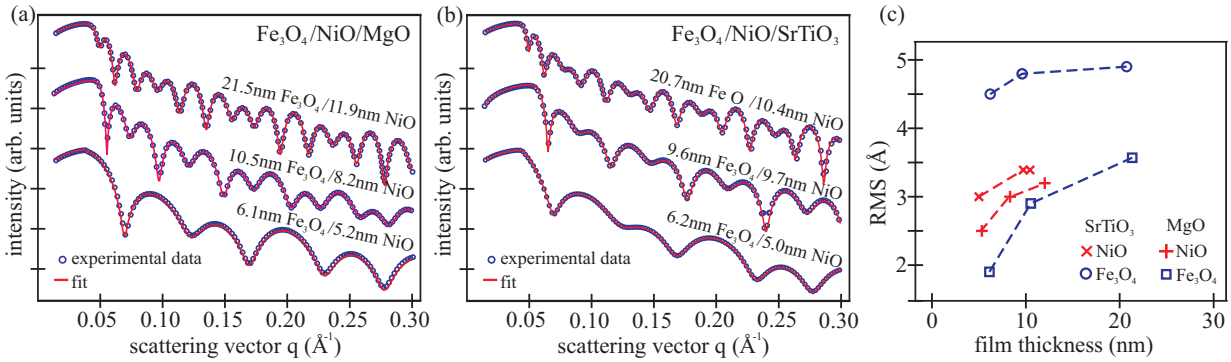

Fig. 6.3: X-ray reflectivity (XRR) measurements and the calculated intensities of the bilayers on (a) MgO and (b) $SrTiO_3$ substrates; (c) Fe_3O_4 surface and Fe_3O_4/NiO interface roughnesses obtained from the XRR measurements.

6.3.2 XRR / XRD

XRR and XRD experiments were performed *ex situ* to determine the structural parameters of the bilayers (e.g., film thicknesses and vertical lattice distances). Figures 6.3(a),(b) show the measured reflectivity curves and the corresponding calculated reflectivity curves after optimizing the structural parameters. In addition, the obtained thicknesses of all studied bilayers are presented. Clear intensity oscillations with beating effects were visible for all samples, indicating double-layer structures and flat homogeneous films with small interface and surface roughness.

The applied calculation model consists of a layer of iron oxide on top of a nickel oxide layer on MgO or $SrTiO_3$ substrate. All fitted curves agreed excellently with the experimental data using literature values for the dispersion $\delta_{Fe_3O_4} = 1.53 \times 10^{-5}$ and $\delta_{NiO} = 1.89 \times 10^{-5}$ [151]. This indicates a small defect density (e.g., oxygen vacancies), which is in accordance with the XPS results.

Additionally, the roughnesses of the films were determined and are presented in Fig. 6.3(c). Here, all films featured an increase of the surface and interface roughness with increasing film thickness. This effect can be attributed to kinetic roughening of the films during growth and to the progressing relaxation process [152]. The nickel oxide films exhibited similar roughnesses of $\sigma_{NiO} = 2.5 - 3.5$ Å on both substrates, with a small increase for thicker films. The roughness of the Fe_3O_4 on NiO/MgO increased more drastically, while the magnetite films deposited on NiO/$SrTiO_3$ showed nearly constant roughness with initially almost doubled values compared to the magnetite films on NiO/MgO. This behavior is likely caused by high lattice misfit and the resulting relaxation process. This is in accordance with the broadened diffraction spots of the Fe_3O_4 films on NiO/$SrTiO_3$ observed in the LEED pattern (see Fig. 6.1).

Figures 6.4(a),(b) present the SR-XRD measurements of the $(00L)$ crystal truncation rod (CTR) compared to intensities calculated by kinematic diffraction theory of the Fe_3O_4/NiO bilayers on MgO(001) and $SrTiO_3$(001), respectively. Here, the bulk nomenclature of the reciprocal space was used, where $L = c\,K_\perp/(2\,\pi)$ in reciprocal lattice units (r.l.u.) denotes the vertical scattering vector $K_\perp$ scaled to the Bragg condition $2\pi/c$ ($c_{MgO} = 4.2117$ Å, $c_{SrTiO_3} = 3.905$ Å). The diffraction data revealed an epitaxial (001)-oriented growth of NiO and Fe_3O_4 on both substrates. Due to the almost-doubled lattice constant of magnetite compared to both MgO and NiO and the resulting lateral tensile strain, the $(004)_S$ spinel reflection was located at higher L values compared to MgO and close to the $(002)_R$ bulk reflection of a rock salt structure. On $SrTiO_3$, both nickel oxide and magnetite exhibited a large lattice misfit and were laterally compressively strained. Thus, the $(004)_S$ reflection of magnetite and $(002)_R$ reflection of NiO were at lower L values compared to

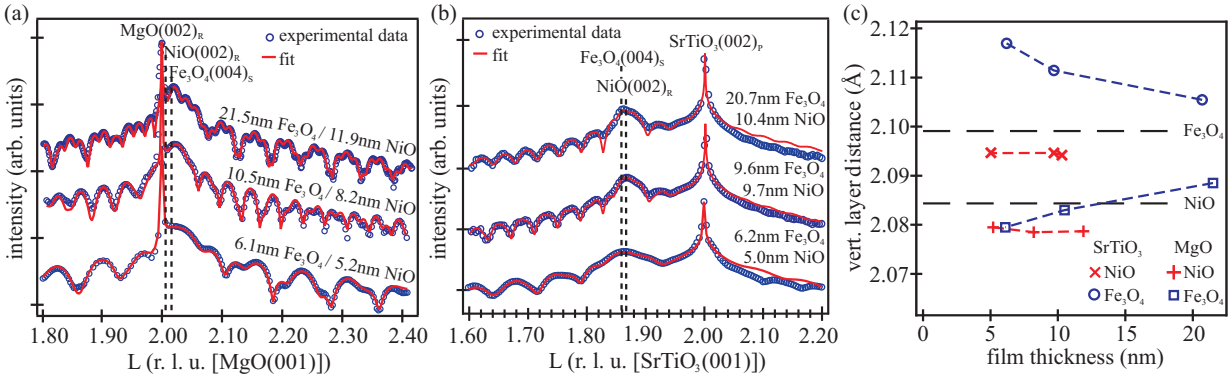

Fig. 6.4: X-ray diffraction (XRD) measurement along the $(00L)$ crystal truncation rod (CTR) (a) of the Fe_3O_4/NiO/MgO samples and (b) of the Fe_3O_4/NiO bilayers on $SrTiO_3$. The calculated intensity distribution using the kinematic approximation is shown in red. (c) Vertical layer distance of nickel oxide and magnetite grown on MgO(001) and $SrTiO_3$(001), dependent on the film thickness. The dashed lines denote the fully relaxed bulk values of magnetite and nickel oxide.

$SrTiO_3$ and were well separated from the $(002)_P$ perovskite reflection of $SrTiO_3$. Here, the indexes R, S, and P indicate bulk indexing for rock salt, spinel, and perovskite types, respectively. For all bilayers grown on MgO, the measurements showed a sharp peak at $L = 2$ originating from the diffraction at the MgO substrate lattice [see Fig. 6.4(a)]. Additionally, broad and rather intense features located at $L \sim 2.02$ accompanied by strong Laue oscillations were visible due to the finite thickness of the iron and nickel oxide films. The well-pronounced intensity oscillations with two superposed partial oscillations clearly showed a periodicity of two layers of different thickness, indicating a high crystalline ordering and homogeneous thicknesses of both films – magnetite and nickel oxide. This is in accordance with the results seen in the XRR measurements.

In the case of bilayers grown on $SrTiO_3$, the $(00L)$ rod also showed a sharp substrate peak at $L = 2$ and Laue oscillations due to crystalline magnetite and nickel oxide films [see Fig. 6.4(b)]. Here, the Bragg peaks originating from the iron and nickel oxide were located at $L \sim 1.86$ and were broadened due to the finite film thicknesses. Upon closer inspection, the Laue oscillations also showed a periodicity of two layers, whereby the damping of the oscillation originating from the magnetite surface increased with increasing magnetite thickness due to increasing roughness [see Fig. 6.3(c)]. This result agrees well with LEED and XRR results shown above.

Due to the small lattice mismatch between Fe_3O_4 and NiO, a separation of the Bragg peaks originating from the respective film is not visible by eye. Complete data analysis using kinematic diffraction theory was performed to obtain the vertical layer distance of the respective oxide film. Within the calculation, the atomic form factors of oxygen, nickel, and iron atoms arranged in a bulk structure were kept constant while the vertical size of the unit cell was varied. Interface roughness was modeled with a Gaussian variation of the height as implemented for XRR by the Névot-Croce model [54]. The applied models consist of a homogeneous Fe_3O_4/NiO bilayer on top of the respective substrate. This structural model involving the number of layers coincides with the layer model and the film thicknesses obtained from XRR calculations. The obtained vertical layer distances ($c_{NiO}/2$ for NiO and $c_{Fe_3O_4}/4$ for Fe_3O_4) are shown in Fig. 6.4(c).

The dashed lines mark the bulk values of the magnetite and nickel oxide. Due to the larger unit cell of MgO(001), pseudomorphic growth of NiO on MgO resulted in an expansion of the NiO unit cell in lateral direction, and thus a vertical compression, and consequently a smaller vertical lattice distance. Exactly the opposite was expected in the case of NiO grown on $SrTiO_3$(001),

due to the smaller bulk unit cell of $SrTiO_3$ compared to NiO. Thus, the vertical lattice distance of NiO was larger than the bulk value, as observed in the experiment.

For the NiO layers on MgO, the vertical layer distance exhibited a compressive strain (2.078 Å) due to lateral tension, and showed no dependence on the NiO thickness in the investigated range [see Fig. 6.4(c)]. In the case of bilayers grown on $SrTiO_3$, the vertical lattice distance of NiO (2.095 Å) pointed to tensile strain as a result of the lateral compression. Further, there was no dependence on the NiO thickness.

However, the situation was different for the relaxation of the magnetite films. Due to pseudomorphic growth of NiO on MgO, the vertical layer distance of Fe_3O_4 grown on top of NiO/MgO was also slightly compressively strained but relaxed to higher values with increasing magnetite thickness. Its value relaxed from 2.0795 Å for the 6.1 nm thick magnetite film to 2.0885 Å for the thickest magnetite film. A strong relaxation with increasing film thickness of the magnetite could also be seen for magnetite films grown on NiO/$SrTiO_3$. The vertical lattice distance of Fe_3O_4 on NiO/$SrTiO_3$ was exposed to heavy tensile strain and decreased rapidly from 2.117 Å for the thinnest film to 2.106 Å for the 20.7 nm thick magnetite film.

6.3.3 VSM

As an example, the magnetic properties of the two thickest magnetite films on NiO/MgO and NiO/$SrTiO_3$ were studied by means of VSM. The magnetization curves were measured for different azimuthal sample directions α between the substrate [100] direction and the applied magnetic field. Figures 6.5(a),(b) show the magnetic moment per f.u.(formula unit) as a function of the magnetic field for the bilayers on MgO and $SrTiO_3$, respectively, for two different directions of the external magnetic field.

For both samples, a typical ferro(i)magnetic behavior was observed. Here, the red curves recorded with the magnetic field applied in the [010] direction of the substrates represent magnetic easy axes with a high magnetic remanence and coercive fields. The blue curves recorded with the magnetic field applied in the [110] direction exhibit the magnetic behavior of a magnetic hard axis due to a lower strength of the coercive field and a smaller magnetic remanence. However, from magnetic saturation to magnetic remanence, neither investigated sample was in a monodomain state. This can also be concluded from the squareness (magnetic remanence value divided by the saturation magnetization) for the field loop of the magnetic easy direction which is below one. This effect is probably originated in the presence of antiphase boundaries that pin the magnetic moments in different directions and, thus, support multidomain states rather than monodomain states, even for the case of having the magnetization aligned in the magnetic easy direction. The Fe_3O_4 film on NiO/$SrTiO_3$ showed an enhanced coercive field compared to the magnetite film grown on NiO/MgO. One possible reason could be a higher density of grain boundaries due to the relaxation process, which supports pinned multidomain states that need larger magnetic fields to be switched. This is consistent with the weaker structural quality (e.g., high roughness, broad diffraction peaks) seen in the LEED, XRR, and XRD measurements. Further, the saturation magnetization of the Fe_3O_4 film grown on NiO/MgO amounted to $(3.7 \pm 0.3)\,\mu_B$/f.u., and was rather close to the literature value of $4.07\,\mu_B$/f.u. [11, 153]. In contrast, magnetite on NiO/$SrTiO_3$ showed a lower magnetic moment of $(3.3 \pm 0.3)\,\mu_B$/f.u., which may result from the antiferromagnetic coupling in the vicinity of antiphase domain boundaries (APBs) [154].

The remanent magnetization as a function of azimuthal sample angle α is shown in Fig. 6.5(c) for both investigated samples. The maxima of the magnetic remanence pointed in ⟨100⟩ directions for both Fe_3O_4 films on NiO/MgO and NiO/$SrTiO_3$, indicating the magnetic easy directions. Consequently, the magnetic hard axes were located in ⟨110⟩ directions.

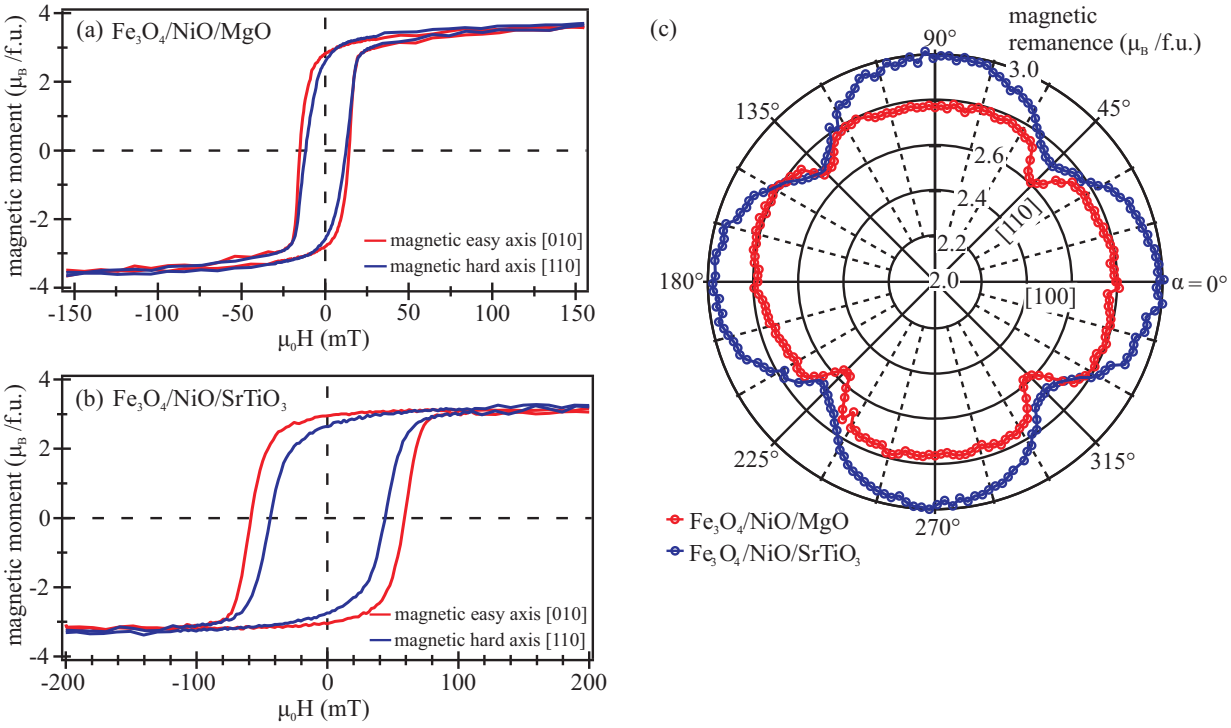

Fig. 6.5: Vibrating sample magnetometry (VSM) magnetization curves of magnetic easy and hard directions for (a) 21.5 nm-thick Fe_3O_4 film on NiO/MgO and (b) 20.7 nm-thick Fe_3O_4 film on NiO/$SrTiO_3$. (c) Polar plot of the magnetic remanence depending on the azimuthal sample angle α of a 21.5 nm-thick Fe_3O_4 film on NiO/MgO (red) and 20.7 nm-thick Fe_3O_4 film on NiO/$SrTiO_3$ (blue).

6.4 Discussion

XPS measurements taken directly after deposition revealed stoichiometric Fe_3O_4 and NiO on both substrates, independent of the film thicknesses. Due to the limited mean free path of the electrons, only the near-surface region (~ 5 nm) of the layers could be characterized. No evidence for the formation of non-stoichiometric magnetite was observed in this region. Pilard *et al.* found a 1.5 nm-thick $NiFe_2O_4$ interfacial layer after depositing NiO above 610°C on Fe_3O_4 [140]. Within the XPS measurements presented here, the interfacial region could be detected only for the thinnest magnetite films showing spectral shape and binding energies typical for Ni^{2+} in NiO stoichiometry. Thus, there was no evidence for the formation of $NiFe_2O_4$ due to the lower growth temperature.

Hard x-ray photoelectron spectroscopy (HAXPES) and x-ray magnetic circular dichroism (XMCD) measurements [141] of the same samples recorded after transport under ambient conditions showed small traces of Fe^{3+} excess on the surface of the bilayers grown on $SrTiO_3$. However, in deeper layers and at the interface, the presence of stoichiometric NiO and Fe_3O_4 was confirmed, excluding the formation of $NiFe_2O_4$ clusters or any interfacial layer also for thicker Fe_3O_4 films [141]. Consequently, very thin magnetite films tend to form maghemite at the surface after exposure to ambient air whereas thicker films seem to be more stable, as reported previously by Fleischer *el al.* [155]. Since *in situ* XPS and LEED measurements taken after preparation under UHV conditions showed no evidence for maghemite, a capping layer deposited directly after growth could prevent the possible oxidation process in the upper layers.

In situ LEED measurements also verified the Fe_3O_4 stoichiometry of the iron oxide film showing the typical $(\sqrt{2} \times \sqrt{2})R45°$ superstructure of the magnetite surface for all investigated films. Further, NiO films on both substrates exhibited the expected (1×1) pattern due to the rock salt crystal structure. The diffraction spots of the magnetite and NiO films grown on $SrTiO_3$ were slightly broadened compared to the films grown on MgO, indicating the formation of more surface defects due to the high lattice misfit. Surface roughnesses obtained from the XRR analysis exhibited higher values for all films grown on $SrTiO_3$. While the roughness of the nickel oxide films deposited on $SrTiO_3$ was only about 0.5 Å higher than after deposition on MgO, the magnetite films on NiO/$SrTiO_3$ initially showed almost doubled values compared to the magnetite films on NiO/MgO. This result is consistent with the higher value for the defect density of Fe_3O_4/NiO/$SrTiO_3$ obtained from the LEED pattern analysis. Nevertheless, the XRR measurements provided distinct intensity oscillations, indicating double layer structures and homogeneous film thicknesses. Thus, the two layers did not intermix during the deposition process.

The entire structure of the samples was investigated by XRD measurements of the specular CTR. For all samples, the thickness determined by XRR agreed well with the number of layers obtained from XRD analysis, where distinct Laue oscillations were observed. The strong intensity oscillations revealed crystalline and well-ordered nickel oxide and magnetite films with homogeneous thicknesses on both substrates.

The vertical layer distances of all NiO films showed no dependence on the thickness in the investigated range. However, NiO and Fe_3O_4 films grown on MgO exhibited a vertical compressive strain while NiO and Fe_3O_4 films on $SrTiO_3$ showed vertical tensile strain due to lattice matching at the interface. Based on elastic theory for continuum, the vertical lattice constant c for homogeneous tetragonally (in-plane) distorted films is related to the lateral lattice constant a via [23]

$$\frac{\Delta c}{c} = \frac{2\nu}{\nu - 1}\frac{\Delta a}{a} \quad . \tag{6.1}$$

For the calculation of the vertical layer distance for a completely strained film, Δa from pseudomorphic growth was used. Assuming a Poisson number of $\nu = 0.21$ for NiO [73], the vertical layer distance of pseudomorphic nickel oxide on MgO was calculated to be 2.079 Å. Hence, the NiO films grown on MgO were fully strained as clarified by Fig. 6.6 where lateral distances of (100) planes are presented. Above a critical thickness d_c, this strain should reduce rapidly due to the stable formation of dislocations. Following the model of Matthews and Blakeslee [31], the critical thickness d_c, at which the generation of misfit dislocation will begin, can be calculated by the formula

$$\frac{d_c}{b} = \frac{\left(1 - \nu\cos^2\alpha\right)\left(\ln\left(\frac{d_c}{b}\right) + 1\right)}{2\,\pi\,f\,(1+\nu)\,\cos(\lambda)} \quad . \tag{6.2}$$

Here, b is the magnitude of the Burgers vector, f is the lattice mismatch, ν is the Poisson ratio, $\alpha = 90°$ is the angle between the Burgers vector and the dislocation line, and $\lambda = 45°$ is the angle between the Burgers vector and the direction both normal to the dislocation line and within the plane of the interface. For NiO films on MgO(001), the critical thickness was determined to 39 nm. Since the studied films were below the critical thickness, the absence of strain relaxation is in good agreement with this model. Similar results were also observed by Schemme *et al.* [121] for NiO films of different thicknesses up to 34 nm grown on MgO(001). The experimental data of James *et al.* [73] showed a strain relaxation above $\sim$ 40 nm, which is consistent with our observations and confirms Eq. (6.2).

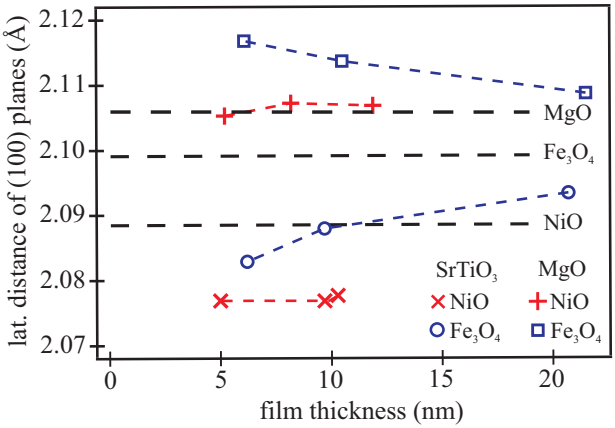

Fig. 6.6: Lateral distance of (100) planes of all prepared magnetite and nickel oxide films calculated using Eq. (6.1) and the vertical layer distances obtained from XRD analysis. The dashed lines denote the fully relaxed bulk values of MgO, Fe_3O_4, and NiO.

Despite the large misfit of −6.9% between NiO and $SrTiO_3$, the XRD curves of all studied films also featured distinct Laue oscillations, pointing to a good crystalline ordering. Assuming a complete lattice matching at the interface, we calculated a vertical lattice distance of 2.161 Å for fully strained NiO films on $SrTiO_3$ [Eq. (6.1)], while we observed a film thickness independent value of 2.095 Å. The resulting lateral distances of the (100) planes calculated by Eq. (6.1) of all investigated nickel oxide and magnetite films are presented in Fig. 6.6. Thus, for the NiO films grown on $SrTiO_3$, the remaining lateral strain only amounted to −0.6% (see Fig. 6.6). For the critical thickness, Eq. (6.2) revealed a value of 3.5 nm. All prepared NiO films were well above the critical thickness. Thus, the observed strong strain relaxation seems to be reasonable although they were not completely relaxed. We assume that the residual strain cannot be removed from the film due to kinetic barriers preventing the film from relaxing completely. Similar strain behavior was reported by Zhang *et al.* for NiO films of 2 nm thickness grown by pulsed laser deposition on $SrTiO_3$ substrates. In contrast to our findings, a complete relaxation for NiO films of thicknesses above 10 nm was observed, probably driven by higher deposition temperature [139].

In the case of Fe_3O_4 on NiO/MgO, we calculated a vertical layer distance for a fully strained film of 2.092 Å and a critical thickness of 105 nm ($\nu = 0.356$ [156], $f = 0.3\%$), applying Eq. (6.1) and (6.2), respectively. Here, the misfit f coincided with the misfit of magnetite on MgO since the growth of NiO on MgO was pseudomorphic adapting its lateral lattice constant (see Fig. 6.6). All our investigated magnetite films on NiO/MgO were strongly strained having a lower vertical layer distance than received by Eq. (6.1). Further, the calculated lateral layer distance of all prepared Fe_3O_4 films was larger than that of the NiO films pseudomorphically grown on MgO (see Fig. 6.6). Consequently, the magnetite films were exposed to much higher tensile lateral strain as expected from classical growth theory. This effect may be attributed to the unpreventable formation of APBs, which is not considered in the simple theories of epitaxial growth and relaxation via misfit dislocations. Thus, we assume that APBs expose additional tensile strain to the magnetite film. This result is in contrast to the compressive strain due to APBs as reported for magnetite films (thickness range 85 − 600 nm) directly grown on MgO(001) by magnetron sputtering [157]. As shown in Fig.6.4(c), the measured vertical layer distance approached the bulk value with increasing Fe_3O_4 thickness. However, the bulk value was not reached even for the thickest magnetite film on NiO/MgO studied here. On one hand, this effect is very surprising since the predicted critical thickness of 105 nm is beyond the thicknesses under consideration here. On the other hand, this behavior of partial relaxation below the calculated critical thickness also coincides with the results

reported by Schemme *et al.* [121]. We also attribute this effect to the unpreventable formation of APBs, which is not considered in the simple theories for the nucleation of misfit dislocations. Thus, APBs seem to lower the kinetic barrier for the formation of dislocations.

Regardless of the low remaining compressive strain between the Fe_3O_4 and NiO/$SrTiO_3$, these magnetite films were less structurally ordered than the magnetite films grown on NiO/MgO. While the crystalline quality of the NiO films on $SrTiO_3$ was constantly high independent of the film thickness, the strength of Laue oscillations of the Fe_3O_4 films grown on top of NiO/$SrTiO_3$ decreased with increasing magnetite thickness. This result is supported by the high surface roughness of the magnetite films obtained from the XRR measurements as well as by the broadened diffraction spots seen in the LEED pattern.

Assuming a pseudomorphic growth of magnetite on the strained NiO film with remaining lattice mismatch of -1%, the vertical layer distance of a fully strained magnetite film was calculated to be 2.123 Å using Eq. (6.1). The measured value of 2.117 Å for the 5 nm-thick magnetite film was already lower than the expected value for pseudomorphic growth [see Fig. 6.4(c)]. Thus, this magnetite film was already partially relaxed and showed vertical and lateral strain of 0.9% and 0.8%, respectively (see Fig. 6.6). With increasing thickness of the magnetite film, the vertical and lateral layer distances strongly relaxed further to 2.104 Å and 2.093 Å, respectively, for the 20.7 nm-thick film. Again, this effect contradicts classical relaxation theory via dislocation formation from which the critical film thickness of 27 nm was obtained using Eq. (6.2). Consequently, the formation of grain boundaries and structural defects (e.g., APBs) during the initial stage of film growth may support the formation of misfit dislocations, and thus a faster relaxation process. In addition, as stated above, the lateral tensile strain due to APBs may cause a larger lateral layer distance compared to pseudomorphic growth on the strained NiO film.

VSM measurements of the two thickest magnetite films on NiO/MgO and NiO/$SrTiO_3$ revealed ferro(i)magnetic behavior for both samples. However, the Fe_3O_4 film grown on NiO/$SrTiO_3$ showed enhanced coercive field compared to the film on NiO/MgO, possibly caused by a higher density of grain boundaries, and thus the formation of more pinning centers as confirmed by the LEED analysis. This behavior coincides with the weaker structural ordering and higher surface roughness of the magnetite films on NiO/$SrTiO_3$, also seen in the XRD and XRR measurements. An increased coercive field for magnetite films grown on $SrTiO_3$ caused by a higher surface roughness or strain has also been reported in Refs. [158, 159].

The obtained saturation magnetization values of Fe_3O_4 grown on NiO/MgO and NiO/$SrTiO_3$ coincided within the error tolerances with the values determined by XMCD [141]. Additionally, the value of Fe_3O_4 film on NiO/MgO was also rather close to the ideal theoretical value as well as to the experimental bulk moment of magnetite of 4.07 μ_B/f.u. [11, 79, 153], whereas Fe_3O_4 on NiO/$SrTiO_3$ exhibited a lower value. A reduced magnetic moment has also been reported for Fe_3O_4/$SrTiO_3$ systems, possibly caused by a large density of APBs induced by high lattice mismatch [135, 160]. This result is supported by a weaker structural ordering as well as higher coercive fields and, thus, a higher density of grain boundaries observed for Fe_3O_4 on NiO/$SrTiO_3$.

Further, both investigated samples showed a fourfold magnetic in-plane anisotropy with magnetic easy axes aligned along the ⟨100⟩ directions. For thin magnetite films on MgO(001), the magnetic easy axes are mostly reported to point into ⟨110⟩ directions [159, 161, 162] as expected from bulk properties of Fe_3O_4. However, a magnetic isotropic behavior [162, 163] or magnetic easy axes aligned in ⟨100⟩ directions [164] are also presented in the literature for Fe_3O_4/MgO(001). Moreover, magnetite films grown on an iron buffer layer deposited on MgO(001) also exhibited a magnetic in-plane anisotropy with magnetic easy axes parallel to ⟨100⟩ [17]. For Fe_3O_4 films on $SrTiO_3$(001), different orientations of the magnetic easy axes were also reported. While Kale *et al.* observed a fourfold magnetic anisotropy with magnetic easy axes pointing into ⟨110⟩ directions

[163], magnetic easy axes aligned along the ⟨100⟩ directions are presented in Refs. [136, 164]. All these observations show that the magnetic properties of magnetite are highly affected by the interface between the film and substrate and can be influenced by the deposition conditions, lattice mismatch, or stoichiometric deviations. In addition, we assume that a tetragonal distortion of the films can influence the spin-orbit coupling, which may lead to modified magnetocrystalline anisotropy constants [165] and, thus, altered directions of magnetic easy and hard axes.

6.5 Conclusions

We present a comparative study on the structural and magnetic properties of Fe_3O_4/NiO bilayers grown on MgO(001) and Nb-doped $SrTiO_3$(001). Stoichiometric magnetite and NiO films with homogeneous thicknesses were found on both substrates in the investigated thickness range ($5 - 20\,\mathrm{nm}$). Detailed analysis of the XRD measurements revealed a high crystallinity of the NiO films independent of the underlying substrate or film thickness. However, magnetite films grown on NiO/$SrTiO_3$ showed a weaker structural ordering and higher surface roughness compared to the films grown on NiO/MgO, induced by a large lattice mismatch and the resulting relaxation process. Further, the bilayers exhibited a vertical compressive strain on MgO but a tensile strain in the vertical direction on $SrTiO_3$ as a result of lateral compression. The weaker crystalline structure of Fe_3O_4 on NiO/$SrTiO_3$ affected the magnetic properties leading to an enhanced coercive field and a reduced magnetic moment compared to magnetite on NiO/MgO. Nevertheless, these Fe_3O_4/NiO bilayers on MgO and $SrTiO_3$ substrates are expected to show large thermoelectric effects based on the thermal generation of spin currents (spin Seebeck effect) [112–114], supported by the antiferromagnetic NiO layer [21, 22].

Additionally, both systems showed a fourfold magnetic in-plane anisotropy with magnetic easy axes pointing in ⟨100⟩ directions which were 45° rotated to the well-known magnetic easy axes directions of thin magnetite films on MgO(001) as expected from bulk properties. One potential reason may be a modified spin-orbit coupling as a result of the tetragonal distortion of the films leading to altered magnetocrystalline anisotropy. A detailed understanding of these bilayers is of the utmost importance since they are excellent candidates for potential spintronic and spin caloritronic applications. Therefore, this behavior deserves further study to shed more light on this interesting change of the magnetic anisotropy of Fe_3O_4 thin films grown on NiO/MgO(001) and NiO/$SrTiO_3$(001).

6.6 Acknowledgments

Portions of this research were carried out at beamline I811, MaXLab synchrotron radiation source, Lund University, Sweden. Funding for the beamline I811 project was kindly provided by The Swedish Research Council and The Knut och Alice Wallenbergs Stiftelse. Additional experiments were performed at the X04SA beamline at the Swiss Light Source synchrotron radiation source at Paul Scherrer Institute, Villigen, Switzerland. We like to thank the I811 and X04SA beamline staff for experimental support. Further, we acknowledge support by Deutsche Forschungsgemeinschaft (DFG) and Open Access Publishing Fund of Osnabrück University.

Original publication: Physical Review B **94**, 094423 (2016)
available at http://dx.doi.org/10.1103/PhysRevB.94.094423

From Fe_3O_4/NiO bilayers to $NiFe_2O_4$-like thin films through Ni interdiffusion

O. Kuschel, R. Buß, W. Spiess, T. Schemme, J. Wöllermann, K. Balinski, A. T. N'Diaye, T. Kuschel, J. Wollschläger, and K. Kuepper

Abstract

Ferrites with (inverse) spinel structure display a large variety of electronic and magnetic properties, making some of them interesting for potential applications in spintronics. We investigate the thermally induced interdiffusion of Ni^{2+} ions out of NiO into Fe_3O_4 ultrathin films resulting in off-stoichiometric nickel ferrite-like thin layers. We synthesized epitaxial Fe_3O_4/NiO bilayers on Nb-doped $SrTiO_3$(001) substrates by means of reactive molecular beam epitaxy. Subsequently, we performed an annealing cycle comprising three steps at temperatures of 400°C, 600°C, and 800°C under an oxygen background atmosphere. We studied the changes of the chemical and electronic properties as result of each annealing step with help of hard x-ray photoelectron spectroscopy and found a rather homogeneous distribution of Ni and Fe cations throughout the entire film after the overall annealing cycle. For one sample we observed a cationic distribution close to that of the spinel ferrite $NiFe_2O_4$. Further evidence comes from low energy electron diffraction patterns indicating a spinel type structure at the surface after annealing. Site and element specific hysteresis loops performed by x-ray magnetic circular dichroism uncovered the antiferrimagnetic alignment between the octahedral coordinated Ni^{2+} and Fe^{3+} ions and the Fe^{3+} in tetrahedral coordination. We find a quite low coercive field of 0.02 T, indicating a rather low defect concentration within the thin ferrite films.

8 Summary and outlook

Within this thesis, the growth behavior accompanied by the resulting structural, electronic and magnetic properties of pure magnetite films as well as Fe_3O_4/NiO bilayers on Nb:$SrTiO_3$(001) substrates has been investigated. Subsequently, thermal stability of the bilayers and the induced interdiffusion process have been studied successively providing an alternative pathway for the preparation of ultrathin nickel ferrite films.

In the first step, the impact of different deposition temperatures on the film growth has been studied strongly affecting the relaxation behavior and structural quality of the magnetite films. The growth process of Fe_3O_4 on $SrTiO_3$ substrates has been monitored *in situ* during deposition by means of XRD. At a deposition temperature of 400°C, the magnetite film exhibits a fully relaxed vertical lattice constant even in the early growth stages. However, a residual interfacial layer of ∼1 nm is observed additionally. The interlayer is supposed to have a high density of point defects and misfit dislocations, which leads to a fast strain relaxation and, subsequently, to the growth of an ordered fully relaxed magnetite film on top. In contrast, the film deposited at 270°C shows a strong vertical compressive strain and relaxes continuously towards the bulk value with increasing film thickness. Additionally, a lateral tensile strain is observed, which contradicts the anticipated strain behavior due to a lattice mismatch of -7.5% and requires further investigations, e.g., high resolution TEM measurements. Despite a strong relaxation process across the whole film, the sample deposited at 270°C features a higher ordering of the magnetite sublattices due to a higher occupancy of the tetrahedral sites compared to the sample deposited at 400°C. Thus, for higher deposition temperatures a relocation of the iron ions from tetrahedral sites to octahedral vacancies can be assumed, leading to a formation of a deficient rock salt like lattice. In conclusion, the strain relaxation as well as the ordering of the tetrahedral sublattice in magnetite are strongly correlated with the substrate temperature during deposition. Further, the lateral ordering of magnetite films can be improved by subsequent annealing.

The crystal structure of magnetite and, thus, the ordering of the tetrahedral lattice sites strongly affect its magnetic properties, which can be important for spintronic devices that contain magnetite thin films. Therefore, experiments disclosing the magnetic structure of these magnetite films (e.g., XMCD) should be performed in future studies and correlated with the structural ordering.

As a second step, a comparative study on the morphology, the structural and magnetic properties of Fe_3O_4/NiO bilayers on MgO and $SrTiO_3$ substrates has been shown. Here, a stoichiometric and crystalline cube-on-cube growth of NiO and Fe_3O_4 films on both MgO and $SrTiO_3$ is confirmed using several investigation techniques, e.g., XPS, LEED and XRD. However, the bilayers grown on MgO substrates exhibit a higher structural ordering and less surface defects compared to the bilayers grown on $SrTiO_3$. One reason is the large lattice mismatch and, thus, a fast strain relaxation for the bilayers on $SrTiO_3$. While the NiO films grow pseudomorphic on MgO without any relaxation, the films on $SrTiO_3$ show strong relaxation with remaining lateral strain of -0.6% for all thicknesses. Nevertheless, the situation is different for magnetite films which exhibit strong relaxation, even for films of 5 nm thickness on both NiO/MgO and NiO/$SrTiO_3$.

Furthermore, the weaker crystalline structure of Fe_3O_4 on NiO/$SrTiO_3$ compared to NiO/MgO affects the magnetic properties leading to an enhanced coercive field and a reduced magnetic

moment, studied by means of VSM. Both systems show a fourfold magnetic in-plane anisotropy with magnetic easy axes pointing in ⟨100⟩ directions 45° rotated to the well-known magnetic easy axes in ⟨110⟩ directions of thin magnetite films on MgO(001) as expected from bulk properties. One potential reason may be a modified spin-orbit coupling as a result of the tetragonal distortion of the films leading to an altered magnetic anisotropy. Here, additional work on magnetite films with increasing thicknesses is required to investigate the transition of the magnetic anisotropy towards bulk behavior. Moreover, future spin and charge transport measurements in these bilayers are planned to study enhancement of the transport properties by the antiferromagnetic NiO layer.

In the last step, the modification of the crystallographic, electronic, and magnetic properties of Fe_3O_4/NiO bilayers on $SrTiO_3$(001) has been investigated induced by thermally driven interdiffusion. Post-deposition annealing experiments for different thickness ratios of the bilayers have been performed and the interdiffusion process has been monitored by soft XPS and high-resolution angle-resolved HAXPES to control the stoichiometry and chemical properties for the individual annealing steps. The structural analysis reveals that the annealing cycle at 600°C leads to homogeneous layers of $Ni_xFe_{3-x}O_4$. In case of a NiO excess, further annealing at higher temperatures results in a formation of a NiO layer on top of the film stack due to segregation through the ferrite film after a stoichiometric $NiFe_2O_4$ has already been formed. The resulting magnetic properties of the thin films are studied by XMCD and analyzed using complementary charge-transfer multiplet simulations. The magnetic properties after the last annealing cycle are dominated by the contribution of the Ni^{2+} ions. In case of the ferrite-like $Ni_xFe_{3-x}O_4$ with lower amount of Ni than in stoichiometric nickel ferrite, the measured magnetic moment corresponds quite well to the value recently reported for stoichiometric $NiFe_2O_4$ thin films [12]. In contrast, for the sample consisting of a stoichiometric $NiFe_2O_4$ and a NiO layer on top, a lower magnetic moment is found. This behavior can be explained by the formation of (antiferromagnetic) NiO-rich islands or clusters at the surface.

In conclusion, a multitechnique approach considering the structural, chemical, electronic and magnetic properties has led to a rather complete and conclusive picture which is also in good agreement with corresponding model calculations. Thus, an alternative pathway has been demonstrated to form ultrathin nickel ferrite of high crystalline quality by interdiffusion of bilayers. However, slight stoichiometric deviations such as gradients or not ideal occupation of the respective lattice sides can alter the magnetic and electronic transport properties. Here, transport measurements concerning both charge and spin currents on the intermixed films are planned for further studies. Further, thin $Ni_xFe_{3-x}O_4$ films with a tunable band gap can be obtained employing this method. This might be of interest for several applications, e.g., in the field of spintronics (spin valves) or for experiments concerning the spin Hall magnetoresistance or the spin Seebeck effect. Consequently, additional transport effects based on either charge or spin currents can be amplified or suppressed depending on the bad gap properties of the $Ni_xFe_{3-x}O_4$ material. Here, further systematic investigations of the interdiffusion process of Fe_3O_4/NiO bilayers of different thickness ratios are needed.

In the present work only one stacking order Fe_3O_4 on NiO has been investigated. Further studies including the influence of the stacking order on the interdiffusion process are planned in the future. Moreover, other material combinations such as Fe_3O_4 on CoO have been successfully utilized recently to form stoichiometric $CoFe_2O_4$ through interdiffusion [193]. Here, further studies on other material classes such as garnets etc. would be of large interest.

9 List of publications

Peer-reviewed publications

1. R. Silber, O. Stejskal, L. Beran, P. Cejpek, R. Antoš, T. Matalla-Wagner, J. Thien, O. Kuschel, J. Wollschläger, M. Veis, T. Kuschel, and J. Hamrle
"Quadratic magneto-optic Kerr effect spectroscopy of Fe epitaxial films on MgO(001) substrates"
Physical Review B **100**, 064403 (2019); doi:10.1103/PhysRevB.100.064403
2. O. Kuschel, N. Pathé, T. Schemme, K. Ruwisch, J. Rodewald, R. Buß, F. Bertram, T. Kuschel, K. Kuepper, and J. Wollschläger
"Impact of strain and morphology on magnetic properties of Fe_3O_4/NiO bilayers grown on Nb:$SrTiO_3$(001) and MgO(001)"
Materials **11**, 1122 (2018); doi:10.3390/ma11071122
3. P. Bougiatioti, C. Klewe, D. Meier, O. Manos, O. Kuschel, J. Wollschläger, L. Bouchenoire, S. D. Brown, J.-M. Schmalhorst, G. Reiss, and T. Kuschel
"Quantitative disentanglement of the spin Seebeck, proximity-induced, and ferromagnetic-induced anomalous Nernst effect in normal-metal-ferromagnet bilayers"
Physical Review Letters **119**, 227205 (2017); doi:10.1103/PhysRevLett.119.227205
4. O. Kuschel, W. Spiess, T. Schemme, J. Rubio-Zuazo, K. Kuepper, and J. Wollschläger
"Real-time monitoring of the structure of ultrathin Fe_3O_4 films during growth on Nb-doped $SrTiO_3$(001)"
Applied Physics Letters **111**, 041902 (2017); doi:10.1063/1.4995408
5. O. Kuschel, R. Buß, W. Spiess, T. Schemme, J. Wöllermann, K. Balinski, A. T. N'Diaye, T. Kuschel, J. Wollschläger, and K. Kuepper
"From Fe_3O_4/NiO bilayers to $NiFe_2O_4$-like thin films through Ni interdiffusion"
Physical Review B **94**, 094423 (2016); doi:10.1103/PhysRevB.94.094423
6. K. Kuepper, O. Kuschel, O. Pathé, T. Schemme, J. Schmalhorst, A. Thomas, E. Arenholz, M. Gorgoi, R. Ovsyannikov, S. Bartkowski, G. Reiss, and J. Wollschläger
"Electronic and magnetic structure of epitaxial Fe_3O_4(001)/NiO heterostructures grown on MgO(001) and Nb-doped $SrTiO_3$(001)"
Physical Review B **94**, 024401 (2016); doi:10.1103/PhysRevB.94.024401
7. C. Klewe, T. Kuschel, J.-M. Schmalhorst, F. Bertram, O. Kuschel, J. Wollschläger, J. Strempfer, M. Meinert, and G. Reiss
"Static magnetic proximity effect in Pt/$Ni_{1-x}Fe_x$ bilayers investigated by x-ray resonant magnetic reflectivity"
Physical Review B **93**, 214440 (2016); doi:10.1103/PhysRevB.93.214440
8. T. Nordmann, O. Kuschel, and J. Wollschläger
"Epitaxial growth of ultrathin MgO layers on Fe_3O_4(001) films"
Applied Surface Science **381**, 28 (2016); doi:10.1016/j.apsusc.2016.02.133

9. T. Kuschel, C. Klewe, P. Bougiatioti, O. Kuschel, J. Wollschläger, L. Bouchenoire, S. D. Brown, J.-M. Schmalhorst, D. Meier, and G. Reiss
"Static magnetic proximity effect in Pt layers on sputter-deposited $NiFe_2O_4$ and on Fe of various thicknesses investigated by XRMR"
IEEE Transactions on Magnetics **52**, 4500104 (2016); doi:10.1109/TMAG.2015.2512040

10. O. Kuschel, F. Diek, H. Wilkens, S. Gevers, J. Rodewald, C. Otte, M. H. Zoellner, G. Niu, T. Schroeder, and J. Wollschläger
"Plasma enhanced complete oxidation of ultrathin epitaxial praseodymia films on Si(111)"
Materials **8**, 6379 (2015); doi:10.3390/ma8095312

11. T. Schemme, O. Kuschel, F. Bertram, K. Kuepper and J. Wollschläger
"Structure and morphology of epitaxially grown Fe_3O_4/NiO bilayers on MgO(001)"
Thin Solid Films **589**, 526 (2015); doi:10.1016/j.tsf.2015.06.018

12. T. Kuschel, C. Klewe, J.-M. Schmalhorst, F. Bertram, O. Kuschel, T. Schemme, J. Wollschläger, S. Francoual, J. Strempfer, A. Gupta, M. Meinert, G. Götz, D. Meier, and G. Reiss
"Static magnetic proximity effect in Pt/$NiFe_2O_4$ and Pt/Fe bilayers investigated by x-ray resonant magnetic reflectivity"
Physical Review Letters **115**, 097401 (2015); doi:10.1103/PhysRevLett.115.097401

13. A. Thomas, S. Niehörster, S. Fabretti, N. Shepheard, O. Kuschel, K. Küpper, J. Wollschläger, P. Krzysteczko, and E. Chicca
"Tunnel junction based memristors as artificial synapses"
Frontiers in Neuroscience **9**, 241 (2015); doi:10.3389/fnins.2015.00241

14. L. Marnitz, K. Rott, S. Niehörster, C. Klewe, D. Meier, S. Fabretti, M. Witziok, A. Krampf, O. Kuschel, T. Schemme, K. Kuepper, J. Wollschläger, A. Thomas, G. Reiss, and T. Kuschel
"Sign change in the tunnel magnetoresistance of Fe_3O_4/MgO/Co-Fe-B magnetic tunnel junctions depending on the annealing temperature and the interface treatment"
AIP Advances **5**, 047103 (2015); doi:10.1063/1.4917018

15. H. Schäfer, S. M. Beladi-Mousavi, L. Walder, J. Wollschläger, O. Kuschel, S. Ichilmann, A. Sedaf, M. Steinhart, K. Küpper, and L. Schneider
"Surface oxidation of stainless steel: oxygen evolution electrocatalysts with high catalytic activity"
ACS Catalysis **5**, 2671 (2015); doi:/10.1021/acscatal.5b00221

16. H. Wilkens, O. Schuckmann, R. Oelke, S. Gevers, A. Schaefer, M. Bäumer, M. H. Zoellner, T. Schroeder, and J. Wollschläger
"Stabilization of the ceria ι-phase (Ce_7O_{12}) surface on Si(111)"
Applied Physics Letters **102**, 111602 (2013); doi:/10.1063/1.4795867

17. H. Wilkens, O. Schuckmann, R. Oelke, S. Gevers, M. Reichling, A. Schaefer, M. Bäumer, M. H. Zoellner, G. Niu, T. Schroeder, and J. Wollschläger
"Structural transitions of epitaxial ceria films on Si(111)"
Physical Chemistry Chemical Physics **15**, 18589 (2013); doi:/10.1039/C3CP52688G

Submitted publications

1. P. Bougiatioti, O. Manos, O. Kuschel, J. Wollschläger, M. Tolkiehn, S. Francoual, T. Kuschel
"Impact of magnetic moment and anisotropy of $Co_{1-x}Fe_x$ thin films on the magnetic proximity effect of Pt"
submitted to *Physical Review Letters* (2018); arXiv:1807.09032v2

Non reviewed publications

1. J. Wollschläger, T. Schemme, O. Kuschel, M. Witziok, T. Kuschel, K. Kuepper "Structural, magnetic and magneto optical properties of Fe_3O_4/NiO bilayers on MgO(001)" *Proc. SPIE 9749*, Oxide-based Materials and Devices VII, **974917** (2016); doi:10.1117/12.2219627

Literature

[1] National Research Council. *Physics in a new era: An overview - 9. The economy and the information age*. The National Academies Press, Washington, DC, 2001. doi:10.17226/10118.

[2] S. Waner and S. R. Costenoble. *Finite mathematics*. Cengage Learning, Boston, 7th edition, 2018.

[3] S. A. Wolf, D. D. Awschalom, R. A. Buhrman, J. M. Daughton, S. von Molnár, M. L. Roukes, A. Y. Chtchelkanova and D. M. Treger. "Spintronics: A spin-based electronics vision for the future". *Science*, 294, 1488, 2001. doi:10.1126/science.1065389.

[4] G. Binasch, P. Grünberg, F. Saurenbach and W. Zinn. "Enhanced magnetoresistance in layered magnetic structures with antiferromagnetic interlayer exchange". *Phys. Rev. B*, 39, 4828, 1989. doi:10.1103/PhysRevB.39.4828.

[5] M. N. Baibich, J. M. Broto, A. Fert, F. N. V. Dau, F. Petroff, P. Etienne, G. Creuzet, A. Friederich and J. Chazelas. "Giant magnetoresistance of (001)Fe/(001)Cr magnetic superlattices". *Phys. Rev. Lett.*, 61, 2472, 1988. doi:10.1103/PhysRevLett.61.2472.

[6] M. Julliere. "Tunneling between ferromagnetic films". *Phys. Lett. A*, 54, 225, 1975. doi:10.1016/0375-9601(75)90174-7.

[7] T. Miyazaki and N. Tezuka. "Giant magnetic tunneling effect in Fe/Al_2O_3/Fe junction". *J. Magn. Magn. Mater.*, 139, L231, 1995. doi:10.1016/0304-8853(95)90001-2.

[8] J. S. Moodera, L. R. Kinder, T. M. Wong and R. Meservey. "Large magnetoresistance at room temperature in ferromagnetic thin film tunnel junctions". *Phys. Rev. Lett.*, 74, 3273, 1995. doi:10.1103/PhysRevLett.74.3273.

[9] I. Žutić, J. Fabian and S. D. Sarma. "Spintronics: Fundamentals and applications". *Rev. Mod. Phys.*, 76, 323, 2004. doi:10.1103/RevModPhys.76.323.

[10] A. Fert, A.Barthélémy and F. Petroff. *Nanomagnetism: Ultrathin films, multilayers and nanostructures*. Contemporary Concepts of Condensed Matter Science. Elsevier, Amsterdam, 2nd edition, 2006. doi:10.1016/S1572-0934(05)01006-1.

[11] Z. Zhang and S. Satpathy. "Electron states, magnetism, and the Verwey transition in magnetite". *Phys. Rev. B*, 44, 13319, 1991. doi:10.1103/PhysRevB.44.13319.

[12] C. Klewe, M. Meinert, A. Boehnke, K. Kuepper, E. Arenholz, A. Gupta, J.-M. Schmalhorst, T. Kuschel and G. Reiss. "Physical characteristics and cation distribution of $NiFe_2O_4$ thin films with high resistivity prepared by reactive co-sputtering". *J. Appl. Phys.*, 115, 123903, 2014. doi:10.1063/1.4869400.

[13] M. Meinert and G. Reiss. "Electronic structure and optical band gap determination of $NiFe_2O_4$". *J. Phys. Condens. Matter*, 26, 115503, 2014. doi:10.1088/0953-8984/26/11/115503.

[14] N.-T. H. Kim-Ngan, A. G. Balogh, J. D. Meyer, J. Brötz, M. Zając, T. Ślęzak and J. Korecki. "Thermal and irradiation induced interdiffusion in magnetite thin films grown on magnesium oxide (001) substrates". *Surf. Sci.*, 603, 1175, 2009. doi:10.1016/j.susc.2009.02.028.

[15] K. A. Shaw, E. Lochner and D. M. Lind. "Interdiffusion study of magnesium in magnetite thin films grown on magnesium oxide (001) substrates". *J. Appl. Phys.*, 87, 1727, 2000. doi:10.1063/1.372084.

[16] N.-T. H. Kim-Ngan, A. G. Balogh, J. D. Meyer, J. Brötz, S. Hummelt, M. Zając, T. Ślęzak and J. Korecki. "Structure, composition and crystallinity of epitaxial magnetite thin films". *Surf. Sci.*, 602, 2358, 2008. doi:10.1016/j.susc.2008.04.036.

[17] T. Schemme, A. Krampf, F. Bertram, T. Kuschel, K. Kuepper and J. Wollschläger. "Modifying magnetic properties of ultra-thin magnetite films by growth on Fe precovered MgO(001)". *J. Appl. Phys.*, 118, 113904, 2015. doi:10.1063/1.4930998.

[18] C. Gatel, E. Snoeck, V. Serin and A. R. Fert. "Epitaxial growth and magnetic exchange anisotropy in Fe_3O_4/NiO bilayers grown on MgO(001) and Al_2O_3(0001)". *Eur. J. Phys. B*, 45, 157, 2005. doi:10.1140/epjb/e2005-00073-y.

[19] W. H. Meiklejohn and C. P. Bean. "New magnetic anisotropy". *Phys. Rev.*, 102, 1413, 1956. doi:10.1103/PhysRev.102.1413.

[20] J. Keller, P. Miltényi, B. Beschoten, G. Güntherodt, U. Nowak and K. D. Usadel. "Domain state model for exchange bias. II Experiments". *Phys. Rev. B*, 66, 014431, 2002. doi:10.1103/PhysRevB.66.014431.

[21] W. Lin, K. Chen, S. Zhang and C. L. Chien. "Enhancement of thermally injected spin current through an antiferromagnetic insulator". *Phys. Rev. Lett.*, 116, 186601, 2016. doi:10.1103/PhysRevLett.116.186601.

[22] A. Prakash, J. Brangham, F. Yang and J. P. Heremans. "Spin Seebeck effect through antiferromagnetic NiO". *Phys. Rev. B*, 94, 014427, 2016. doi:10.1103/PhysRevB.94.014427.

[23] S. Hashimoto, J.-L. Peng, W. M. Gibson, L. J. Schowalter and R. W. Fathauer. "Strain measurement of epitaxial CaF_2 on SI (111) by MeV ion channeling". *Appl. Phys. Lett.*, 47, 1071, 1985. doi:10.1063/1.96383.

[24] J. Holanda, D. S. Maior, O. A. Santos, L. H. Vilela-Leão, J. B. S. Mendes, A. Azevedo, R. L. Rodríguez-Suárez and S. M. Rezende. "Spin-current to charge-current conversion and magnetoresistance in a hybrid structure of graphene and yttrium iron garnet". *Appl. Phys. Lett.*, 111, 172405, 2017. doi:10.1103/PhysRevLett.115.226601.

[25] O. Kuschel, R. Buß, W. Spiess, T. Schemme, J. Wöllermann, K. Balinski, A. T. N'Diaye, T. Kuschel, J. Wollschläger and K. Kuepper. "From Fe_3O_4/NiO bilayers to $NiFe_2O_4$-like thin films through Ni interdiffusion". *Phys. Rev. B*, 94, 094423, 2016. doi:10.1103/PhysRevB.94.094423.

[26] O. Kuschel, W. Spiess, T. Schemme, J. Rubio-Zuazo, K. Kuepper and J. Wollschläger. "Real-time monitoring of the structure of ultrathin Fe_3O_4 films during growth on Nb-doped $SrTiO_3$(001)". *Appl. Phys. Lett.*, 111, 041902, 2017. doi:10.1063/1.4995408.

[27] O. Kuschel, N. Pathé, T. Schemme, K. Ruwisch, J. Rodewald, R. Buß, F. Bertram, T. Kuschel, K. Kuepper and J. Wollschläger. "Impact of strain and morphology on magnetic properties of Fe_3O_4/NiO bilayers grown on Nb:$SrTiO_3$(001) and MgO(001)". *Materials*, 11, 1122, 2018. doi:10.3390/ma11071122.

[28] F. Bertram. *The structure of ultrathin iron oxide films studied by x-ray diffraction.* Ph.D. thesis, Osnabrück University, 2012.

[29] R. Gross and A. Marx. *Festkörperphysik.* De Gruyter Oldenbourg, Munich, 2014.

[30] K. Oura, V. G. Lifshits, A. Saranin, A. V. Zotov and M. Katayama. *Surface science - an introduction.* Springer-Verlag, Berlin, Heidelberg, 2003. doi:10.1007/978-3-662-05179-5.

[31] J. W. Matthews and A. E. Blakeslee. "Defects in epitaxial multilayers: I. Misfit dislocations". *J. Cryst. Growth*, 27, 118, 1974. doi:10.1016/S0022-0248(74)80055-2.

[32] E. C. Stoner and E. P. Wohlfarth. "A mechanism of magnetic hysteresis in heterogeneous alloys". *Philos. Trans. Roy. Soc. London*, 240(826), 599, 1948. doi:https://doi.org/10.1098/rsta.1948.0007.

[33] B. D. Culity and C. D. Graham. *Introduction to magnetic materials.* John Wiley & Sons, Hoboken, 2nd edition, 2009.

[34] C. Kittel. "Physical theory of ferromagnetic domains". *Rev. Mod. Phys.*, 21(4), 541, 1949. doi:10.1103/RevModPhys.21.541.

[35] U. Gradmann and J. Müller. "Flat ferromagnetic, epitaxial 48Ni/62Fe(111) films of few atomic layers". *Phys. Stat. Sol.*, 27, 313, 1968. doi:10.1002/pssb.19680270133.

[36] O. Durand, J. R. Childress, P. Galtier, R. Bisaro and A. Schuhl. "Origin of the uniaxial magnetic anisotropy in Fe films grown by molecular beam epitaxy". *J. Magn. Magn. Mater.*, 145, 111, 1995. doi:10.1016/0304-8853(94)01308-X.

[37] Y. Park, E. E. Fullerton, and S. D. Bader. "Growth-induced uniaxial in-plane magnetic anisotropy for ultrathin Fe deposited on MgO(001) by oblique-incidence molecular beam epitaxy". *Appl. Phys. Lett.*, 66, 2140, 1995. doi:10.1063/1.113929.

[38] Y. Z. Wu, C. Won and Z. Q. Qiu. "Magnetic uniaxial anisotropy of Fe films grown on vicinal Ag(001)". *Phys. Rev. B*, 65, 184419, 2002. doi:10.1103/PhysRevB.65.184419.

[39] T. Kuschel, T. Becker, D. Bruns, M. Suendorf, F. Bertram, P. Fumagalli and J. Wollschläger. "Uniaxial magnetic anisotropy for thin Co films on glass studied by magnetooptic Kerr effect". *J. Appl. Phys.*, 109, 093907, 2011. doi:10.1063/1.3576135.

[40] C. Kittel. *Einführung in die Festkörperphysik.* Oldenbourg Wissenschaftsverlag, Munich, 14th edition, 2006.

[41] R. W. DeBlois and C. P. Bean. "Nucleation of ferromagnetic domains in iron whiskers". *J. Appl. Phys.*, 30, S225, 1959. doi:10.1063/1.2185899.

[42] W. H. Bragg and W. L. Bragg. "The reflection of x-rays by crystals". *Proc. Royal Soc. Lond. A*, 88, 428, 1913. doi:10.1098/rspa.1913.0040.

[43] W. Friedrich, P. Knipping and M. Laue. "Interferenzerscheinungen bei Röntgenstrahlen". *Annalen der Physik*, 346, 971, 1913. doi:10.1002/andp.19133461004.

[44] R. Feidenhans'l. "Surface structure determination by x-ray diffraction". *Surface Science Reports*, 10, 105, 1989. doi:10.1016/0167-5729(89)90002-2.

[45] I. K. Robinson and D. J. Tweet. "Surface x-ray diffraction". *Rep. Prog. Phys.*, 55, 599, 1992. doi:10.1088/0034-4885/55/5/002.

[46] *International tables for x-ray crystallography.* Kynoch Press for the International Union of Crystallography, Birmingham, 1952 - 1974.

[47] B. E. Warren. *X-ray diffraction.* Addison-Wesley Pub. Co, Boston, 1969.

[48] E. R. Wölfel. *Die Beugung von Röntgenstrahlen an Kristallgittern (wellenkinematische Theorie). In: Theorie und Praxis der Röntgenstrukturanalyse.* Vieweg+Teubner Verlag, Wiesbaden, 1987. doi:10.1007/978-3-663-07787-9_3.

[49] P. Scherrer. "Bestimmung der Größe und der inneren Srtruktur von Kolloidteilchen mittels Röntgenstrahlen". *Nachrichten von der Gesellschaft der Wissenschaften zu Göttingen, Mathematisch-Physikalische Klasse*, 1918, 98, 1918. doi:10.1007/978-3-662-33915-2_7.

[50] F. Bertram, C. Deiter, T. Schemme, S. Jentsch and J. Wollschläger. "Reordering between tetrahedral and octahedral sites in ultrathin magnetite films grown on MgO(001)". *J. Appl. Phys.*, 113, 184103, 2013. doi:10.1063/1.4803894.

[51] L. G. Parratt. "Surface studies of solids by total reflection of x-rays". *Phys. Rev.*, 95, 359, 1954. doi:10.1103/PhysRev.95.359.

[52] F. Bertram. *Röntgenreflektometrie an ultradünnen Schichten.* Bachelor's thesis, Osnabrück University, 2007.

[53] M. Tolan. *X-ray scattering from soft-matter thin films. Materials science and basic research.* Springer-Verlag, Berlin, Heidelberg, 1999. doi:10.1007/BFb0112834.

[54] L. Névot and P. Croce. "Caractérisation des surfaces par réflexion rasante de rayons x. Application á l'étude du polissage de quelques verres silicates". *Rev. Phys. Appl.*, 15, 761, 1980. doi:10.1051/rphysap:01980001503076100.

[55] M. Henzler. "Measurement of surface defects by low-energy electorn diffraction". *Appl. Phys. A*, 34, 205, 1984. doi:10.1007/BF00616574.

[56] S. Hüfner. *Photoelectron spectroscopy.* Springer-Verlag, Berlin, Heidelberg, 1996. doi:10.1007/978-3-662-03209-1.

[57] D. Briggs and M. P. Seah (Editors). *Practical surface anlysis.* John Wiley & Sons, Hoboken, 1990.

[58] P. J. Cumpson and M. P. Seah. "Elastic scattering corrections in AES and XPS. II. Estimating attenuation lengths and conditions required for their valid use in overlayer/substrate experiments". *Surf. Interface Anal.*, 25, 430, 1997. doi:10.1002/(SICI)1096-9918(199706)25:6<430::AID-SIA254>3.0.CO;2-7.

[59] U. Gelius. "Binding energies and chemical shifts in ESCA". *Phys. Scr.*, 9, 133, 1974. doi:10.1088/0031-8949/9/3/001.

[60] V. I. Nefedov. *X-ray photoelectron spectroscopy of solid surfaces.* CRC Press, Boca Raton, 1988.

[61] A. E. Bocquet, T. Mizokawa, T. Saitoh, H. Namatame and A. Fujimori. "Electronic structure of 3d-transition-metal compounds by analysis of the 2p core-level photoemission spectra". *Phys. Rev. B*, 46(7), 3771, 1992. doi:10.1103/PhysRevB.46.3771.

[62] D. A. Shirley. "High-resolution x-ray photoemission spectrum of the valence bands of gold". *Phys. Rev. B*, 5(12), 4709, 1972. doi:10.1103/PhysRevB.5.4709.

[63] S. Tanuma, C. J. Powell and D. R. Penn. "Calculation of electron inelastic mean free paths (IMFPs) VII. Reliability of the TPP-2M IMFP predictive equation". *Surf. Interface Anal.*, 35(3), 268, 2003. doi:10.1002/sia.1526.

[64] J. W. Cooper. "Photoelectron-angular-distribution parameters for rare-gas subshells". *Phys. Rev. A*, 47, 1841, 1993. doi:10.1103/PhysRevA.47.1841.

[65] J. H. Scofield. "Hartree-Slater subshell photoionization cross-sections at 1254 and 1487 eV". *Journal of Electron Spectroscopy and Related Phenomena*, 8, 129, 1976. doi:10.1016/0368-2048(76)80015-1.

[66] M. B. Trzhaskovskaya, V. I. Nefedov and V. G. Yarzhemsky. "Photoelectron angular distribution parameters for elements $Z = 1$ to $Z = 54$ in the photoelectron energy range 100-5000 eV". *At. Data Nucl. Data Tables*, 77, 97, 2001. doi:10.1006/adnd.2000.0849.

[67] M. B. Trzhaskovskaya, V. K. Nikulin, V. I. Nefedov and V. G. Yarzhemsky. "Non-dipole second order parameters of the photoelectron angular distribution for elements $Z = 1$–100

in the photoelectron energy range 1–10 keV". *At. Data Nucl. Data Tables*, 92, 245, 2006. doi:10.1016/j.adt.2005.12.002.

[68] I. Nedkov and M. Ausloos (Editors). *Nano-crystalline and thin film magnetic oxides*. Kluwer Academic Publishers (The Netherlands), 1998.

[69] M. Cardona. "Optical properties and band structure of $SrTiO_3$ and $BaTiO_3$". *Phys. Rev.*, 140, A651, 1965. doi:10.1103/PhysRev.140.A651.

[70] T. Tomio, H. Miki, H. Tabata, T. Kawai and S. Kawai. "Control of electrical conductivity in laser deposited $SrTiO_3$ thin films with Nb doping". *J. Appl. Phys.*, 75, 5886, 1994. doi:10.1063/1.358404.

[71] M. Bass (Editor). *Handbook of optics*. McGraw-Hill, New York, 2nd edition, 1995.

[72] D. M. Roessler and W. C. Walker. "Electronic spectrum and ultraviolet optical properties of crystalline MgO". *Phys. Rev.*, 159, 733, 1967. doi:10.1103/PhysRev.159.733.

[73] M. A. James and T. Hibma. "Thickness-dependent relaxation of NiO(001) overlayers on MgO(001) studied by x-ray diffraction". *Surf. Sci.*, 433-435, 718, 1999. doi:10.1016/S0039-6028(99)00476-8.

[74] G. A. Sawatzky and J. W. Allen. "Magnitude and origin of the band gap in NiO". *Phys. Rev. Lett.*, 53, 2339, 1984. doi:10.1103/PhysRevLett.53.2339.

[75] G. Srinivasan and M. S. Seehra. "Magnetic susceptibilities, their temperature variation, and exchange constants of NiO". *Phys. Rev. B*, 29, 6295, 1984. doi:10.1103/PhysRevB.29.6295.

[76] R. M. Cornell and U. Schwertmann. *The iron oxides: Structure, properties, reactions, occurences and uses*. Wiley-VCH GmbH & Co. KGaA, Weinheim, 2004. doi:10.1002/3527602097.

[77] J. F. Anderson, M. Kuhn, U. Diebold, K. Shaw, P. Stoyanov and D. Lind. "Surface structure and morphology of Mg-segregated epitaxial Fe_3O_4(001) thin films on MgO(001)". *Phys. Rev. B*, 56, 9902, 1997. doi:10.1103/PhysRevB.56.9902.

[78] M. Hoppe, S. Döring, M. Gorgoi, S. Cramm and M. Müller. "Enhanced ferrimagnetism in auxetic $NiFe_2O_4$ in the crossover to the ultrathin-film limit". *Phys. Rev. B*, 91, 054418, 2015. doi:10.1103/PhysRevB.91.054418.

[79] P. Weiss and R. Forrer. "The absolute saturation of ferromagnetic and laws of approach according to the field and the temperature". *Annales de Physique*, 10(12), 279, 1929. doi:10.1051/anphys/192910120279.

[80] E. J. W. Verwey. "Electronic conduction of magnetite (Fe_3O_4) and its transition point at low temperatures". *Nature*, 144, 327, 1939. doi:10.1038/144327b0.

[81] J. Yoshida and S. Iida. "X-ray diffraction study on the low temperature phase of magnetite". *J. Phys. Soc. Jpn.*, 42, 230, 1977. doi:10.1143/JPSJ.42.230.

[82] X. H. Liu, A. D. Rata, C. F. Chang, A. C. Komarek and L. H. Tjeng. "Verwey transition in Fe_3O_4 thin films: Influence of oxygen stoichiometry and substrate-induced microstructure". *Phys. Rev. B*, 90, 125142, 2014. doi:10.1103/PhysRevB.90.125142.

[83] X. H. Liu, W. Liu and Z. D. Zhang. "Evolution of magnetic properties in the vicinity of the Verwey transition in Fe_3O_4 thin films". *Phys. Rev. B*, 96, 094405, 2017. doi:10.1103/PhysRevB.96.094405.

[84] Z. Li, E. S. Fisher, J. Z. Liu and M. V. Nevitt. "Single-crystal elastic constants of Co-Al and Co-Fe spinels". *J. Mater. Sci.*, 26, 2621, 1991. doi:10.1007/BF00545546.

[85] S. Celotto, W. Eerenstein and T. Hibma. "Characterization of anti-phase boundaries in epitaxial magnetite films". *Eur. Phys. J. B*, 36, 271, 2003. doi:10.1140/epjb/e2003-00344-7.

[86] T. Hibma, F. C. Voogt, L. Niesen, P. A. A. van der Heijden, W. J. M. de Jonge, J. J. T. M. Donkers and P. J. van der Zaag. "Anti-phase domains and magnetism in epitaxial magnetite layers". *J. Appl. Phys.*, 85, 5291, 1999. doi:10.1063/1.369857.

[87] W. Eerenstein, T. T. M. Palstra, T. Hibma and S. Celotto. "Diffusive motion of antiphase domain boundaries in Fe_3O_4 films". *Phys. Rev. B*, 68, 014428, 2003. doi:10.1103/PhysRevB.68.014428.

[88] W. Eerenstein, T. T. M. Palstra, T. Hibma and S. Celotto. "Origin of the increased resistivity in epitaxial Fe_3O_4 films". *Phys. Rev. B*, 66, 201101, 2002. doi:10.1103/PhysRevB.66.201101.

[89] A. V. Singh, B. Khodadadi, J. B. Mohammadi, S. Keshavarz, T. Mewes, D. S. Negi, R. Datta, Z. Galazka, R. Uecker and A. Gupta. "Bulk single crystal-like structural and magnetic characteristics of epitaxial spinel ferrite thin films with elimination of antiphase boundaries". *Adv. Mater.*, 29, 1701222, 2017. doi:10.1002/adma.201701222.

[90] S. Venzke, R. B. van Dover, J. M. Phillips, E. M. Gyorgy, T. Siegrist, C.-H. Chen, D. Werder, R. M. Fleming, R. J. Felder, E. Coleman and R. Opila. "Epitaxial growth and magnetic behavior of $NiFe_2O_4$ thin films". *J. Mater. Res.*, 11, 1187, 1996. doi:10.1557/JMR.1996.0153.

[91] J.-B. Moussy, S. Gota, A. Bataille, M.-J. Guittet, M. Gautier-Soyer, F. Delille, B. Dieny, F. Ott, T. D. Doan, P. Warin, P. Bayle-Guillemaud, C. Gatel and E. Snoeck. "Thickness dependence of anomalous magnetic behavior in epitaxial $Fe_3O_4(111)$ thin films: Effect of density of antiphase boundaries". *Phys. Rev. B*, 70, 174448, 2004. doi:10.1103/PhysRevB.70.174448.

[92] T. Schemme. *Structure and magnetocrystalline anisotropy of interlayer modified ultrathin epitaxial magnetite films on MgO(001).* Ph.D. thesis, Osnabrück University, 2016.

[93] C. Otte. *Rastertunnelmikroskopie an epitaktischen Eisenschichten auf MgO(001).* Diploma thesis, Osnabrück University, 2010.

[94] K. Wille. *Physik der Teilchenbeschleuniger und Synchrotronstrahlungsquellen.* Vieweg+Teubner Verlag, Wiesbaden, 1992. doi:10.1007/978-3-663-11850-3.

[95] J. Als-Nielsen and D. McMorrow. *Elements of modern x-ray physics.* John Wiley & Sons, Hoboken, 2001. doi:10.1002/9781119998365.

[96] J. Falta and T. Möller. *Forschung mit Synchrotronstrahlung. Eine Einführung in die Grundlagen und Anwendungen.* Vieweg+Teubner Verlag, Wiesbaden, 2010.

[97] J. Rodewald. Ph.D. thesis, Osnabrück University, 2020.

[98] C. J. Powell and A. Jablonski. "Surface sensitivity of x-ray photoelectron spectroscopy". *Nucl. Instrum. Methods Phys. Res., Sect. A*, 601, 54, 2009. doi:10.1016/j.nima.2008.12.103.

[99] C. M. Schlepütz, S. O. Mariager, S. A. Pauli, R. Feidenhans'l and P. R. Willmott. "Angle calculations for a (2+3)-type diffractometer: focus on area detectors". *J. Appl. Cryst.*, 44, 73, 2011. doi:10.1107/S0021889810048922.

[100] H. You. ""Angle calculations for a '4S+2D' six-circle diffractometer". *J. Appl. Cryst.*, 32, 614, 1999. doi:10.1107/S0021889899001223.

[101] E. Vlieg. "Integrated intensities using a six-circle surface x-ray diffractometer". *J. Appl. Cryst.*, 30, 532, 1997. doi:10.1107/S0021889897002537.

[102] A. Greuling. *Röntgenstrukturanalyse von Isolatorschichten.* Masters's thesis, Osnabrück University, 2007.

[103] S. Hahne. *Strukturanalyse von Praseodymoxidschichten mit Röntgenbeugung.* Bachelor's thesis, Osnabrück University, 2008.

[104] F. Bertram. *Röntgenstrukturanalyse von Oxidschichten*. Masters's thesis, Osnabrück University, 2009.

[105] A. Hoffmann and S. D. Bader. "Opportunities at the frontiers of spintronics". *Phys. Rev. Applied*, 4, 047001, 2015. doi:10.1103/PhysRevApplied.4.047001.

[106] G. E. W. Bauer, E. Saitoh and B. J. van Wees. "Spin caloritronics". *Nat. Mater.*, 11, 391, 2012. doi:10.1038/NMAT3301.

[107] G. Schmidt. "Concepts for spin injection into semiconductors - a review". *J. Phys. D: Appl. Phys.*, 38, R107, 2005. doi:10.1088/0022-3727/38/7/R01.

[108] J.-B. Moussy. "From epitaxial growth of ferrite thin films to spin-polarized tunnelling". *J. Phys. D: Appl. Phys.*, 46, 143001, 2013. doi:10.1088/0022-3727/46/14/143001.

[109] P. Seneor, A. Fert, J.-L. Maurice, F. Montaigne, F. Petroff and A. Vaurés. "Large magnetoresistance in tunnel junctions with an iron oxide electrode". *Appl. Phys. Lett.*, 74, 4017, 1999. doi:10.1063/1.123246.

[110] T. Kado. "Large room-temperature inverse magnetoresistance in tunnel junctions with a Fe_3O_4 electrode". *Appl. Phys. Lett.*, 92, 092502, 2008. doi:10.1063/1.2890852.

[111] E. Wada, K. Watanabe, Y. Shirahata, M. Itoh, M. Yamaguchi and T. Taniyama. "Efficient spin injection into GaAs quantum well across Fe_3O_4 spin filter". *Appl. Phys. Lett.*, 96, 102510, 2010. doi:10.1063/1.3357436.

[112] R. Ramos, A. Anadón, I. Lucas, K. Uchida, P. A. Algarabel, L. Morellón, M. H. Aguirre, E. Saitoh and M. R. Ibarra. "Thermoelectric performance of spin Seebeck effect in Fe_3O_4/ Pt-based thin film heterostructures". *APL Materials*, 4, 104802, 2016. doi:10.1063/1.4950994.

[113] R. Ramos, T. Kikkawa, K. Uchida, H. Adachi, I. Lucas, M. H. Aguirre, P. Algarabel, L. Morellón, S. Maekawa, E. Saitoh and M. R. Ibarra. "Observation of the spin Seebeck effect in epitaxial Fe_3O_4 thin films". *Appl. Phys. Lett.*, 102, 072413, 2013. doi:10.1063/1.4793486.

[114] K.-I. Uchida, H. Adachi, T. Kikkawa, A. Kirihara, M. Ishida, S. Yorozu, S. Maekawa and E. Saitoh. "Thermoelectric generation based on spin Seebeck effects". *Proc. IEEE*, 104, 1946, 2016. doi:10.1109/JPROC.2016.2535167.

[115] K. Kato and S. Iida. "Observation of ferroelectric hysteresis loop of Fe_3O_4 at 4.2 K". *J. Phys. Soc. Jpn.*, 51, 1335, 1982. doi:10.1143/JPSJ.51.1335.

[116] M. Alexe, M. Ziese, D. Hesse, P. Esquinazi, K. Yamauchi, T. Fukushima, S. Picozzi and U. Gösele. "Ferroelectric switching in multiferroic magnetite (Fe_3O_4) thin films". *Adv. Mater.*, 21, 4452, 2009. doi:10.1002/adma.200901381.

[117] G. R. Castro. "Optical design of the general-purpose Spanish x-ray beamline for absorption and diffraction". *J. Synchrotron Radiat.*, 5, 657, 1998. doi:10.1107/S0909049597019079.

[118] J. Rubio-Zuazo, M. Escher, M. Merkel and G. R. Castro. "High voltage-cylinder sector analyzer 300/15: A cylindrical sector analyzer for electron kinetic energies up to 15 keV". *Rev. Sci. Instrum.*, 81, 043304, 2010. doi:10.1063/1.3398441.

[119] J. Rubio-Zuazo and G. R. Castro. "Beyond hard x-ray photoelectron spectroscopy: Simultaneous combination with x-ray diffraction". *J. Vac. Sci. Technol. A*, 31, 031103, 2013. doi:10.1116/1.4801915.

[120] J. Rubio-Zuazo and G. R. Castro. "Hard x-ray photoelectron spectroscopy (HAXPES) (15 keV) at SpLine, the Spanish CRG beamline at the ESRF". *Nucl. Instr. Meth. Phys. Res. A*, 547, 64, 2005. doi:10.1016/j.nima.2005.05.013.

[121] T. Schemme, O. Kuschel, F. Bertram, K. Kuepper and J. Wollschläger. "Structure and morphology of epitaxially grown Fe_3O_4/NiO bilayers on MgO(001)". *Thin Solid Films*, 589, 526, 2015. doi:10.1016/j.tsf.2015.06.018.

[122] T. Yamashita and P. Hayes. "Analysis of XPS spectra of Fe^{2+} and Fe^{3+} ions in oxide materials". *Appl. Surf. Sci.*, 254, 2441, 2008. doi:10.1016/j.apsusc.2007.09.063.

[123] T. Fujii, F. M. F. de Groot, G. A. Sawatzky, F. C. Voogt, T. Hibma and K. Okada. "In situ XPS analysis of various iron oxide films grown by NO_2-assisted molecular-beam epitaxy". *Phys. Rev. B*, 59, 3195, 1999. doi:10.1103/PhysRevB.59.3195.

[124] R. Pentcheva, W. Moritz, J. Rundgren, S. Frank, D. Schrupp and M. Scheffler. "A combined DFT/LEED-approach for complex oxide surface structure determination: Fe_3O_4(001)". *Surf. Sci.*, 602, 1299, 2008. doi:10.1016/j.susc.2008.01.006.

[125] J. Korecki, B. Handke, N. Spiridis, T. Slezak, F. Flis-Kabulska and J. Haber. "Size effects in epitaxial films of magnetite". *Thin Solid Films*, 412, 14, 2002. doi:10.1016/S0040-6090(02)00306-1.

[126] D. Levy, G. Artioli and M. Dapiaggi. "The effect of oxidation and reduction on thermal expansion of magnetite from 298 to 1173 K at different vacuum conditions". *J. Solid State Chem.*, 177, 1713, 2004. doi:10.1016/j.jssc.2003.12.032.

[127] C. N. R. Rao. "Transition metal oxides". *Annu. Rev. Phys. Chem.*, 40, 291, 1989. doi:10.1146/annurev.pc.40.100189.001451.

[128] L. Marnitz, K. Rott, S. Niehörster, C. Klewe, D. Meier, S. Fabretti, M. Witziok, A. Krampf, O. Kuschel, T. Schemme, K. Kuepper, J. Wollschläger, A. Thomas, G. Reiss and T. Kuschel. "Sign change in the tunnel magnetoresistance of Fe_3O_4/MgO/Co-Fe-B magnetic tunnel junctions depending on the annealing temperature and the interface treatment". *AIP Advances*, 5, 047103, 2015. doi:10.1063/1.4917018.

[129] G. R. Hoogeboom, A. Aqeel, T. Kuschel, T. T. M. Palstra and B. J. van Wees. "Negative spin Hall magnetoresistance of Pt on the bulk easy-plane antiferromagnet NiO". *Appl. Phys. Lett.*, 111, 052409, 2017. doi:10.1063/1.4997588.

[130] D. Hou, Z. Qui, J. Barker, K. Sato, K. Yamamoto, S. Vélez, J. M. Gomez-Perez, L. E. Hueso, F. Casanova and E. Saitoh. "Tunable sign change of spin Hall magnetoresistance in Pt/NiO/YIG structures". *Phys. Rev. Lett.*, 118, 147202, 2017. doi:10.1103/PhysRevLett.118.147202.

[131] S. K. Arora, H.-C. Wu, R. J. Choudhary, I. V. Shvets, O. N. Mryasov, H. Yao and W. Y. Ching. "Giant magnetic moment in epitaxial Fe_3O_4 thin films on MgO(100)". *Phys. Rev. B*, 77, 134443, 2008. doi:10.1103/PhysRevB.77.134443.

[132] S. K. Arora, R. G. S. Sofin, I. V. Shvets and M. Luysberg. "Anomalous strain relaxation behavior of Fe_3O_4/MgO(100) heteroepitaxial system grown using molecular beam epitaxy". *J. Appl. Phys.*, 100, 073908, 2006. doi:10.1063/1.2349468.

[133] H.-C. Wu, R. Ramos, R. G. S. Sofin, Z.-M. Liao, M. Abid and I. V. Shvets. "Transversal magneto-resistance in epitaxial Fe_3O_4 and Fe_3O_4/NiO exchange biased system". *Appl. Phys. Lett.*, 101, 052402, 2012. doi:10.1063/1.4739951.

[134] H.-C. Wu, S. K. Arora, O. N. Mryasov and I. V. Shvets. "Antiferromagnetic interlayer exchange coupling between Fe_3O_4 layers across a nonmagnetic MgO dielectric layer". *Appl. Phys. Lett.*, 92, 182502, 2008. doi:10.1063/1.2919081.

[135] Y. Z. Chen, J. R. Sun, Y. N. Han, X. Y. Xie, J. Shen, C. B. Rong, S. L. He and B. G. Shen. "Microstructure and magnetic properties of strained Fe_3O_4 films". *J. Appl. Phys.*, 103, 07D703, 2008. doi:10.1063/1.2832305.

[136] M. Monti, M. Sanz, M. Oujja, E. Rebollar, M. Castillejo, F. J. Pedrosa, A. Bollero, J. Camarero, J. L. F. Cunado, N. M. Nemes, F. J. Mompean, M. Garcia-Hernández, S. Nie, K. F. McCarty, A. T. N'Diaye, G. Chen, A. K. Schmid, J. F. Marco and J. de la Figuera. "Room temperature in-plane ⟨100⟩ magnetic easy axis for $Fe_3O_4/SrTiO_3$(001):Nb grown by infrared pulsed laser deposition". *J. Appl. Phys.*, 114, 223902, 2013. doi:10.1063/1.4837656.

[137] G. Chern and C. Cheng. "Interface matching in oxides of rocksalt/rocksalt(001) and rocksalt/perovskite(001)". *J. Vac. Sci. Technol.*, A17, 1097, 1999. doi:10.1116/1.581780.

[138] R. J. Kennedy. "The growth of iron oxide, nickel oxide and cobalt oxide thin films by laser ablation from metal targets". *IEEE Trans. Magn.*, 31, 3829, 1995. doi:10.1109/20.489786.

[139] K. H. L. Zhang, R. Wu, F. Tang, W. Li, R. E. Oropeza, L. Qiao, V. K. Lazarov, Y. Du, D. J. Payne, J. L. MacManus-Driscoll and M. G. Blamire. "Electronic structure and band alignment at the NiO and $SrTiO_3$ p-n heterojunctions". *Appl. Mater. Interfaces*, 9, 26549, 2017. doi:10.1021/acsami.7b06025.

[140] M. Pilard, O. Ersen, S. Cherifi, B. Carvello, L. Roiban, B. Muller, F. Scheurer, L. Ranno and C. Boeglin. "Magnetic properties of coupled ultrathin NiO/Fe_3O_4 (001) films". *Phys. Rev. B*, 76, 214436, 2007. doi:10.1103/PhysRevB.76.214436.

[141] K. Kuepper, O. Kuschel, N. Pathé, T. Schemme, J. Schmalhorst, A. Thomas, E. Arenholz, M. Gorgoi, R. Ovsyannikov, S. Bartkowski, G. Reiss and J. Wollschlager. "Electronic and magnetic structure of epitaxial Fe_3O_4(001)/NiO heterostructures grown on MgO(001) and Nb-doped $SrTiO_3$(001)". *Phys. Rev. B*, 94, 024401, 2016. doi:10.1103/PhysRevB.94.024401.

[142] I. P. Krug, F. U. Hillebrecht, M. W. Haverkort, A. Tanaka, L. H. Tjeng, H. Gomonay, A. Fraile-Rodriguez, F. Nolting, S. Cramm and C. M. Schneider. "Impact of interface orientation on magnetic coupling in highly ordered systems: A case study of the low-indexed Fe_3O_4/NiO interfaces". *Phys. Rev. B*, 78, 064427, 2008. doi:10.1103/PhysRevB.78.064427.

[143] H.-Q. Wang, W. Gao, E. I. Altman and V. E. Heinrich. "Studies of the electronic structure at the Fe_3O_4-NiO interface". *J. Vac. Sci. Technol. A*, 22, 1675, 2004. doi:10.1116/1.1763900.

[144] R. Bliem, E. McDermott, P. Ferstl, M. Setvin, O. Gamba, J. Pavelec, M. A. Schneider, M. Schmid, U. Diebold, P. Blaha, L. Hammer and G. S. Parkinson. "Subsurface cation vacancy stabilization of the magnetite (001) surface". *Science*, 346, 1215, 2014. doi:10.1126/science.1260556.

[145] H. W. Nesbitt, D. Legrand and G. M. Bancroft. "Interpretation of Ni 2p XPS spectra of Ni conductors and Ni insulators". *Phys. Chem. Miner.*, 27, 357, 2000. doi:10.1007/s002690050265.

[146] A. P. Grosvenor, M. C. Biesinger, R. S. C. Smart and N. S. McIntyre. "New interpretations of XPS spectra of nickel metal and oxides". *Surf. Sci.*, 600, 1771, 2006. doi:10.1016/j.susc.2006.01.041.

[147] S. Uhlenbrock, C. Scharfschwerdtt, M. Neumannt, G. Illing and H.-J. Freund. "The influence of defects on the Ni 2p and O 1s XPS of NiO". *J. Phys. Condens. Matter*, 4, 7973, 1992. doi:10.1088/0953-8984/4/40/009.

[148] L. Soriano, I. Preda, A. Gutiérrez, S. Palacín, M. Abbate and A. Vollmer. "Surface effects in the Ni 2p x-ray photoemission spectra of NiO". *Phys. Rev. B*, 75, 233417, 2007. doi:10.1103/PhysRevB.75.233417.

[149] A. N. Mansour. "Characterization of NiO by XPS". *Surf. Sci. Spectra*, 3, 231, 1994. doi:10.1116/1.1247751.

[150] A. F. Carley, S. D. Jackson, J. N. O'Shea and M. W. Roberts. "The formation and characterisation of Ni^{3+} - an x-ray photoelectron spectroscopic investigation of potassium-doped Ni(110)-O". *Surf. Sci. Lett.*, 440, L868, 1999. doi:10.1016/S0039-6028(99)00872-9.

[151] B. L. Henke, E. M. Gullikson and J. C. Davis. "X-ray interactions: photoabsorption, scattering, transmission, and reflection at $E = 50 - 30000\,\mathrm{eV}$, $Z = 1 - 92$". *At. Data. Nucl. Data Tables*, 54, 181, 1993. doi:10.1006/adnd.1993.1013.

[152] A. Pimpinelli and J. Villain. *Physics of crystal growth.* Campbridge University Press, Cambridge, 1998. doi:10.1017/CBO9780511622526.

[153] H.-T. Jeng and G. Y. Guo. "First-principles investigations of the electronic structure and magnetocrystalline anisotropy in strained magnetite Fe_3O_4". *Phys. Rev. B*, 65, 094429, 2002. doi:10.1103/PhysRevB.65.094429.

[154] D. T. Margulies, F. T. Parker, M. L. Rudee, F. E. Spada, J. N. Chapman, P. R. Aitchison and A. E. Berkowitz. "Origin of the anomalous magnetic behavior in single crystal Fe_3O_4 films". *Phys. Rev. Lett.*, 79, 5162, 1997. doi:10.1103/PhysRevLett.79.5162.

[155] K. Fleischer, O. Mauit and I. V. Shvets. "Stability and capping of magnetite ultra-thin films". *Appl. Phys. Lett.*, 104, 192401, 2014. doi:10.1063/1.4876059.

[156] A. G. Every and A. K. McCurdy. *Second and higher order elastic constants.* Springer Materials - The Landolt-Boernstein Database , Springer-Verlag, Berlin, Heidelberg, 1992.

[157] K. Balakrishnan, S. K. Arora and I. V. Shvets. "Strain relaxation studies of the Fe_3O_4/MgO(100) heteroepitaxial system grown by magnetron sputtering". *J. Phys.: Condens. Matter*, 16(30), 5387, 2004. doi:10.1088/0953-8984/16/30/001.

[158] J. Cheng, G. E. Sterbinsky and B. W. Wessels. "Magnetic and magneto-optical properties of heteroepitaxial magnetite thin films". *J. Cryst. Growth*, 310, 3730, 2008. doi:10.1016/j.jcrysgro.2008.05.048.

[159] J. Dho, B. Kim and S. Ki. "Substrate effects on in-plane magnetic anisotropy and Verwey transition temperatures of (100) magnetite (Fe_3O_4) films". *IEEE Trans. Magn.*, 52, 2600304, 2016. doi:10.1109/TMAG.2016.2521604.

[160] G. W. Leung, M. E. Vickers, R. Yu and M. G. Blamire. "Epitaxial growth of $Fe_3O_4(111)$ on $SrTiO_3(001)$ substrates". *J. Cryst. Growth*, 310, 5282, 2008. doi:10.1016/j.jcrysgro.2008.07.126.

[161] D. T. Margulies, F. T. Parker and A. E. Berkowitz. "Magnetic anomalies in single crystal Fe_3O_4 thin films". *J. Appl. Phys.*, 75, 6097, 1994. doi:10.1103/PhysRevLett.79.5162.

[162] T. Schemme, N. Pathé, G. Niu, F. Bertram, T. Kuschel, K. Kuepper and J. Wollschläger. "Magnetic anisotropy related to strain and thickness of ultrathin iron oxide films on MgO(001)". *Mater. Res. Exp.*, 2(1), 016101, 2015. doi:10.1088/2053-1591/2/1/016101.

[163] S. Kale, S. M. Bhagat, S. E. Lofland, T. Scabarozi, S. B. Ogale, A. Orozco, S. R. Shinde, T. Venkatesan, B. Hannover, B. Mercey and W. Prellier. "Film thickness and temperature dependence of the magnetic properties of pulsed-laser-deposited Fe_3O_4 films on different substrates". *Phys. Rev. B*, 64, 205413, 2001. doi:10.1103/PhysRevB.64.205413.

[164] P. Prieto, J. E. Prieto, R. Gargallo-Caballero, J. F. Marco and J. de la Figueraca. "Role of the substrate on the magnetic anisotropy of magnetite thin films grown by ion-assisted deposition". *Appl. Surf. Sci.*, 359, 742, 2015. doi:10.1016/j.apsusc.2015.10.180.

[165] R. Wu and A. J. Freeman. "Spin-orbit induced magnetic phenomena in bulk metals and their surfaces and interfaces". *J. Magn. Magn. Mater*, 200, 498, 1999. doi:10.1016/S0304-8853(99)00351-0.

[166] P. I. Slick. *Ferromagnetic materials: A handbook on the properties of magnetically ordered substances*, volume 2. North-Holland Publishing Company, Amsterdam, 1980.

[167] M. I. Katsnelson, V. Y. Irkhin, L. Chioncel, A. I. Lichtenstein and R. A. de Groot. "Half-metallic ferromagnets: From band structure to many-body effects". *Rev. Mod. Phys.*, 80, 315, 2008. doi:10.1103/RevModPhys.80.315.

[168] J. M. Byrne, N. Klueglein, C. Pearce, K. M. Rosso, E. Appel and A. Kappler. "Redox cycling of Fe(II) and Fe(III) in magnetite by Fe-metabolizing bacteria". *Science*, 347(6229), 1473, 2015. doi:10.1126/science.aaa4834.

[169] G. E. Sterbinsky, J. Cheng, P. T. Chiu, B. W. Wessels and D. J. Keavney. "Investigation of heteroepitaxial growth of magnetite thin films". *J. Vac. Sci. Technol. B*, 25, 1389, 2007. doi:10.1116/1.2757185.

[170] F. Bertram, C. Deiter, O. Hoefert, T. Schemme, F. Timmer, M. Suendorf, B. Zimmermann and J. Wollschläger. "X-ray diffraction study on size effects in epitaxial magnetite thin films on MgO(001)". *J. Phys. D: Appl. Phys.*, 45, 395302, 2012. doi:10.1088/0022-3727/45/39/395302.

[171] J. A. Moyer, S. Lee, P. Schiffer and L. W. Martin. "Magnetically disordered phase in epitaxial iron-deficient F e_3O_4 thin films". *Phys. Rev. B*, 91(6), 064413, 2015. doi:10.1103/PhysRevB.91.064413.

[172] L. A. Kalev, P. Schurer and L. Nielsen. "Emission Mössbauer spectroscopy study of the Fe_3O_4 surface and Fe_3O_4/MgO(100) and Fe_3O_4/CoO(100) interfaces". *Phys. Rev. B*, 68, 165407, 2003. doi:10.1103/PhysRevB.68.165407.

[173] J. Rubio-Zuazo, L. Onandia, E. Salas-Colera, A. Munoz-Noval and G. R. Castro. "Incommensurate growth of thin and ultrathin films of single-phase Fe_3O_4(001) on $SrTiO_3$(001)". *J. Phys. Chem. C*, 119(2), 1108, 2015. doi:10.1021/jp510615j.

[174] D. Meier, T. Kuschel, L. Shen, A. Gupta, T. Kikkawa, K. Uchida, E. Saitoh, J.-M. Schmalhorst and G. Reiss. "Thermally driven spin and charge currents in thin $NiFe_2O_4$/Pt films". *Phys. Rev. B*, 87, 054421, 2013. doi:10.1103/PhysRevB.87.054421.

[175] D. Meier, D. Reinhardt, M. van Straaten, C. Klewe, M. Althammer, M. Schreier, S. T. B. Goennenwein, A. Gupta, M. Schmid, C. H. Back, J.-M. Schmalhorst, T. Kuschel and G. Reiss. "Longitudinal spin Seebeck effect contribution in transverse spin Seebeck effect experiments in Pt/YIG and Pt/NFO". *Nat. Commun.*, 6, 8211, 2015. doi:10.1038/ncomms9211.

[176] M. Althammer, S. Meyer, H. Nakayama, M. Schreier, S. Altmannshofer, M. Weiler, H. Huebl, S. Geprägs, M. Opel, R. Gross, D. Meier, C. Klewe, T. Kuschel, J.-M. Schmalhorst, G. Reiss, L. Shen, A. Gupta, Y.-T. Chen, G. E. W. Bauer, E. Saitoh and S. T. B. Goennenwein. "Quantitative study of the spin Hall magnetoresistance in ferromagnetic insulator/normal metal hybrids". *Phys. Rev. B*, 87(22), 224401, 2013. doi:10.1103/PhysRevB.87.224401.

[177] F. M. F. de Groot. "Multiplet effects in x-ray spectroscopy". *Coord. Chem. Rev.*, 249, 31, 2005. doi:10.1016/j.ccr.2004.03.018.

[178] E. Stavitski and F. M. F. de Groot. "The CTM4XAS program for EELS and XAS spectral shape analysis of transition metal L edges". *Micron*, 41(7), 687, 2010. doi:10.1016/j.micron.2010.06.005.

[179] S. A. Chambers and S. A. Joyce. "Surface termination, composition and reconstruction of Fe_3O_4(001) and γ-Fe_2O_3(001)". *Surf. Sci.*, 420, 111, 1999. doi:10.1016/S0039-6028(98)00657-8.

[180] P. C. J. Graat and M. A. J. Somers. "Simultaneous determination of composition and thickness of thin iron-oxide films from XPS Fe 2p spectra". *Appl. Surf. Sci.*, 100/ 101, 36, 1996. doi:10.1016/0169-4332(96)00252-8.

[181] N. S. McIntyre and M. G. Cook. "X-ray photoelectron studies on some oxides and hydroxides of cobalt, nickel, and copper". *Anal. Chem.*, 47(13), 1975. doi:10.1021/ac60363a034.

[182] M. C. Biesinger, B. P. Payne, A. P. Grosvenor, L. W. M. Lau, A. R. Gerson and R. S. C. Smart. "Resolving surface chemical states in XPS analysis of first row transition metals, oxides and hydroxides: Cr, Mn, Fe, Co and Ni". *Appl. Surf. Sci.*, 257(7), 2717, 2011. doi:10.1016/j.apsusc.2010.10.051.

[183] J. T. Newberg, D. E. Starr, S. Yamamoto, S. Kaya, T. Kendelewicz, E. R. Mysak, S. Porsgaard, M. B. Salmeron, G. E. Brown Jr., A. Nilsson and H. Bluhm. "Formation of hydroxyl and water layers on MgO films studied with ambient pressure XPS". *Surf. Sci.*, 605, 89, 2011. doi:10.1016/j.susc.2010.10.004.

[184] C. J. O'Brien, Z. Rak and D. W. Brenner. "Free energies of (Co, Fe, Ni, Zn)Fe_2O_4 spinels and oxides in water at high temperatures and pressure from density functional theory: results for stoichiometric NiO and $NiFe_2O_4$ surfaces". *J. Phys.: Condens. Matter*, 25, 445008, 2013. doi:10.1088/0953-8984/25/44/445008.

[185] C. T. Chen, Y. U. Idzerda, H.-J. Lin, N. V. Smith, G. Meigs, E. Chaban, G. H. Ho, E. Pellegrin and F. Sette. "Experimental confirmation of the x-ray magnetic circular dichroism sum rules for iron and cobalt". *Phys. Rev. Lett.*, 75, 152, 1995. doi:10.1103/PhysRevLett.75.152.

[186] Y. Teramura, A. Tanaka and T. Jo. "Effect of Coulomb interaction on the x-ray magnetic circular dichroism spin sum rule in 3 d transition elements". *J. Phys. Soc. Jap.*, 65, 1053, 1996. doi:10.1143/JPSJ.65.1053.

[187] C. Piamonteze, P. Miedema and F. M. F. de Groot. "Accuracy of the spin sum rule in XMCD for the transition-metal L edges from manganese to copper". *Phys. Rev. B*, 80(18), 184410, 2009. doi:10.1103/PhysRevB.80.184410.

[188] R. A. D. Pattrick, G. Van der Laan, C. M. B. Henderson, P. Kuiper, E. Dudzik and D. J. Vaughan. "Cation site occupancy in spinel ferrites studied by x-ray magnetic circular dichroism: developing a method for mineralogists". *Eur. J. Mineral.*, 14, 1095, 2002. doi:10.1127/0935-1221/2002/0014-1095.

[189] G. F. M. Gomes, T. E. P. Bueno, D. E. Parreiras, G. J. P. Abreu, A. de Siervo, J. C. Cezar, H.-D. Pfannes and R. Paniago. "Magnetic moment of Fe_3O_4 films with thicknesses near the unit-cell size". *Phys. Rev. B*, 90, 134422, 2014. doi:10.1103/PhysRevB.90.134422.

[190] G. H. Jaffari, A. K. Rumaiz, J. C. Woicik and S. I. Shah. "Influence of oxygen vacancies on the electronic structure and magnetic properties of $NiFe_2O_4$ thin films". *J. Appl. Phys.*, 111, 093906, 2012. doi:10.1063/1.4704690.

[191] C. Jin, Q. Zhang, W. B. Mi, E. Y. Jiang and H. L. Bai. "Tunable magnetic and electrical properties of polycrystalline and epitaxial $Ni_xFe_{3-x}O_4$ thin films prepared by reactive co-sputtering". *J. Phys. D: Appl. Phys.*, 43, L5001, 2010. doi:10.1088/0022-3727/43/38/385001.

[192] A. Shan, X. Wu, J. Lu, C. Chen and R. Wang. "Phase formations and magnetic properties of single crystal nickel ferrite ($NiFe_2O_4$) with different morphologies". *CrystEngComm*, 17, 1603, 2015. doi:10.1039/C4CE02139H.

[193] J. Rodewald, J. Thien, T. Pohlmann, M. Hoppe, F. Timmer, F. Bertram, K. Kuepper and J. Wollschläger. "Formation of ultrathin cobalt ferrite films by interdiffusion of Fe_3O_4/CoO bilayers". *Phys. Rev. B*, 100, 155418, 2019. doi:10.1103/PhysRevB.100.155418.

Danksagung

An dieser Stelle sei allen gedankt, die mich bei der Erstellung dieser Doktorarbeit unterstützt haben, auch wenn nicht jeder explizit namentlich erwähnt ist. In erster Linie gilt mein Dank Prof. Dr. Joachim Wollschläger für die ausdauernde Unterstützung bei der Betreuung meiner Doktorarbeit, die zahlreichen Disskussionen, Geduld und Verständnis in vielen Situationen sowie das entgegengebrachte Vertrauen. Außerdem bedanke ich mich bei den Mitgliedern meiner Promotionskommission Juniorprof. Dr. Robin Steinigeweg, Dr. Karsten Küpper und insbesondere bei Prof. Dr. Jan Ingo Flege von der BTU Cottbus-Senftenberg, der die Rolle des Zweitgutachters übernommen hat.

Des Weiteren möchte ich mich bei Wanja Spieß, Ralph Buß und Nico Pathé bedanken, die während ihrer eigenen Masterarbeiten erheblich zum Gelingen meiner Arbeit beigetragen haben. Danke für euer wissenschafliches Engagement und die gute Zusammenarbeit. In diesem Kontext bedanke ich mich auch bei Tobias Schemme, Frederic Timmer, Jannis Thien, Kevin Ruwisch, Jari Rodewald für die tatkräftige Unterstützung während diverser Synchrotron-Messzeiten sowie die Hilfe bei den Reparaturen und Messungen im Labor. Besonderer Dank gilt hierbei auch Florian Bertram für seine Hilfsbereitschaft während der Messzeiten am DESY sowie bei der Auswertung der Beugungsdaten. Bei den Mitarbeitern der Feinmechanischen Werkstatt und der Werkstatt für Elektronik bedanke ich mich für den schnellen Einsatz bei Reparaturen und Konstruktionen.

Ein großes Dankeschön geht an meine aktuellen und ehemaligen Bürokollegen Henrik Wilkens, Wanja Spieß, Jari Rodewald und Gregor Steinhoff, die mir immer mit Rat und Tat in den unterschiedlichsten Lebens- und Laborsituationen zur Seite standen. Auch den namentlich hier nicht aufgeführten Mitgliedern der Arbeitsgruppe 'Dünne Schichten und Grenzflächen' danke ich für die tolle Arbeitsatmosphäre und die stete Hilfsbereitschaft.

Ein besonderer Dank gilt meiner Familie, ohne die das Ganze nicht möglich gewesen wäre. Hier ist insbesondere mein Bruder Konstantin erwähnt, ohne dessen Anstoß ich sicher nicht Physik studiert hätte. Vor allem aber danke ich von ganzem Herzen meinem Ehemann und Freund Timo für seine grenzenlose Unterstützung und Verständnis, aber auch die tatkräftige Hilfe in allen Lebensbereichen als auch bei dieser Arbeit. Danke für die zahlreichen Diskussionen und Ideen, die gemeinsamen Messzeiten, das aufmerksame Korrekturlesen und für vieles mehr...